

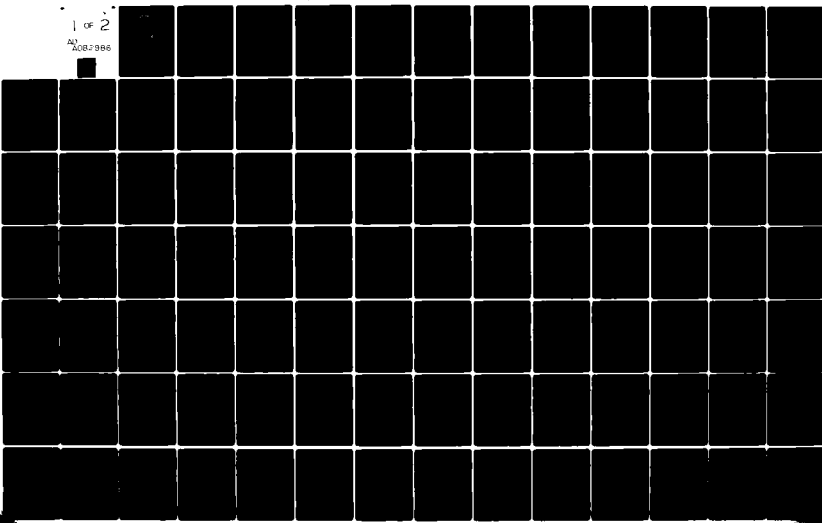
AD-A082 986

PENNSYLVANIA STATE UNIV. UNIVERSITY PARK APPLIED RESE--ETC F/6 7/4  
SCATTERING OF LOW ENERGY HELIUM BEAMS FROM CLEAN SURFACES OF SO--ETC(U)  
DEC 79 6 N DERRY  
N00024-79-C-6043

UNCLASSIFIED ARL/PSU/TM-79-220 NL

1 of 2

AD-A082 986



ADA 082986

LEVEL

12

SCATTERING OF LOW ENERGY HELIUM BEAMS FROM  
CLEAN SURFACES OF SODIUM FLUORIDE, LITHIUM  
FLUORIDE, AND GRAPHITE

Gregory Neil Derry



Technical Memorandum  
File No. TM 79-220  
December 13, 1979  
Contract No. N00024-79-C-6043

Copy No. 11

The Pennsylvania State University  
Institute for Science and Engineering  
APPLIED RESEARCH LABORATORY  
Post Office Box 30  
State College, PA 16801

APPROVED FOR PUBLIC RELEASE  
DISTRIBUTION UNLIMITED

NAVY DEPARTMENT

NAVAL SEA SYSTEMS COMMAND

80 4 10 043

DDC FILE COPY

## UNCLASSIFIED

SECURITY CLASSIFICATION OF THIS PAGE (When Data Entered)

REPORT DOCUMENTATION PAGE		READ INSTRUCTIONS BEFORE COMPLETING FORM
1. REPORT NUMBER TM 79-220	2. GOVT ACCESSION NO.	3. RECIPIENT'S CATALOG NUMBER
4. TITLE (and Subtitle) <del>SCATTERING OF LOW ENERGY HELIUM BEAMS FROM CLEAN SURFACES OF SODIUM FLUORIDE, LITHIUM FLUORIDE, AND GRAPHITE,</del>		5. TYPE OF REPORT & PERIOD COVERED PhD Thesis, May 1980
6. AUTHOR(s) 10) Gregory Neil Derry		6. PERFORMING ORG. REPORT NUMBER TM 79-220
7. PERFORMING ORGANIZATION NAME AND ADDRESS The Pennsylvania State University Applied Research Laboratory P. O. Box 30, State College, PA 16801		8. CONTRACT OR GRANT NUMBER(s) N00024-79-C-6043
9. CONTROLLING OFFICE NAME AND ADDRESS Naval Sea Systems Command Department of the Navy Washington, DC 20362		10. PROGRAM ELEMENT, PROJECT, TASK AREA & WORK UNIT NUMBERS 11) 13 Dec 79
11. MONITORING AGENCY NAME & ADDRESS(if different from Controlling Office)		12. REPORT DATE December 13, 1979
		13. NUMBER OF PAGES 115 pages & figures
		14. SECURITY CLASS. (of this report) Unclassified, Unlimited
		15a. DECLASSIFICATION/DOWNGRADING SCHEDULE
16. DISTRIBUTION STATEMENT (of this Report) Approved for public release, distribution unlimited, per NSSC (Naval Sea Systems Command), 2/1/80		
17. DISTRIBUTION STATEMENT (of the abstract entered in Block 20, if different from Report) 9) Technical memo		
18. SUPPLEMENTARY NOTES		
19. KEY WORDS (Continue on reverse side if necessary and identify by block number) helium, beam, scattering, graphite, thesis 7) (4) (3) (4)		
20. ABSTRACT (Continue on reverse side if necessary and identify by block number) An examination of helium beam scattering from the basal plane of graphite and from [001] surfaces of two alkali halide crystals is presented. Results are given for both ${}^4\text{He}$ and ${}^3\text{He}$ . Incident beam energies used range from 2.9 meV to 17.3 meV, chosen to probe the physisorption regime. Bound state energy levels are measured for ${}^4\text{He}$ and ${}^3\text{He}$ adsorbed on graphite, NaF and LiF. Matrix elements of the atom-surface potential Fourier components are measured for ${}^4\text{He}$ on graphite and LiF. A brief discussion of how this information is used to determine the details of the gas-atom - solid surface		

UNCLASSIFIED

SECURITY CLASSIFICATION OF THIS PAGE(When Data Entered)

20. ABSTRACT (continued)

interaction is given. In the case of <sup>4</sup>He and <sup>3</sup>He on graphite, comparison is made with thermodynamic adsorption data for submonolayer films and excellent agreement is found. (4)

Resonance lineshapes are studied for <sup>4</sup>He scattering from LiF and from graphite as the incident angles and energy are varied. The LiF results are seen to agree well with recent theoretical predictions. For graphite, some phenomena exhibit conformance to elastic theory while others appear to contradict it. Experimental evidence that the latter are due to inelastic scattering mechanisms is presented.

Accession For	
NTIS	ORNL
DDC TAB	<input type="checkbox"/>
Unannounced	<input type="checkbox"/>
Justification _____	
By _____	
Distribution _____	
Available _____	
Available or Special	
Dist	A

UNCLASSIFIED

SECURITY CLASSIFICATION OF THIS PAGE(When Data Entered)

## ABSTRACT

An examination of helium beam scattering from the basal plane of graphite and from [001] surfaces of two alkali halide crystals is presented. Results are given for both  $^4\text{He}$  and  $^3\text{He}$ . Incident beam energies used range from 2.9 meV to 17.3 meV, chosen to probe the physisorption regime.

Bound state energy levels are measured for  $^4\text{He}$  and  $^3\text{He}$  adsorbed on graphite, NaF and LiF. Matrix elements of the atom - surface potential Fourier components are measured for  $^4\text{He}$  on graphite and LiF. A brief discussion of how this information is used to determine the details of the gas-atom - solid surface interaction is given. In the case of  $^4\text{He}$  and  $^3\text{He}$  on graphite, comparison is made with thermodynamic adsorption data for submonolayer films and excellent agreement is found.

Resonance lineshapes are studied for  $^4\text{He}$  scattering from LiF and from graphite as the incident angles and energy are varied. The LiF results are seen to agree well with recent theoretical predictions. For graphite, some phenomena exhibit conformance to elastic theory while others appear to contradict it. Experimental evidence that the latter are due to inelastic scattering mechanisms is presented.

## TABLE OF CONTENTS

	Page
<b>ABSTRACT</b> . . . . .	iii
<b>LIST OF TABLES</b> . . . . .	vi
<b>LIST OF FIGURES</b> . . . . .	vii
<b>ACKNOWLEDGMENTS</b> . . . . .	x
<b>I. INTRODUCTION</b> . . . . .	1
<b>II. HISTORICAL REVIEW</b> . . . . .	3
A. Early Work . . . . .	3
B. Recent Work . . . . .	3
<b>III. THEORY</b> . . . . .	6
A. Introduction . . . . .	6
B. Kinematics of the Scattering Process . . . . .	7
C. Band Structure of Adsorbed Atoms . . . . .	9
D. Dynamical Scattering Theories . . . . .	11
<b>IV. APPARATUS</b> . . . . .	14
A. Beam Formation . . . . .	14
B. Scattering Chamber . . . . .	18
C. Alignment . . . . .	24
D. $^3\text{He}$ Recirculation System . . . . .	26
E. Low Energy Beam Production . . . . .	28
F. Electron Optics . . . . .	31
<b>V. EXPERIMENTAL RESULTS</b> . . . . .	33
A. Alkali Halides . . . . .	33
1. Binding energies . . . . .	35
2. Matrix elements . . . . .	43
3. Comparison with scattering theories . . . . .	46
B. Graphite . . . . .	50
1. Sample preparation . . . . .	52
2. Binding energies . . . . .	58
3. Second-order resonances and splittings . . . . .	63
a. Using 17.3 meV incident beam . . . . .	63
b. Using 4.7 meV incident beam . . . . .	69
4. Inelastic effects . . . . .	75
<b>VI. DISCUSSION</b> . . . . .	81
A. Alkali Halides . . . . .	81
1. Laterally averaged potentials . . . . .	81
2. Surface periodicity . . . . .	84
B. Graphite . . . . .	87
1. Application to physisorption . . . . .	87
2. Evaluation of scattering theory . . . . .	92

## TABLE OF CONTENTS (cont.)

	Page
C. Conclusions . . . . .	94
D. Suggestions for Future Work . . . . .	96
REFERENCES . . . . .	97
APPENDIX . . . . .	101
Misalignment and Angular Measurement . . . . .	101
A1. Introduction . . . . .	101
A2. Angle Measurements for Graphite . . . . .	101
A3. Effects of Misalignment . . . . .	102
A3a. Surface Normal Misalignments . . . . .	102
A3b. Rotation Axes Misalignments . . . . .	102
A3c. Beam and Surface Misalignments . . . . .	103

## LIST OF TABLES

Table	Page
1. Energy eigenvalues for He/NaF . . . . .	42
2. Energy eigenvalues for He/LiF . . . . .	42
3. $^4\text{He}/\text{LiF}$ matrix elements in meV . . . . .	48
4. Energy eigenvalues for $^4\text{He}/\text{graphite}$ . . . . .	61
5. Energy eigenvalues for $^3\text{He}/\text{graphite}$ . . . . .	63
6A. Parameters of the 3-9 potential . . . . .	82
6B. Parameters of the shifted Morse hybrid potential . . . . .	82
7. Comparison of experimental and calculated eigenvalues . . .	83
8. Experimental and theoretical values of $^4\text{He}/\text{LiF}$ matrix elements (in meV) . . . . .	86
9. Parameters of modified Yukawa-6 potential, from Reference 69 . . . . .	89
10. Experimental and theoretical energy eigenvalues of He/graphite (in meV) . . . . .	89
11. Theoretical and experimental matrix elements for He/graphite (in meV) . . . . .	90
12. Zeroing results before and after detector axis change . .	104

## LIST OF FIGURES

Figure	Page
1. Schematic of beam formation . . . . .	15
2. Diagram of the apparatus . . . . .	17
3. Top view of scattering chamber . . . . .	20
4. Sample holder geometry, showing incident beam direction (1), polar angle rotation (2), and azimuthal angle rotation (3). . . . .	21
5. Cross-sectional view of sample holder used in graphite work . . . . .	23
6. Schematic of $^3\text{He}$ recirculation and storage system . . . .	27
7. Schematic of apparatus for cooling the nozzle to very low temperatures . . . . .	30
8. The LiF surface lattice (with basis vectors) and 3D crystal directions; $\phi = 0^\circ$ is defined to be along the (10) direction . . . . .	34
9. Typical specular intensity data for He on alkali halides, showing selective adsorption minima . . . . .	36
10. Selective adsorption loci in the $K_x$ - $K_y$ plane for $^4\text{He}/\text{LiF}$ ; points are measured values, lines are circles described by Equation (6) using average energies . . . . .	37
11. Selective adsorption loci for $^3\text{He}/\text{LiF}$ ; points and lines have same meaning as in Figure 10 . . . . .	38
12. Selective adsorption loci for $^4\text{He}/\text{NaF}$ ; points and lines have same meaning as in Figure 10 . . . . .	39
13. Selective adsorption loci for $^3\text{He}/\text{NaF}$ ; points and lines have same meaning as in Figure 10 . . . . .	40
14. Scans of specular intensity vs. polar angle for a variety of azimuthal values showing the band splitting of two selective adsorption features (maxima in this case) . . . .	44
15. Data of Figure 14 plotted in $K_x$ - $K_y$ plane, showing the splitting; lines are calculated free particle circles [Equation (6)] . . . . .	45

## LIST OF FIGURES (cont.)

Figure	Page
16. Scan of specular intensity vs. azimuthal angle at $\theta = 70^\circ$ (nominal), showing resonance lineshape for different transitions . . . . .	47
17. Specular intensity ratio for two temperatures, plotted vs. $\cos^2 \theta$ to test Equation (10) . . . . .	49
18. The graphite basal plane structure, showing the unit cell and the first-order reciprocal lattice vectors . . . . .	51
19. Profile of a specularly reflected beam, taken by scanning the detector with the sample fixed . . . . .	56
20. Plot of $\theta_d$ vs. $\theta'$ , used to determine the polar angle zero .	57
21. Typical specular intensity data for He/graphite, showing selective adsorption minima . . . . .	59
22. Selective adsorption loci in the $K_x$ - $K_y$ plane for $^4\text{He}/\text{graphite}$ ; points are measured values, lines are circles described by Equation (6) using average energies . . . . .	60
23. Selective adsorption loci for $^3\text{He}/\text{graphite}$ ; points and lines have same meaning as in Figure 22 . . . . .	62
24a. Specular intensity vs. azimuthal angle at 17.3 meV for several values of polar angle corresponding to region "a" of Figure 25 . . . . .	64
24b. Same as Figure 24a except corresponding to region "b" of Figure 25 . . . . .	65
24c. Same as Figure 24a except corresponding to region "c" of Figure 25 . . . . .	66
25. Resonance loci of data in Figure 24 plotted in normalized $K_x$ - $K_y$ plane; points are measured data, lines are free particle curves [Equation (6)] . . . . .	67
26. Specular intensity vs. azimuthal angle as in Figure 24 except incident energy is 4.7 meV . . . . .	70
27. Resonance loci of data in Figure 26, plotted as in Figure 25 . . . . .	71
28. Resonance loci as in Figure 27 but over a larger area of the $K_x$ - $K_y$ plane . . . . .	73

## LIST OF FIGURES (cont.)

Figure	Page
29. Specular intensity vs. polar angle for several azimuthal angles, showing the splitting depicted in Figure 28; arrows indicate positions of $l(1,0)$ resonance for which $\theta$ scans were not taken . . . . .	74
30a. Specular intensity vs. polar angle for $\theta = 0^\circ$ at 16.8 meV incident beam energy; the (*) indicate features predicted to be maxima (see text) . . . . .	77
30b. Same as Figure 30a except for a 5.1 meV beam energy . . . . .	78
31. The measurement of total diffracted intensity; specular and diffraction intensities are plotted vs. polar angle . . . . .	80
32. Plot of the 3-9 potential (---) and the shifted Morse hybrid potential (---) for He/NaF (from Ref. 64) . . . . .	85
33. Plot of modified Yukakwa-6 potential (summed) for He/graphite over principle lattice sites (from Ref. 69) . . . . .	91

## ACKNOWLEDGMENTS

The author would first like to thank Dr. Daniel R. Frankl for his high standards and constant interest in this work. Dr. W. E. Carlos, Dr. M. W. Cole, and Mr. C. Schwartz are thanked for many stimulating discussions. Dr. S. V. Krishnaswamy, Mr. T. O'Gorman, Dr. T. Thwaites, Mr. M. P. Liva, Dr. G. Vidali, Ms. H. Zimmermann, and, most of all, Mr. David A. Wesner are all thanked for their valuable contributions to the experimental work. Drs. T. Noggle, G. Wagoner, M. Dowell, M. Bienfait, and G. P. Felcher are all acknowledged for providing graphite samples. Drs. G. Boato, J. H. Weare, E. D. Thompson, and V. Celli are thanked for providing results of their work in advance of publication. The aid of Dr. W. A. Steele is acknowledged; in particular, an extended loan of the  $^3\text{He}$  storage system. Mr. H. Henry, Mr. R. Sauers, and Mr. J. Weeks are thanked for their technical assistance. The National Science Foundation and the Applied Research Laboratory of The Pennsylvania State University, under contract with the Naval Sea Systems Command, are thanked for their financial support of this project.

## I. INTRODUCTION

In the last few years, atomic beam scattering has undergone a period of rapid development. Beams of low energy neutral atoms are used to study the properties of surfaces and the details of the atom-surface interaction. Although it is possible to study a variety of phenomena such as gas-surface reactions and surface phonon modes, the discussion here will be mainly restricted to elastic scattering of rare gas atoms. The relative simplicity of this case makes it particularly useful for the development of experimental and theoretical techniques. Moreover, much intrinsically interesting physics is involved in the understanding of such systems.

The information generated by the atomic beam scattering experiment is unique in several ways. The low energy and relatively large mass of the incident atoms assure virtually no penetration into the bulk, making the experiment almost totally surface sensitive. The low energy of the atoms (~10 meV or less in some cases) makes them an excellent probe of the physisorption regime. Also, since the incident flux is quite low, it is possible to gain direct information about the interaction of a single atom in the presence of a solid surface, as opposed to measurements of thermodynamic variables of physisorbed films in which atom-atom interactions must be taken into account.

There are also, however, several important limitations in the experiment. The nonzero velocity spread of the incident beam and nonperfect condition of the sample surface tend to limit the

resolution. There are no limitations in principle on the type of sample surface used, but in practice, only a few surfaces have been used with much success. Metals, for example, have produced diffraction in only a few rare cases. Finally, full analysis of the scattering data with physically realistic theories is extremely difficult, especially in the case of inelastic scattering. Much has been done recently to alleviate these problems, but they all remain, at least to some extent.

As mentioned above, the discussion here will be mainly restricted to elastically scattered rare gas atoms. Some of that work has been done at relatively high energies ( $\sim 100$  meV), which primarily yield an estimate of the corrugation for the periodic part of the atom-surface potential by using semi-classical scattering theory. This study, however, will be concerned mostly with the low energy regime ( $\sim 10$  meV) where quantum effects predominate. Under these conditions, many problems of the analysis can be avoided by considering only the kinematics of the scattering event. This method yields direct information on both the form of the attractive well and the strongly repulsive periodic part of the atom-surface potential.

The major emphasis of the present work is on the interaction of helium atoms with the basal plane of graphite. An important motivation for the study of this system is the existence of much data on the thermodynamics of submonolayer He films adsorbed on graphite. These have been widely used to explore the physics of two-dimensional arrays, and it is hoped that the present work will contribute to the understanding of this body of work.

## II. HISTORICAL REVIEW

### A. Early Work

The earliest work on atomic beam scattering from solid surfaces is that of Stern, et al.<sup>1</sup> in 1930. They observed diffraction of He and H<sub>2</sub> atoms from alkali halide surfaces, thus confirming the de Broglie wave hypothesis. They also saw anomalous minima in the specular beam intensity. Lennard-Jones and Devonshire<sup>2</sup> hypothesized that these minima were evidence of the atoms entering into bound states of an attractive well between the atom and surface. They termed this phenomenon "selective adsorption".

The beam used in this work was an "oven beam" with a Maxwell-Boltzman distribution of velocities. This gave poor resolution. The vacuum attainable at that time was also poor. Rapid advances in vacuum technology led to a renewal of interest in beam scattering from solids in the mid 1960's. Owing to the continued use of thermal beams, however, the resolution obtained by Crews,<sup>3</sup> Fisher and Bledsoe,<sup>4</sup> and O'Keefe et al.<sup>5</sup> was little better than Stern's. These workers all used alkali halide targets; O'Keefe et al. tried different isotopic forms (<sup>3</sup>He, D<sub>2</sub>) and heavy rare gases for incident beams.

### B. Recent Work

The next major advance was the use of "supersonic nozzles" to obtain very narrow velocity distributions.<sup>6</sup> Using nozzle beams and ultra-high vacuum techniques, accurate studies of <sup>4</sup>He diffraction from alkali halides were done by Williams et al.<sup>7</sup> and Boato et al.<sup>8</sup> H and

D were scattered from alkali halides in ultra-high vacuum by Wilsch et al.,<sup>9</sup> but oven beams had to be used to keep the atomic species dissociated. These workers all cleaned the surface by heating in vacuum. Houston, Meyers, and Frankl<sup>10</sup> obtained a clean surface by cleaving the alkali halide crystals in situ and studying <sup>4</sup>He scattering from them. Williams et al. and Boato et al. concentrated mostly on diffraction work, while Wilsch et al. and Meyers et al. emphasized study of the bound-state resonances (selective adsorption).

With the advent of these higher quality data, new theoretical efforts were undertaken. The early work of Cabrera et al.<sup>11</sup> and of Wolken<sup>12</sup> did not properly include the resonance states and predicted maxima in the specular beam instead of the experimentally observed minima. The calculations of Chow and Thompson<sup>13</sup> resolved this problem, predicting specular minima within an elastic scattering framework. Another problem with older theories was the use of unrealistic model potentials, e.g., the Morse potential, which was shown to be inconsistent with the more accurate data.<sup>10</sup> Pairwise sums and semi-empirical potentials have since been employed,<sup>14</sup> along with simplified models (e.g., a hard wall with corrugation and square well) in some of the scattering calculations.

The most recent theoretical work has attempted to account for the fine structure seen in atom-surface scattering. Examples of this are the work of Weare et al.<sup>15</sup> and Garcia et al.<sup>16</sup> Theoretical accounts of the interactions of bound state resonances<sup>17,18</sup> have also been attempted. The latter phenomenon has been the subject of recent

experimental investigation also.<sup>19</sup> Another trend in recent experimental work has been toward a wider diversity of surfaces used as targets. Cardillo<sup>20</sup> has seen diffraction of <sup>4</sup>He from the (111) surface of silicon. Work has also been reported on silver,<sup>21</sup> nickel,<sup>22</sup> and nickel oxide,<sup>23</sup> using beams of <sup>4</sup>He and H<sub>2</sub>. The basal plane surface of graphite has been extensively studied by Boato et al.,<sup>24</sup> by Valbusa et al.<sup>25</sup> using H<sub>2</sub>, D<sub>2</sub>, H, and D, and by the author.<sup>26</sup> Boato et al., using beams of <sup>4</sup>He atoms with energies of ~17 meV and ~63 meV, made a thorough study of the interactions between resonances and a preliminary measurement of the resonance binding energies, as well as some diffraction work. The contributions of the author are discussed in the remainder of the present thesis.

### III. THEORY

#### A. Introduction

The development of a complete and satisfactory theory for atomic beam scattering is far from finished. Great strides have been made in recent years, however. More importantly, a large class of experiments can be interpreted extremely well using a set of simplifying assumptions. The latter will first be developed extensively, and then some attention will be devoted to the former.

A complete scattering theory must, of course, take into account the presence of inelastic events in the scattering process. At present, however, such a theory is virtually nonexistent and, moreover, has little relevance to most of the experimental work described herein. Therefore, we will restrict the discussion to elastic scattering. The general goal of these theories is to predict the intensities of the scattered beams. It is possible, however, to obtain much useful information solely from the kinematics of the scattering event without regard for the actual intensities of the outgoing beams; only their geometry with respect to the surface, along with that of the incident beam, need be known.

Only a brief summary of theoretical considerations is given here since the author has not made a significant contribution in this area. The main purpose of this chapter is to clarify the interpretation of the data. In Sections B and C, the kinematical point of view, first developed by Lennard-Jones and Devonshire,<sup>2</sup> is discussed. In Section D, a brief examination of several recent dynamical theories is presented.

### B. Kinematics of the Scattering Process

The incident atom is well modelled as a free particle characterized by a kinetic energy,  $E_b$ . This is essentially a plane wave of wave vector  $|\bar{k}_i| = \frac{2\pi}{\lambda}$ , and the incident wave vector can be decomposed into components parallel and perpendicular to the sample surface:

$$\bar{k}_i = \bar{K} + k_z \hat{z} \quad (1a)$$

and

$$\bar{K} = k_x \hat{x} + k_y \hat{y} \quad . \quad (1b)$$

The z-axis, of course, is the surface normal, while the  $\hat{x}$  can be chosen to be parallel to some crystal symmetry axis in the surface lattice.

The two-dimensional reciprocal lattice of the crystal surface can be obtained via the usual techniques from the corresponding two-dimensional real-space lattice of the surface. Vectors in this space are denoted as

$$\bar{G}_{m,n} = m\bar{g}_1 + n\bar{g}_2 , \quad (2)$$

where  $\bar{g}_1$  and  $\bar{g}_2$  are the fundamental vectors of the surface reciprocal lattice.

In order to satisfy conservation of crystal momentum in the scattering event, the two-dimensional Bragg condition

$$\bar{k}_f = \bar{k}_i + \bar{G}_{m,n} \quad (3)$$

must be satisfied for the final and initial wave vector components parallel to the surface. Conservation of energy can be ensured by

requiring that

$$\frac{\hbar^2}{2m} k_i^2 = E_i = E_f = E(\bar{k}_f) + E_{zf} \quad (4)$$

for the final and incident. Note that these conditions are only valid for the case of elastic scattering.

Combining Equations 3) and (4) and approximating the atom's translational motion as a free particle yields a condition for an elastic scattering event to occur; namely,

$$\bar{k}_i^2 = (\bar{k}_i + \bar{G}_{m,n})^2 + k_{zf}^2 . \quad (5)$$

If  $k_{zf}^2$  is positive, there will be an outgoing scattered beam; this is simply the case of diffraction from a two-dimensional lattice. If  $k_{zf}^2$  is negative, there will be no diffracted beams allowed. There is a physical situation, however, which corresponds to negative  $k_{zf}^2$ .

Van der Waals forces give rise to a weak attractive potential between the gas atom and the surface, leading to a discrete set of bound states with energy  $E_j = \frac{\hbar^2}{2m} \varepsilon_j$ . When  $k_{zf}^2$  is equal to one of the  $\varepsilon_j$ , the incident atom is in resonance with a bound state and undergoes a so-called "selective adsorption" transition.<sup>27</sup> The selectively adsorbed atom is in a one-dimensional bound state with respect to the z-axis and translates across the surface in a Bloch state. Its translational motion can be approximated as a free particle, in which case its translational energy is simply  $\frac{\hbar^2}{2m} K_f^2$ . In this approximation, then, the selective adsorption condition becomes

$$(\bar{k}_i + \bar{G}_{m,n})^2 = \bar{k}_i^2 - \varepsilon_j = \bar{k}_i^2 + |\varepsilon_j| . \quad (6)$$

This is readily seen to be the equation of a circle in  $K_x - K_y$  space centered at  $-\bar{G}_{m,n}$  and having a radius of  $(\bar{k}_i^2 + |\varepsilon_j|)^{1/2}$ .

Notice that the  $E_j$  are the eigenvalues of a one-dimensional Schroedinger equation employing the laterally averaged atom-surface potential Hamiltonian. Thus, much information about the nature of this potential can be extracted from measurements of the  $E_j$ . These in turn can be calculated from Equation (6) if the magnitude of the incident wave vector and its orientation relative to the surface are known when a selective adsorption occurs. The effects of selective adsorption on the scattered intensity will be discussed in Section II.D. The reliability of the approximation leading to Equation (6) will be assessed in the following section.

### C. Band Structure of Adsorbed Atoms

The potential energy of an atom in the presence of a solid surface can be written as a Fourier expansion in the surface reciprocal lattice vectors:

$$V(\bar{r}) = V_0(z) + \sum_{\bar{G} \neq 0}^{\infty} V_{\bar{G}}(z) e^{i\bar{G} \cdot \bar{R}} . \quad (7)$$

The  $V_0(z)$  term is the laterally averaged potential and the summation of higher-order terms constitutes the two-dimensional periodicity of the surface, i.e., the corrugation. The free-atom approximation made in the preceding section consists essentially of retaining only the  $\bar{G} = 0$  term of the expansion. The approximation may be refined by

including the higher-order terms as a perturbation or by including them in dynamical scattering calculation. Using the latter technique, Chow and Thompson<sup>17</sup> predicted the effects of higher-order terms. If circles predicted by Equation (6) for two different states [labelled by  $(m,n)$  and  $j$ ] cross in  $K_x - K_y$  space, there will be a degeneracy of the two states there. The periodic part of the potential acts to lift the degeneracy, giving rise to a band splitting. This is observed in the scattering data as a splitting of the selective adsorption features instead of their merging into a single feature.

The magnitude of the splitting depends, of course, on the Fourier component which admixes the states as well as their energy quantum numbers. Standard second-order perturbation theory<sup>28</sup> yields the result that the magnitude of the splitting is equal to  $2 \langle j | v_{G-G} | j' \rangle$ , the matrix element which connects the two states. In many cases, this matrix element is too small to produce an observable splitting and the levels appear to cross. A more sophisticated band-structure calculation has been done by Carlos<sup>29</sup> for He/graphite, and it was found that the perturbation theory results are generally quite good. Although there are still small deviations in regions far from crossings, the behavior there is quite close to free-atom-like.

The foregoing discussion has several implications for the experiments. In order to accurately measure the binding energies  $E_j$  of the physisorbed atoms, the data must be taken far from any splittings, which render Equation (6) incorrect. If, however, data is taken extensively throughout a splitting, the matrix element for that case

can be calculated. Thus, information can be obtained concerning the periodic part of the potential as well as  $V_0(z)$ , which can be reconstructed from the  $E_j$ .

#### D. Dynamical Scattering Theories

There are many problems inherent in the prediction of actual intensities of scattered beams as a function of incident geometry and energy. Some of these are experimental, such as the imperfection of the surface and distribution of energies in the incident beam. A major theoretical problem is the inability to handle inelastic scattering, which is often quite important. Other problems are the severity of the approximations necessary to make the calculations tractable and nonuniqueness of the models which provide good fits to the data.

Despite these problems, much progress has been made in recent years. The semiclassical approaches will not be dealt with here since they are not very relevant to the energy regime of interest. A good review of these methods is given by Goodman.<sup>30</sup> Two of the more fruitful techniques undertaken recently will be discussed.

The method of Chow and Thompson<sup>13,17</sup> is to expand the atomic wave function in surface reciprocal lattice vectors and insert it into the Schrödinger equation along with Equation (7). This yields a set of coupled differential equations:

$$\left[ \frac{d^2}{dz^2} + k_{zf}^2 \right] \psi_{\bar{G}}(z) - \frac{2m}{\hbar^2} \sum_{\bar{G}'} V_{\bar{G}-\bar{G}'}(z) \psi_{\bar{G}'}(z) = 0 , \quad (8)$$

which are numerically integrated. Of this infinite set of equations, some set  $N$  must be chosen for the computation, corresponding to the  $N$  diffraction channels (i.e.,  $\vec{G}$  vectors) which are important in the scattering process. It was discovered that certain closed channels ( $k_{zf}^2 < 0$ ) must be included as well as open channels. When this was done properly, the theory predicted intensity minima for the selective adsorption features in the specular beam, in agreement with the experimental results. This was found to be the case for several different model potentials.

A Green's function formalism was more recently employed by Weare et al.<sup>15</sup> to predict the lineshapes of the resonance features. They write the scattering equation in integral form:

$$|\psi_K^+\rangle = |\chi_K^+\rangle + G_d^+ V_p |\psi_K^+\rangle , \quad (9)$$

where  $|\chi_K^+\rangle$  is an eigenfunction of the unperturbed Hamiltonian.  $V_p$  is the periodic part of the potential [given by the summation in Equation (7)], and  $G_d^+$  is a representation of Green's operator. This method leads to singularities at the resonance energies. These are eliminated by means of projection operators. Approximate expansions and numerical techniques are then used to solve the scattering problem in detail.

The major qualitative results of this method are readily summarized. Concerning the lineshape of the selective adsorption feature, a minimum in specular intensity is expected if the resonant state is strongly coupled to both the incident beam and an open diffraction channel. Otherwise, a maximum in intensity is expected to be the

dominant feature. Another interesting prediction concerns resonances which are not observable due to weak coupling or high energy quantum number. Such a state could become observable by "borrowing" intensity from a more prominent resonance to which it is strongly coupled by a low-order Fourier component. This would happen near crossings, as discussed in Section III.C.

A set of rules to predict the lineshape of the specular intensity at resonance has also been derived by Garcia et al.<sup>16</sup> using a corrugated hard-wall with an attractive well as a model potential. These calculations employ an exact scattering formalism and yield results similar to those of Weare et al.,<sup>15</sup> although the rules are stated in different terms. This method can also be used to treat the mixing of resonances. The predictions of these theories are compared with experiments in Chapters V and VI after the experimental results have been presented.

#### IV. APPARATUS

The major components of the atomic beam apparatus were constructed by D. E. Houston<sup>31</sup> and J. E. Meyers.<sup>32</sup> A description of the essential parts of the apparatus is given in Sections A and B. The author also made several contributions to and modifications of the equipment. In Section A, the investigation of beam instability and the brief mention of low-temperature nozzle cooling belong in this category. In Section B, the modifications to the sample holder are the major example.

The work described in Sections C, D, E, and F was done in whole or in part by the author. In Section C, the problems of apparatus alignment are considered. Section D describes the auxiliary system devised in order to perform <sup>3</sup>He scattering experiments. The equipment and techniques needed for cryogenic cooling of the nozzle are discussed in Section E, while Section F presents a brief account of the electron optics and its uses.

##### A. Beam Formation

The first step in the formation of the atomic beam is expansion of the source gas through a nozzle into vacuum. The nozzles used in this work are electron microscope apertures (platinum or molybdenum), typically about 10 microns in diameter. The second part of the beam source is an electroformed copper cone ("skimmer") with an orifice of about 0.2 mm diameter facing the nozzle as shown in Figure 1. The skimmer can be moved laterally for alignment purposes.

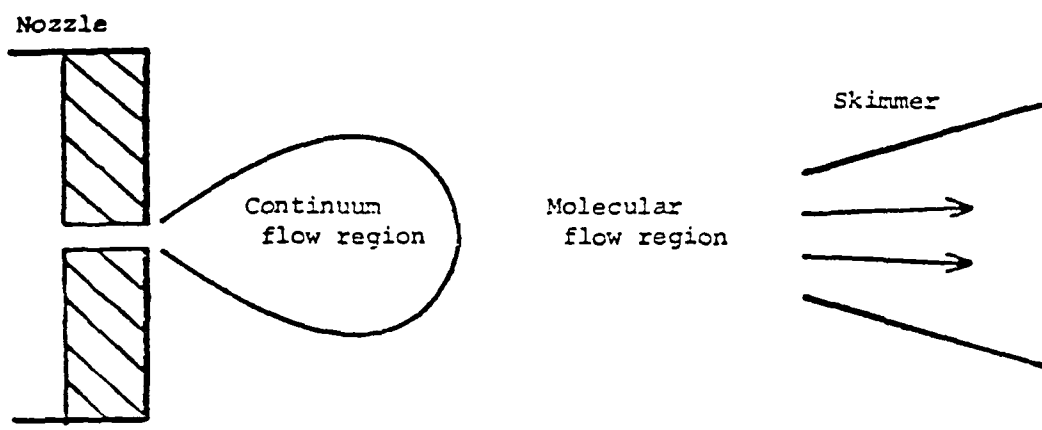


Figure 1. Schematic of beam formation.

The details of supersonic beam formation have been discussed at length elsewhere,<sup>6,27</sup> and only the more important properties of nozzle beams will be summarized here. The motion of the gas atoms becomes more directed along the axis of the nozzle aperture with the skimmer eliminating most of the remaining gas. The gas temperature decreases greatly during the expansion, but the average kinetic energy of the atoms comprising the beam is determined by the temperature of the gas behind the nozzle. The distribution of velocities is much narrower than a Maxwellian distribution characterized by the temperature of the gas behind the nozzle. The details of the velocity distribution depend on the source pressure, nozzle diameter, and nozzle temperature.<sup>33</sup>

In general, the distribution narrows with increasing pressure and diameter. With the nozzle cooled by liquid nitrogen, typical source pressures (~6 atm) yield velocity distributions of  $\frac{\Delta v}{v} < 2\%$  FWHM. At a nozzle temperature of 20K, typical source pressures are lower (~1  $\frac{1}{2}$  atm) and the distribution is a little broader ( $\frac{\Delta v}{v} \sim 2 \frac{1}{2}\%$  FWHM). The upper limit of the source pressure is essentially determined by the pumping speed in the first stage, because if the pressure there becomes too high, the beam intensity attenuates rapidly.

The skimmer separates the first stage from the second stage (see Figure 2). The second stage houses the mechanical chopper. The beam is chopped at 240 Hz, while a light and photo cell provide a reference signal to a lock-in amplifier. This allows extraction of the beam signal from the background noise, which may be several orders of magnitude larger.

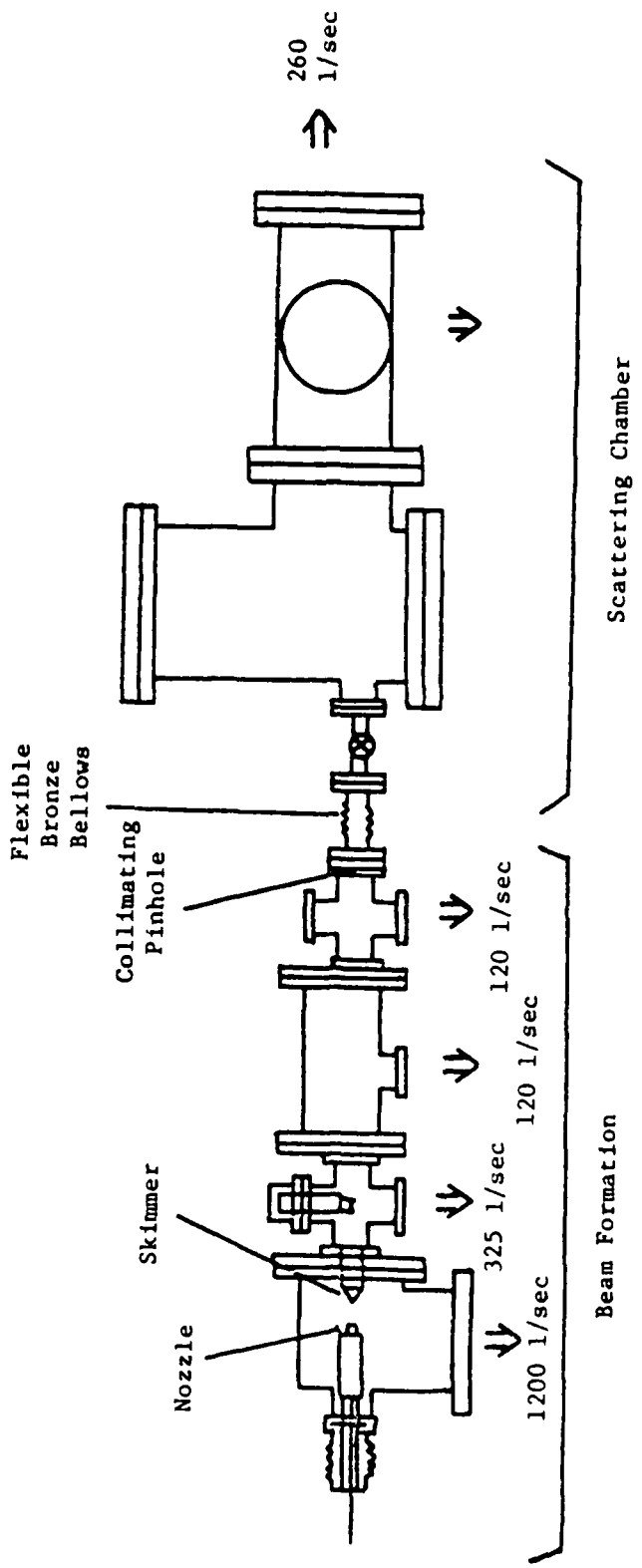


Figure 2. Diagram of the apparatus

The third stage is a velocity selector consisting of five rotating slotted disks.<sup>32,34</sup> This is needed only for measuring the velocity since the velocity distribution is very narrow. During the scattering experiments, the selector is lifted out of the beam. When measuring the velocity, the selector is run in both directions and an average taken to compensate for small misalignments in the rotation axis.

The fourth stage is a buffer for the ultrahigh vacuum in the scattering chamber. Separating them is a collimating pinhole which is the defining aperture for the beam incident on the sample. The long distance traveled by the beam ( $\approx 90$  cm) and the narrowness of the pinhole ( $\approx 0.3$  mm) result in a highly collimated beam ( $\Delta\theta < 10^{-3}$  rad).

The major problem with the beam formation system has been the occurrence of momentary pressure bursts, especially in stage two. These result in anomalous drops in the beam intensity. The problem has been partially alleviated by installing a larger second stage diffusion pump, regulating the cooling water flows to all the diffusion pumps, and avoiding contaminated O-rings.<sup>35</sup> The problem still exists to some extent, however. Small pressure fluctuations also cause some noise in the beam intensity.

#### B. Scattering Chamber

The beam formation system is connected to the scattering chamber by a flexible bronze bellows to allow positioning of the beam. The chamber is pumped by a turbo-molecular pump backed by a small diffusion

pump to aid in pumping light gases. A titanium sublimation pump is also used, although it is not needed to maintain the ultimate pressure once it has been realized. The system is baked at  $\sim 100^{\circ}\text{C}$  and this yields a nominal pressure of  $\approx 3 \times 10^{-10}$  torr. The titanium sublimation pump is mounted in a Tee equipped with a jacket which is cooled with liquid nitrogen to condense contaminants whenever the sample surface is cooled. As shown in Figure 3, the scattering chamber has a number of ports for the beam, sample manipulators, windows, and electron optics. These ports are knife-edge flanges sealed by copper gaskets. A large flange on top has a rotary feed-through for the detector and a port for the ionization gauge. The bottom flange has a rotary feed-through for the sample holder motion, electrical feed-throughs, and a sealed liquid nitrogen inlet.

The sample holder is constructed so as to allow rotation of the sample about two mutually perpendicular axes, as shown in Figure 4. The holder is mounted on a rigid shaft which extends to outside of the chamber. Three teflon rings divide the feed-through area into two differentially pumped regions. Thus, the polar angle can be read directly on a vernier scale mounted on the outside. Changes in angle can be measured to a resolution of  $0.1^{\circ}$ , but absolute angle measurements are more difficult (see Section IV.C.). A mechanical rotary feed-through drives a chain and sprocket to rotate the bearing mounted inner section of the sample holder. This arrangement has a good deal more backlash, but the azimuthal angle scale is mounted directly on the holder and read through a window to insure accuracy.

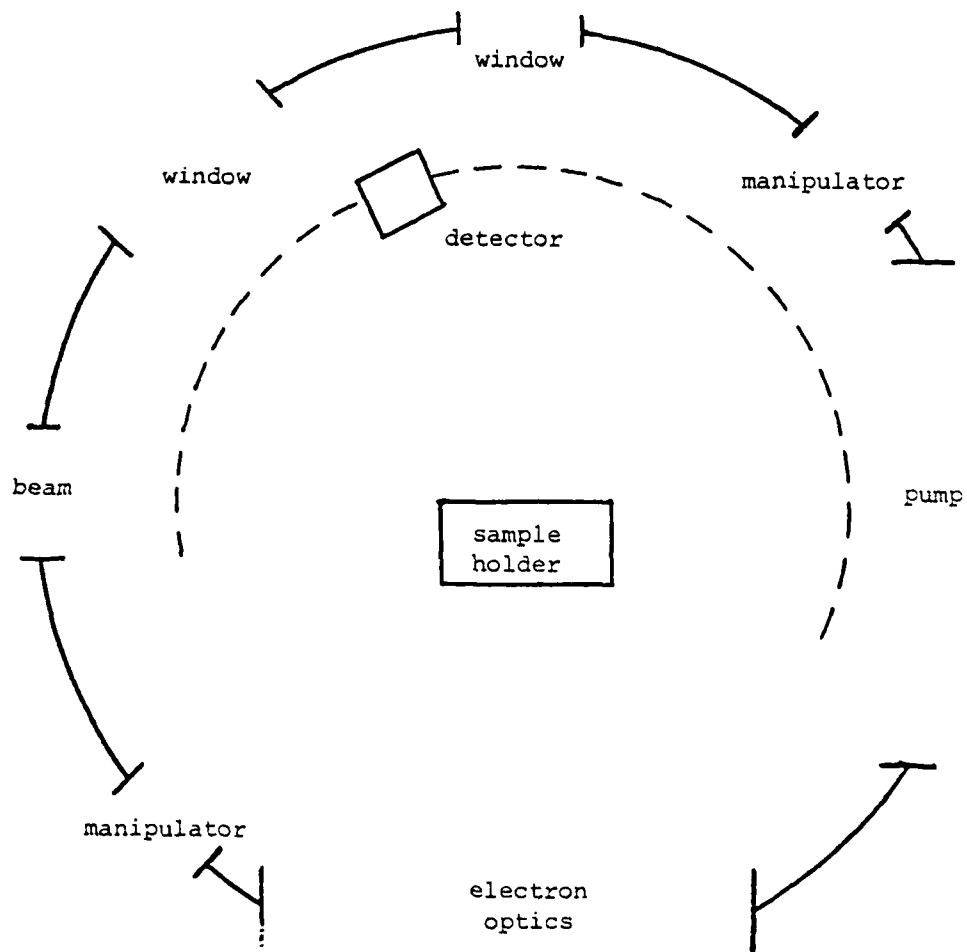


Figure 3. Top view of scattering chamber.

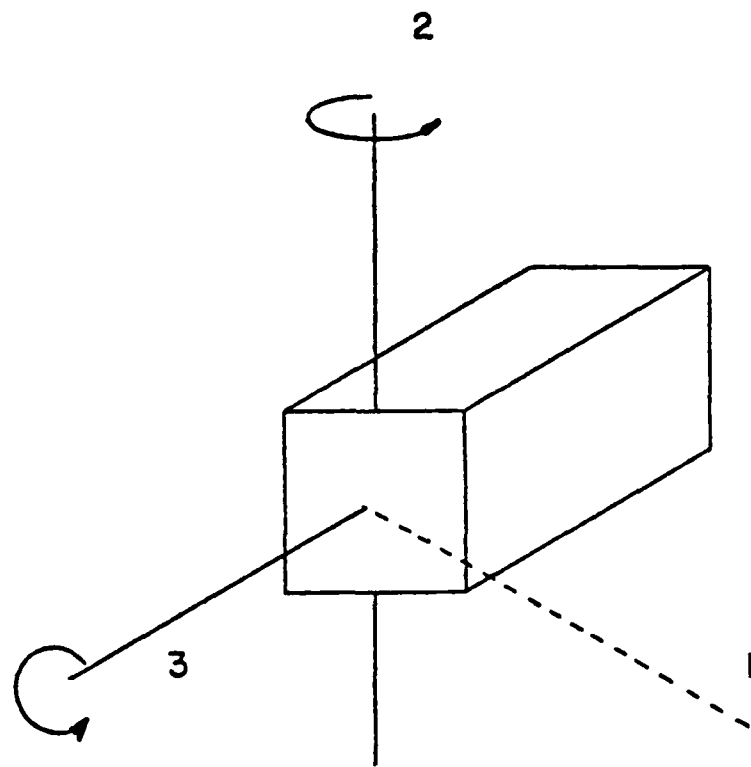


Figure 4. Sample holder geometry, showing incident beam direction (1), polar angle rotation (2), and azimuthal angle rotation (3).

It is often necessary to heat or cool the sample. Liquid nitrogen coolant is fed from outside through flexible bellows-type copper tubing into a copper reservoir block. This block is then maintained in good thermal contact with the sample holding mechanism. In work with the alkali halides, a rather massive sample holder is needed for cleaving in vacuum. Thermal contact is made in this case by sliding copper plates. The sample could be heated to ~450 K by a tantalum wire resistive heater encased in ceramic tubing.

For work with graphite samples, the large mass is not needed, even for the vacuum cleaved surfaces (see Section V.B.). Also, it is more common to heat the sample to high temperatures (~700 K) to clean the surface, a technique which requires low mass and good thermal isolation. This was accomplished by attaching a lightweight copper sample mount to a copper shaft which is held in suspension by eight thin stainless steel screws. Embedded in the sample mount is a Spectra-mat<sup>36</sup> heater. Thermal contact with the liquid nitrogen reservoir is made via a flexible copper braid; inserted between the braid and the shaft is a beryllia tab which conducts well at low temperatures for cooling and insulates at high temperatures for thermal isolation. The sample can be cooled to ~100 K and heated to ~700 K as measured by a chromel-alumel thermocouple mounted on the shaft.

A later refinement was the replacement of the eight thin mounting screws by three screws through a front, spring-loaded rocker plate. This arrangement, shown in Figure 5, allows the alignment of the azimuthal axis perpendicular to the polar axis and the beam. Alignment is discussed further in the following section.

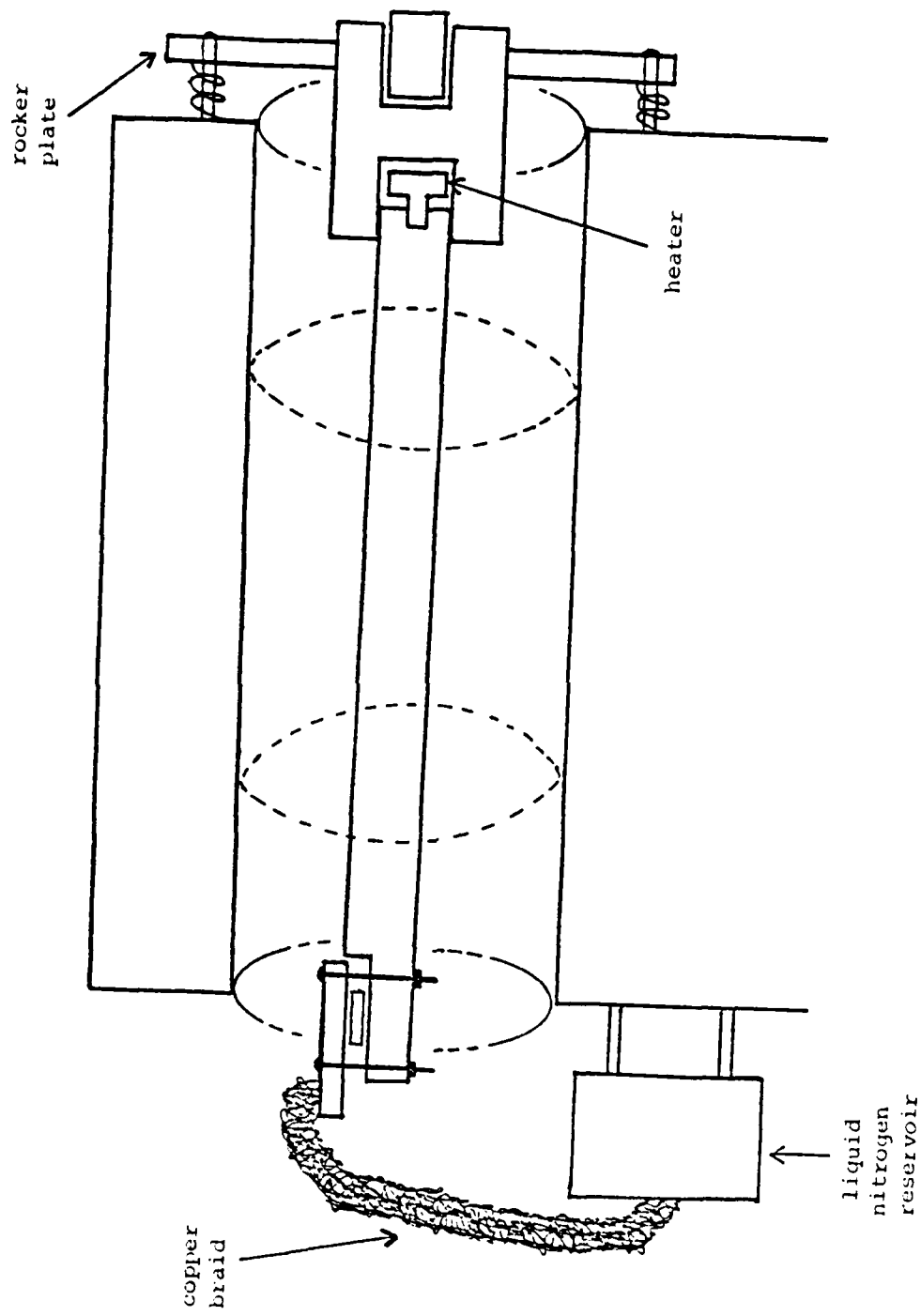


Figure 5. Cross-sectional view of sample holder used in graphite work.

The detector is mounted on a rigid shaft with a feed-through similar to the one on the sample holder. The detector swings along an arc with  $\approx 50$  mm radius, and it has a vertical travel of ~5 cm achieved by running the shaft through a flexible sealed bellows. This allows the detector height to be adjusted for optimum beam intensity and makes possible work with out-of-plane diffracted beams. The angle scale of the detector is mounted outside the vacuum and can be read to  $0.1^\circ$  (see Section IV.C.); changes in detector height can be measured to 0.01 mm.

The detector is a quadrupole mass spectrometer tuned to the mass of the incident atom ( ${}^4\text{He}$  or  ${}^3\text{He}$ ). The beam enters the ionizer box through a narrow (~0.8 mm  $\times$  3 mm) aperture. The ionized He atoms are selected out by the quadrupole filter and detected by an electron multiplier. The signal from the electron multiplier is fed via a current-sensitive preamplifier to the input of a lock-in amplifier provided with the chopper reference signal. The output of the lock-in amplifier is proportional to the intensity of the beam, but it is not calibrated to an actual flux since the intensities of the scattered beams can be normalized to incident intensity. Furthermore, many interesting phenomena depend only on relative changes in the scattered intensities.

#### C. Alignment

Although the goniometers of the sample and detector can be read to accuracies of  $\sim 0.1^\circ$ , true angle readings of this accuracy can only

be performed if the apparatus is properly aligned. Ideally, the following conditions should exist: The polar angle rotation axis and the detector rotation axis should be collinear. They should also be perpendicular to the beam and cross it at some point. The azimuthal axis should cross through the same point and be perpendicular to both the beam and the other axes when  $\beta = 0^\circ$ . Finally, also when  $\beta = 0^\circ$ , the surface should lie on the plane defined by the beam and the polar axis with its normal collinear to the azimuthal axis.

In practice, none of these conditions can be met perfectly. If extreme care is taken in leveling and positioning the beam (using finely threaded screws), aligning the axes (done optically, using shims and the rocker plate described above), and positioning the sample, the misalignments can be reduced to about  $\sim 1^\circ$  in the angles and  $\sim 0.1$  mm in the distances. The actual situation, however, is worse than this implies because the crystal surfaces are not flat planes but rather sets of misaligned facets.

The solution to this latter problem depends on the nature of the sample surface being studied, graphite being the most intractable. Therefore, these cases will be discussed individually in Section V. In each case, minimizing the misalignments described here is prerequisite to obtaining accurate results. A detailed exposition of the effects of misalignments and techniques chosen to deal with them is given in the Appendix.

#### D. <sup>3</sup>He Recirculation System

Most of the gas coming through the nozzle is retained in the first stage by the skimmer and pumped away. In the case of <sup>4</sup>He, the source gas is provided by a high-pressure cylinder of research grade (99.9995% pure) helium and the waste gas is simply vented to the atmosphere through the first stage forepump. This method cannot be employed for <sup>3</sup>He due to its high cost. Instead, a system was constructed to recirculate the used gas (except the small amount which goes through the skimmer). The gas is pumped into a reservoir for storage when not in use.

A schematic representation of this system is shown in Figure 6. The vent of the forepump is sealed from atmosphere with a valve, and the exhaust gases are fed through a zeolite trap immersed in liquid nitrogen. The <sup>3</sup>He is then further purified by a Randex<sup>37</sup> inert gas purifier consisting of a titanium "sponge" heated to 1100 K inside a quartz tube. The pure gas is then pressurized by a sealed refrigerator compressor capable of producing a source pressure of ~8 atm. The earlier alkali halide work was done with a sealed diaphragm<sup>38</sup> compressor that only produced ~4 atm with the amount of <sup>3</sup>He available. The pressurized gas, of course, is fed to the nozzle completing the cycle.

This recirculation system is interfaced with the <sup>4</sup>He source and the <sup>3</sup>He storage cylinders by systems of valves and pumps. With the valve separating the compressor from the nozzle closed, the <sup>4</sup>He is evacuated from the volume behind the nozzle. The valve to the <sup>4</sup>He

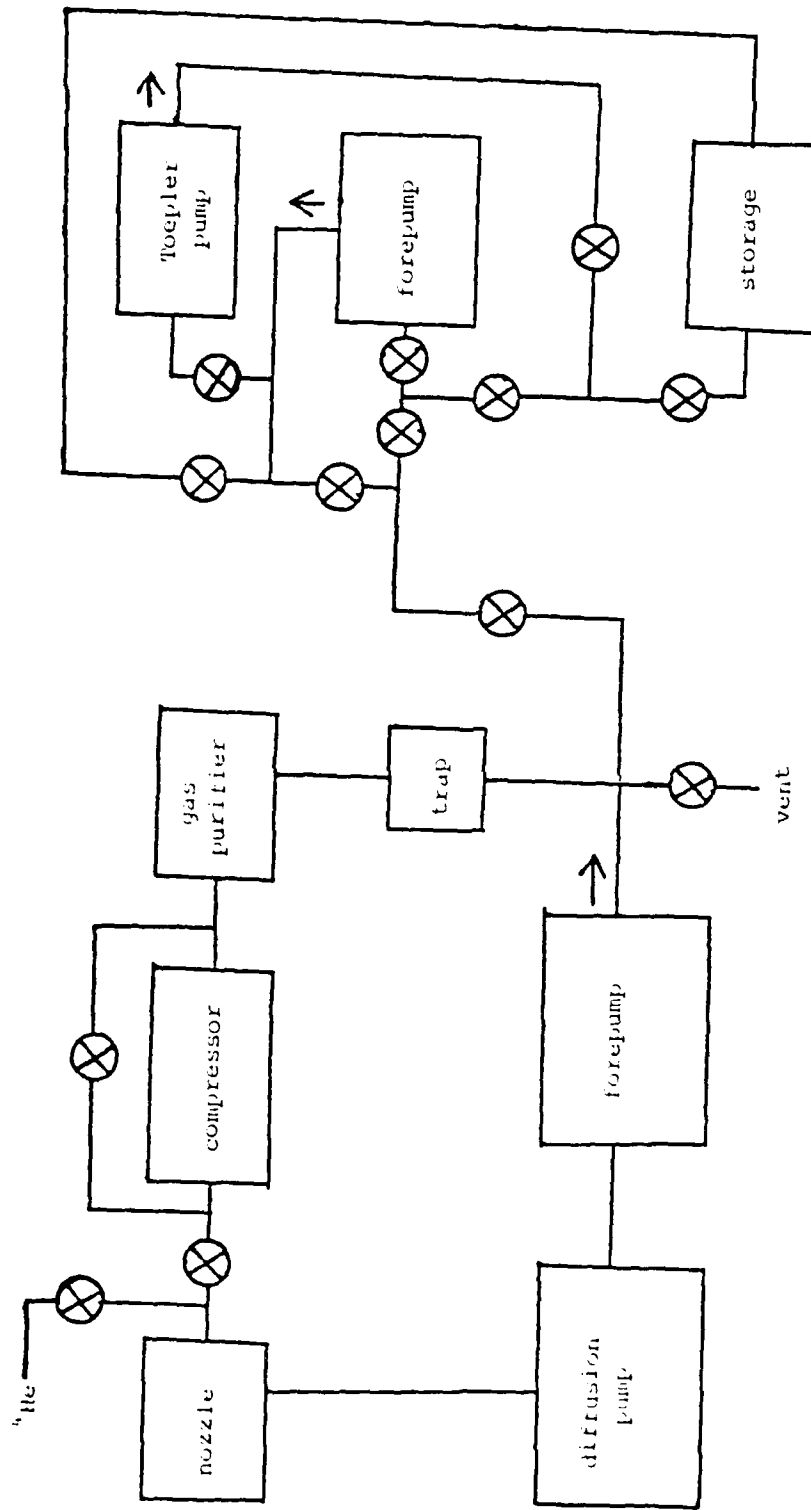


Figure 6. Schematic of the recirculation and storage system.

source is then closed and the valve to high-pressure output of the compressor opened. The pressure is regulated by a precision feedback valve between the compressor's output and input sides. When the run is completed, this valve is opened completely and the  $^3\text{He}$  is pumped out by a sealed mechanical pump with its vent connected to the storage cylinders. By manipulating the valves shown in Figure 6, the same pump is used to transfer the  $^3\text{He}$  from the storage volume into the recirculation system. Finally, a mercury-filled glass Toepler pump is used to transfer the  $^3\text{He}$  from the rather large volume at the vent of the mechanical pump to either the storage cylinders or recirculation system.

Great care must be taken to insure that no leakage of  $\text{He}$  occurs. All devices are sealed and leak-tested, the valves are bellows sealed, and plumbing connections are either brazed or swagelocked.<sup>39</sup> The loss rate of the  $^3\text{He}$  is known empirically to be  $\sim 0.031 \text{ l-atm/hr}$ , but it is not known how much of this goes through the skimmer. The maximum pressure generated by the compressor is a limiting factor in achieving a narrow velocity distribution. This is particularly a problem with  $^3\text{He}$  since it has a naturally broader distribution than  $^4\text{He}$ .<sup>40</sup> The velocity distribution characteristic of this system is  $\frac{\Delta v}{v} \approx 5\%$  FWHM for  $^3\text{He}$  at 77 K.

#### E. Low Energy Beam Production

The temperature of the gas at the nozzle essentially determines the average kinetic energy of atoms in the beam. Production of a very low-energy, long-wavelength beam is therefore dependent on cooling the

nozzle to very low temperatures. This is accomplished by cooling it with liquid helium. The problems of beam intensity and stability then need to be overcome.

The arrangement for cooling the nozzle is schematically illustrated in Figure 7. It is an adaptation of a "Heli-Tran"<sup>41</sup> refrigerator and is similar to the design of Skofronick and Pope.<sup>42</sup> Liquid helium in the dewar is pressurized and a slow, steady stream forced to the tip while a portion of the cold gas is fed back through an outer jacket for cryogenic shielding. The line is also vacuum-jacketed for improved efficiency and is rated for 0.75 l/hr average liquid helium consumption; the consumption rate in this application is typically  $\approx$  2 l/hr, probably due to the high thermal load of the warm He source gas.

The nozzle mount screws onto a copper "nosepiece" which in turn screws into the end of the "cold finger." They are both sealed with indium gaskets to promote good thermal contact. The source gas inlet, thermocouple wires, and heater wire are coiled around the cold finger. The heater originally supplied by the manufacturer was self-contained and attached to the tip of the cold finger. This did not regulate well and burned out frequently. A new heater wound directly onto the nosepiece is now installed, and works very well.

The heater power is regulated by a feedback circuit using the tip thermocouple signal to maintain a constant temperature. The early problems with this method (probably poor thermal contact of the heater) forced us to resort to temperature control simply by regulating the

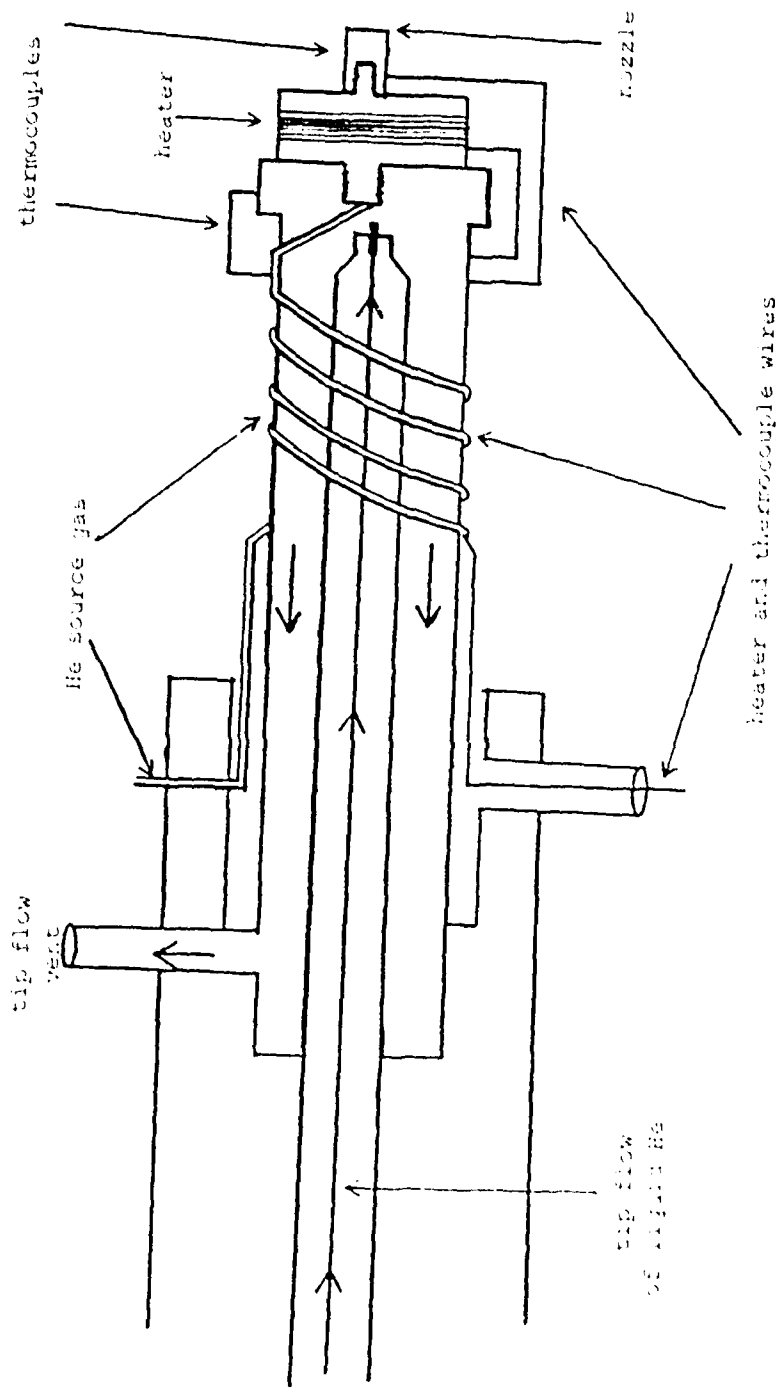


Fig. 7. Schematic of apparatus for cooling the nozzle to very low temperatures.

flow of liquid helium until the desired steady-state temperature is attained. This method worked fairly well but was susceptible to long-term temperature drifts. The most recent data were taken using the heater controller, which provides both short-term and long-term temperature stability quite well.

The lowest nozzle temperature attainable with this arrangement is  $\approx 10$  K. A reasonably intense beam can be obtained only if the source pressure is less than 1 atm. The nozzle also tends to clog readily, probably due to condensation in the aperture. A stable and intense beam is produced at  $\approx 20$  K with source pressures of  $\sim 1 \frac{1}{2}$  atm. The velocity distribution under these conditions is  $\approx 2 \frac{1}{2}$  % FWHM, only slightly poorer than the 77 K beam.

#### F. Electron Optics

The purpose of the electron optics in this system is primarily surface characterization rather than detailed studies. It has been used in the Auger mode to check the state of surface cleanliness and in the LEED mode to ascertain the directions of the surface lattice symmetry axes. A brief description of it will be given here.

The electron optics head is a PHI<sup>43</sup> Model 10-120. It consists of an electron gun, four hemispherical grids, and phosphor-coated collector. It is mounted on a bellows so that it can be moved in close to the sample to work on it and moved out of the way when not in use. The electron beam is at right angles to the atomic beam.

In the LEED mode, the head is controlled by a PHI<sup>43</sup> Model 11-020 electronics system. The electron beam energy is variable and the hemispherical grid system discriminates against inelastically scattered electrons. In the Auger mode, the beam energy is fixed at 3 keV. The hemispherical grids are used as a variable energy analyzer. A PHI<sup>43</sup> Model 11-500 Auger System Control sweeps the retarding potential through the desired values. An ac modulation is superimposed on this potential for lock-in detection. Actually, the lock-in monitors twice the modulation frequency in order to take the derivative of the electron energy distribution and remove the background.

## V. EXPERIMENTAL RESULTS

A. Alkali Halides

The alkali halide (001) surface has been studied very extensively by atomic beam scattering. Boato et al.<sup>8</sup> made a thorough study of <sup>4</sup>He diffraction from LiF. Meyers<sup>10,32</sup> and Liva<sup>44</sup> measured the binding energies of <sup>4</sup>He on LiF and NaF, respectively, using the vacuum cleaving technique pioneered by Houston.<sup>10,31</sup> Liva also experimentally confirmed<sup>45</sup> some of the theoretical scattering predictions of Chow and Thompson.<sup>13</sup> The author's work on the alkali halides consists in part of an extension of that work, employing many of the same methods (e.g., cleaving in situ). More accurate binding energies were measured for <sup>4</sup>He on LiF and NaF, and similar measurements were made for <sup>3</sup>He on LiF and NaF,<sup>46</sup> which had not been done before. This work is summarized in Section A.1. The band-structure of <sup>4</sup>He on NaF<sup>47</sup> was verified and matrix elements of some higher Fourier components of the <sup>4</sup>He/LiF atom-surface potential<sup>19</sup> were measured. A review of this work is presented in Section A.2. Data were taken to test the more recent scattering theories for both elastic scattering<sup>48</sup> and surface temperature dependence.<sup>49</sup> These studies are summarized in Section A.3.

The work was done on LiF and NaF crystals cleaved in vacuum. The surfaces contaminate over a period of several days, and then another cleave is made. Some of the data were taken with the surface cooled to ~100 K, but this does not make a dramatic difference in the scattering results.

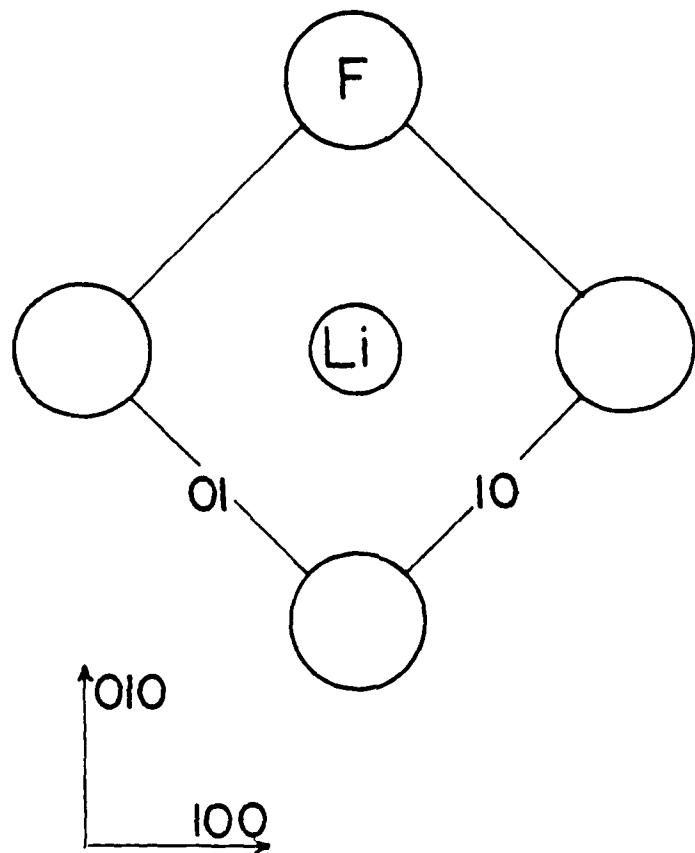


Figure 8. The LiF surface lattice (with basis vectors) and 3D crystal directions;  $\hat{\nu} = 0^\circ$  is defined to be along the (10) direction.

The surface structure of the alkali halide (001) plane is shown in Figure 8, along with the conventions being used to identify the coordinate axes. The rather corrugated surface yields strong, sharp diffracted beams. The samples were bars about 5 mm  $\times$  5 mm  $\times$  50 mm obtained from Harshaw Chemical Co.<sup>50</sup> To promote cleavability, some of the material was hardened by  $\gamma$  irradiation and some was supplied doped with OH<sup>-</sup> impurities ("X-ray grade").

### 1. Binding energies

As was discussed above, selective adsorption transitions can be observed as anomalies in the specular beam intensity. These anomalies are generally minima, an example of which is shown in Figure 9. The positions of these features can be used along with Equation. (6) to determine the binding energies  $E_j$  of the atoms physiosorbed on the surfaces. In order to determine more information about the same interaction potential, two isotopes of helium were used.

In the case of LiF, four bound-state energies were measured for  $^4\text{He}$  and two for  $^3\text{He}$ . Three energy levels were resolved for  $^4\text{He}$  on NaF and two for  $^3\text{He}$ . Several other weak minima were observed, but they could not be resolved well enough to calculate energy values. Preliminary results had been obtained previously<sup>10,44</sup> for  $^4\text{He}$  adsorption, as mentioned above.

Data for each energy level were generally taken on several cleaved surfaces. Readings were also taken with a variety of incident geometries. These are summarized in the form of plots in  $K_x$ - $K_y$  space for all four systems studied in Figures 10-13. Most of the data

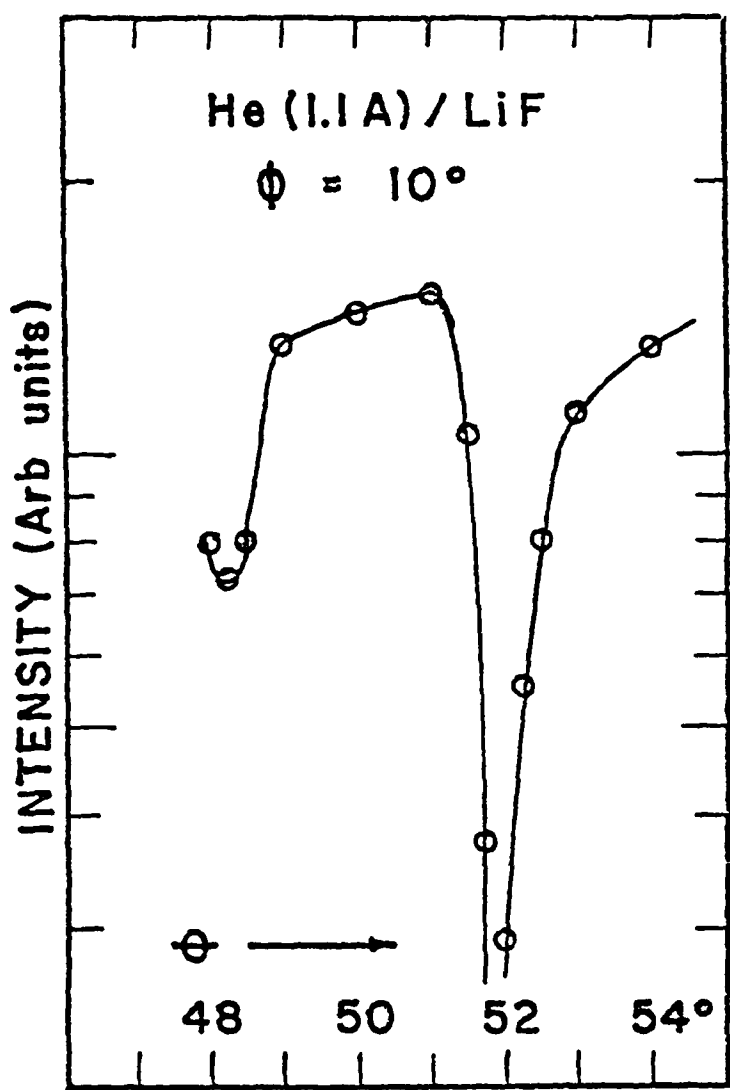


Figure 9. Typical specular intensity data for He on alkali halides, showing selective adsorption minima.

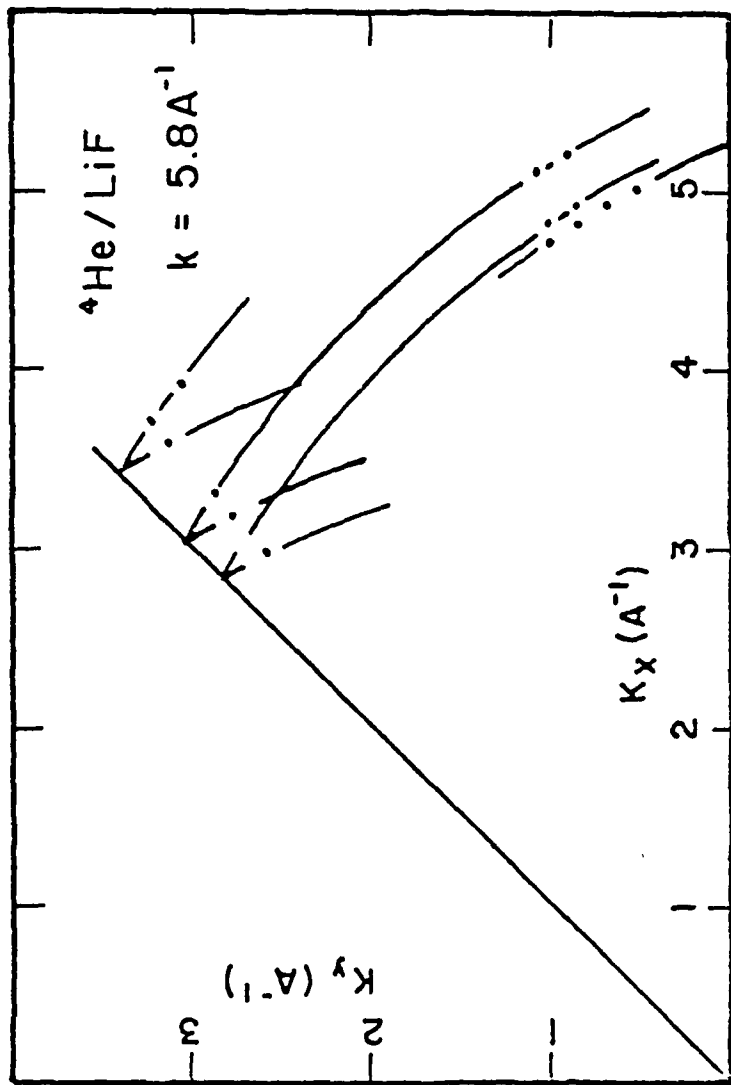


Figure 10. Selective adsorption loci in the  $K_x - K_y$  plane for  $^4\text{He}/\text{LiF}$ ; points are measured values, lines are circles described by equation (6) using average energies.

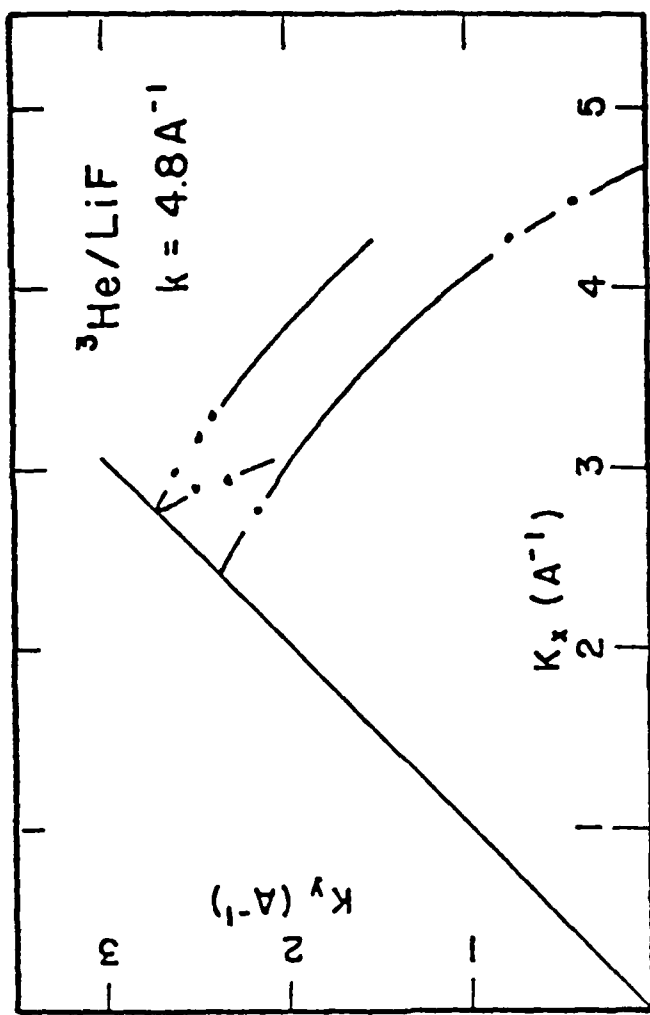


Figure 11. Selective adsorption loci for  ${}^3\text{He}/\text{LiF}$ ; points and lines have same meaning as in Figure 10.

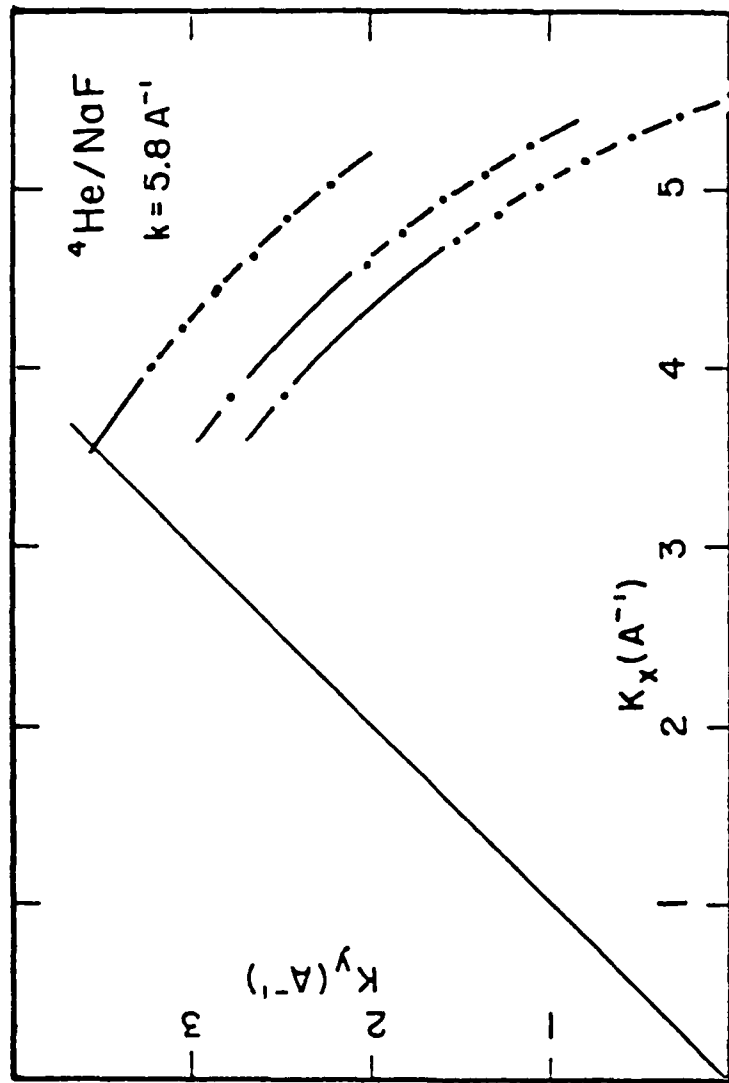


Figure 12. Selective adsorption loci for  ${}^4\text{He}/\text{NaF}$ ; points and lines have same meaning as in Figure 10.

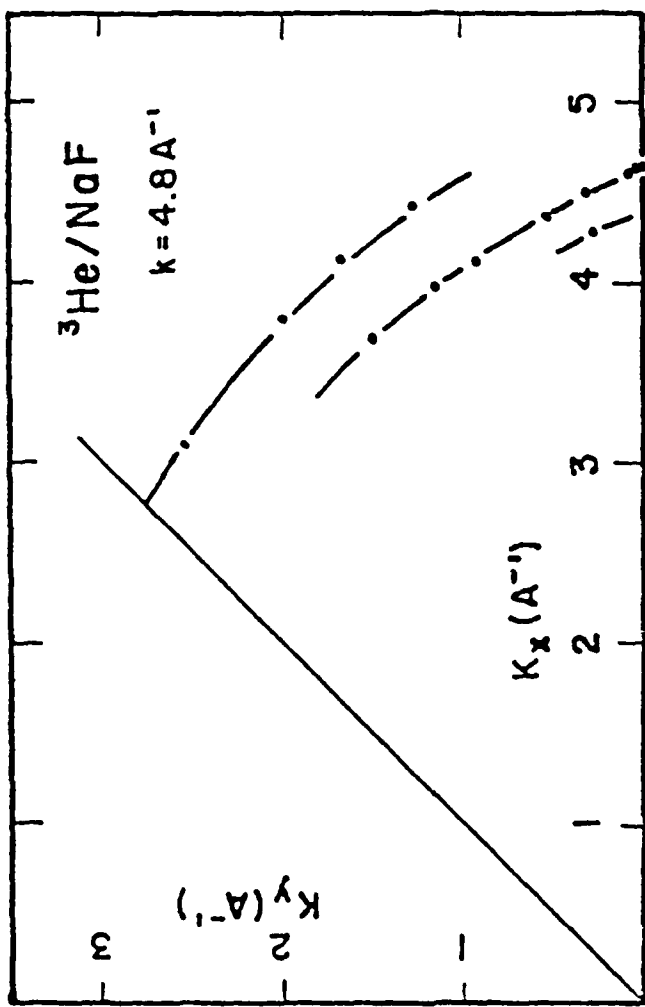


Figure 13. Selective adsorption loci for  ${}^3\text{He}/\text{NaF}$ ; points and lines have same meaning as in Figure 10.

were taken for the  $\bar{G}_{1,1}$  transition, with a few points for  $\bar{G}_{1,0}$ , because these are the shortest reciprocal lattice vectors and therefore yield the strongest selective adsorption features. Care was taken to avoid collecting data for transitions which are strongly influenced by band-splitting.

The average values obtained for the binding energies of  $^4\text{He}/\text{NaF}$  and  $^3\text{He}/\text{NaF}$  are summarized in Table 1. Also shown are the standard deviations and the number of determinations that were averaged. In Table 2, the same information for  $^4\text{He}/\text{LiF}$  and  $^3\text{He}/\text{LiF}$  is listed. The standard deviations in Tables 1 and 2 can be compared to the estimated uncertainty in the energy results. The latter quantity is calculated as the rms value of the individual errors caused by uncertainty in the measurements of  $\theta$ ,  $\phi$  and  $\Delta k$ . These quantities are taken to be  $\Delta\theta = \Delta\phi = 0.2^\circ$  and  $\Delta k = 0.03 \text{ \AA}^{-1}$ , resulting in  $\Delta E_j \approx 0.08 \text{ meV}$  for the cases of interest. This is comparable to the standard deviations found in the data. Use of this data to determine details of the interaction between helium atoms and alkali halide surfaces is discussed in Section VI.A.

A final word should be said about the zeroing procedures used for  $\theta$  and  $\phi$ . For  $\theta$ , the goniometer is zeroed relative to the symmetry directions of the azimuthal reflection patterns.  $\theta$  is initially zeroed relative to the sample holder face, but the cleaved crystal surface is not necessarily flat and parallel to this face due to faceting. This is compensated for by taking data in four crystallographically equivalent orientations separated by  $90^\circ$  in azimuth.

Table 1. Energy eigenvalues for He/NaF

Isotope	J	$\bar{E}_J$ (meV)	Std. dev. (meV)	No. of detns.
$^4\text{He}$	0	-4.92	0.05	7
$^4\text{He}$	1	-1.87	0.02	6
$^4\text{He}$	2	-0.54	0.05	8
$^3\text{He}$	0	-4.50	0.06	9
$^3\text{He}$	1	-1.38	0.1	9

Table 2. Energy eigenvalues for He/LiF

Isotope	J	$\bar{E}_J$ (meV)	Std. dev. (meV)	No. of detns.
$^4\text{He}$	0	-5.90	0.06	3
$^4\text{He}$	1	-2.46	0.05	4
$^4\text{He}$	2	-0.78	0.04	4
$^4\text{He}$	3	-0.21	0.02	4
$^3\text{He}$	0	-5.59	0.08	5
$^3\text{He}$	1	-2.00	0.06	4

The average polar angle of the four minima is then used to calculate  $E_j$ .

## 2. Matrix elements

While the binding energies contribute information about the laterally averaged atom-surface potential, they tell nothing about the periodic part, i.e., the  $\bar{G} \neq 0$  terms in Equation (7). The periodic part of the potential can be probed by the measurement of diffracted beam intensities or by determining matrix elements of the higher Fourier components. The many experimental and theoretical difficulties of the former method make the latter seem more attractive. The first observation of such band-structure effects was made by the author and co-workers for  ${}^4\text{He}$  scattering from NaF.<sup>47</sup> Quantitative results are presented here for  ${}^4\text{He}$  scattering from the (001) surface of LiF.

Figure 14 shows an example of the sort of data taken in these experiments. The two prominent maxima in the figure are selective adsorption signatures for the  $j = 0$ ,  $\bar{G}_{1,0}$  resonance [hereafter designated  $0(1,0)$  by convention] and the  $0(1,\bar{l})$  resonance. The specular intensity is measured as a function of polar angle for several values of the azimuth. Notice that the two maxima approach each other but remain always at least one degree apart in  $\phi$ . This angular separation corresponds to the band gap discussed in section III.C. Figure 15 is a plot of these resonance loci in  $K_x$ - $K_y$  space, demonstrating explicitly the deviations of the data from the degeneracy at the crossing of the free-atom curves. Nominal polar angles in this data have been shifted by  $-0.5^\circ$  to compensate for facetting by fitting them to the free-atom eigenvalues far from the crossing.

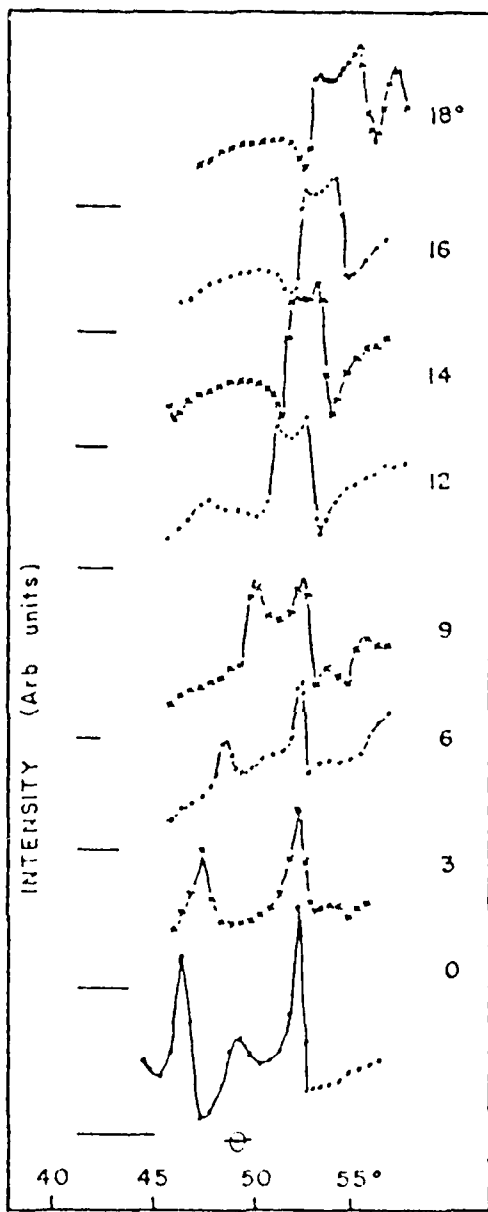


Figure 14. Scans of specular intensity vs. polar angle for a variety of azimuthal values showing the band splitting of two selective adsorption features (maxima in this case).

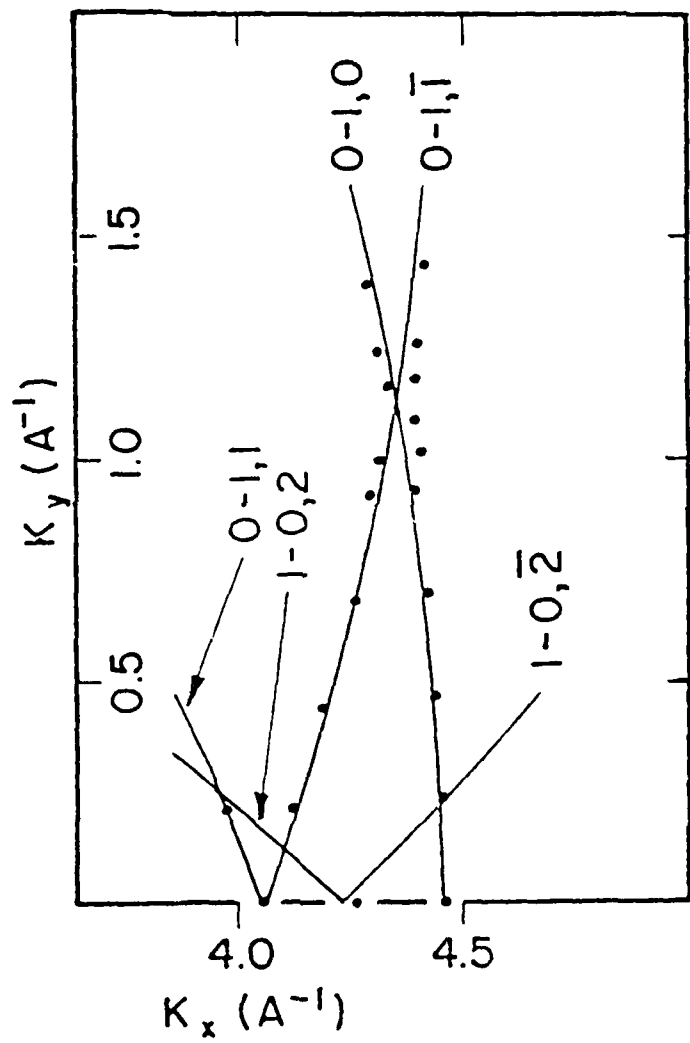


Figure 15. Data of Figure 14 plotted in  $K_x-K_y$  plane, showing the splitting; lines are calculated free particle circles (impurity  $\sim 0\%$ ).

The  $0(1,0)$  and  $0(1,\tilde{1})$  resonances are strongly coupled by the  $v_{0,1}(z)$  Fourier component. The magnitude of the splitting can be used to calculate the matrix element  $\langle 0|v_{0,1}|0\rangle$ . The result of this calculation, done in collaboration with W. Carlos,<sup>19,29</sup> is presented in Table 3. Also shown there are the experimental matrix elements for all cases which were seen to give rise to observable splittings. Detailed data for these matrix elements have been presented elsewhere.<sup>19</sup> These matrix element values have some interesting implications for theoretical pairwise sum calculations. This is discussed more fully in Section VI.A.

### 3. Comparison with scattering theories

It was pointed out in Section III.D that the calculations of Weare et al.<sup>15</sup> and Garcia et al.,<sup>16</sup> done within an elastic scattering framework, predict both minima and maxima in the specular intensity. Minima are predicted if the resonance state is coupled strongly to both the incident beam and an open diffraction channel, while maxima are expected for weak coupling. This was tested for  ${}^4\text{He}$  scattering from the (001) surface of LiF. Figure 16 is a scan of specular intensity as a function of azimuthal angle at  $\theta = 70^\circ$  (nominal reading). The selective adsorption features seen in the data are in quite good agreement with the theoretical predictions, the strongly coupled  $(0,1)$  states being the deep minima.

The status of inelastic scattering theory is on a less firm basis. The effects of the surface temperature in reducing elastic scattering

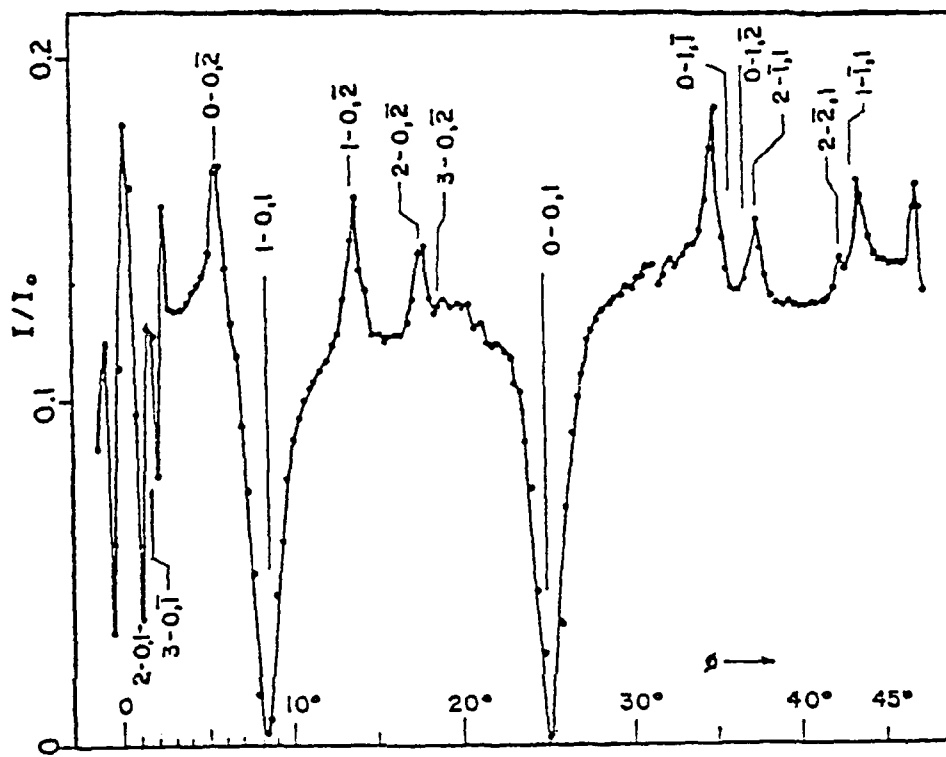


Figure 16. Scan of specular intensity vs. azimuthal angle at  $\theta = 70$  (nominal), showing resonance lineshape for different transitions.

Table 3.  ${}^4\text{He}/\text{LiF}$  matrix elements in meV

$\langle 0   v_{01}   0 \rangle$	$0.25 \pm 0.05$
$\langle 1   v_{01}   1 \rangle$	$0.20 \pm 0.10$
$\langle 0   v_{11}   0 \rangle$	$0.10 \pm 0.05$
$\langle 1   v_{11}   1 \rangle$	$<0.05$

intensity, for example, is subject to much debate. The standard methods employ a Debye-Waller factor<sup>51</sup> to account for these losses. Beeby<sup>52</sup> claims that the momentum transfer must be modified by the acceleration due to the attractive well, while Goodman<sup>53</sup> doubts that the Debye-Waller relation is well established for gas-surface scattering.

To examine these questions, a study of  ${}^4\text{He}$  scattering from the (001) surface of NaF as a function of surface temperature was undertaken. The major results are summarized in Figure 17, which is a plot of the logarithm of the ratio of intensities at two surface temperatures versus  $\cos^2 \theta$ . This plot should be linear in the context of the Debye-Waller formalism since

$$I(T) = I_R e^{-<(\bar{u} \cdot \Delta k)^2>} \quad , \quad (10)$$

where  $I_R$  is the intensity due to a rigid lattice,  $\bar{u}$  is the atomic displacement, and  $\Delta k$  is the momentum transfer which equals  $2k \cos\theta$  in magnitude for the specular beam. It is clear that such a linear relation does not hold for the data in Figure 17 and that a more sophisticated model is needed to account for the effects of surface vibrations

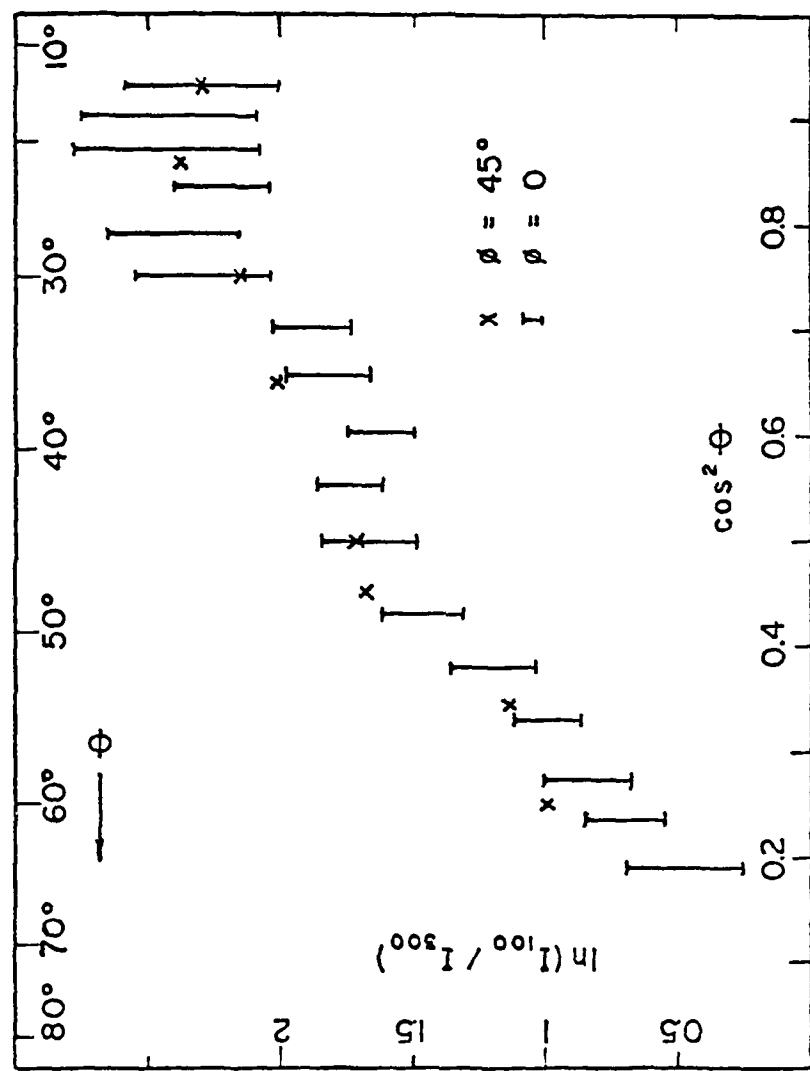


Figure 17. Specular intensity ratio for two temperatures, plotted vs.  $\cos^2 \theta$  to test Equation (10).

in gas-surface scattering. If the linear portion of the curve (roughly  $\theta > 45^\circ$ ) is interpreted as being a good approximation to Debye-Waller theory, then a surface Debye temperature of  $\theta_D = 411$  K is calculated. From intensity versus surface temperature data at fixed angle ( $\theta \approx 45^\circ$ ), a value  $\theta_D = 425 \pm 20$  K is obtained. The two values agree rather well, and also compare well with the value of Williams et al.<sup>7</sup> ( $\theta_D = 416$  K) for He/NaF.

### B. Graphite

Helium on the graphite basal plane is an extremely interesting system to study. As mentioned in Chapter I, this system has been used to carry out detailed thermodynamic studies of physisorbed films gaining information on phase transitions in two dimensions.<sup>54</sup> Graphite has a layer structure involving weak Van der Waal's interlayer forces. This layer structure allows preparation of samples having large surface area (by means of exfoliation) for use in adsorption and phase transition studies. The saturated covalent bonding within the layers renders the graphite basal phases chemically quite non-reactive, a desirable property experimentally since it retards surface contamination. The crystallographic structure of the basal plane is shown in Figure 18, along with the six lowest-order reciprocal lattice vectors. The hexagonal symmetry of the surface mesh is apparent, and the labelling conventions used herein (Reference 24 uses a different convention) are shown there. A further convention is to choose  $\phi = 0^\circ$  along the (1,1) reciprocal lattice vector. Further motivations for employing graphite in scattering experiments are its theoretical interest<sup>55</sup> and possible technological uses, e.g. as a substrate for catalysts.<sup>56</sup>

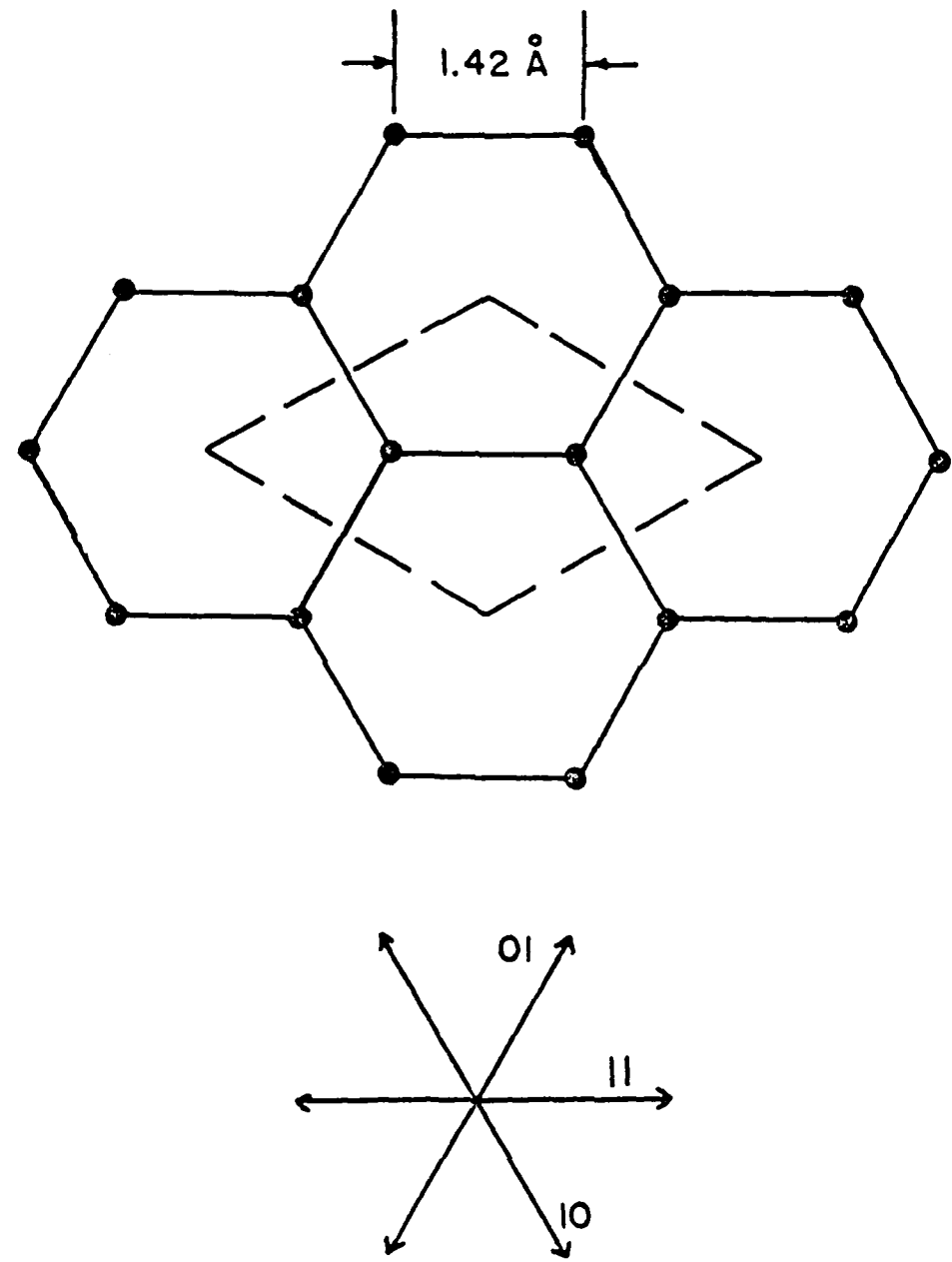


Figure 18. The graphite basal plane structure, showing the unit cell and the first-order reciprocal lattice vectors.

Although many workers have used graphite for physisorption studies, employing a variety of research techniques,<sup>57</sup> only Boato et al. besides ourselves have used helium beam scattering for this purpose. They used a 63 meV incident beam to study the surface corrugation by means of diffraction intensities.<sup>58</sup> They also used a 17.3 meV beam to measure the binding energies<sup>59</sup> and matrix elements<sup>24</sup> of <sup>4</sup>He on graphite.

The remainder of this section presents the results of the author's study of helium scattering from graphite. In the first subsection, methods of surface preparation and their effect on the scattering results are discussed. Results for the binding energies of <sup>4</sup>He and <sup>3</sup>He on graphite,<sup>26</sup> done at 17.3 meV incident energy, are summarized in the next subsection. In Subsection 3, some interesting phenomena associated with level crossings are examined, at both 17.3 meV and 4.7 meV incident beam energies. In the final subsection, experimental evidence for inelastic scattering processes is presented, primarily at 4.7 meV incident energy and lower.

### 1. Sample preparation

Samples for use in atomic beam scattering must be natural single crystals. Grafoil,<sup>60</sup> which is an exfoliated form of graphite much used in thermodynamic work, is not suitable for use in beam scattering due to its crystallographic disorder. The same is true even of the pyrolytic graphites, which are highly ordered with respect to the c-axis orientation but completely disordered around it. The natural crystals used in this work are flakes about 4 mm  $\times$  4 mm  $\times$  0.1 mm in size. They do not exhibit a single flat crystal plane but rather a mosaic of

facets demarcated by fault lines. These facets are aligned well in azimuthal angle but not in polar angle. The largest facets are of order 1 mm<sup>2</sup> in area.

The crystals in their natural state are embedded in a matrix of calcite and silica. A quantity of this material, found in Ticonderoga (New York State) by Dr. T. S. Noggle of Oak Ridge National Laboratory, was kindly sent to us. The graphite is extracted by attacking the matrix first with hydrochloric and then with hydrofluoric acid. Drs. G. Wagoner and M. B. Dowell of Union Carbide Corporation and Dr. G. Felcher of Argonne National Laboratory have also sent us Ticonderoga graphite flakes, already extracted, that were used in this work.

The flakes are first cemented with "Vacseal"<sup>61</sup> onto copper mounts that fit into the sample holder. One of two methods for cleaning the surface are then employed. Most of the data were taken using surfaces which were cleaned by heat treatment. The sample is cleaved in room air by peeling off graphite layers with adhesive tape. Several cleaves may be made until a surface with relatively large and well-aligned facets is obtained. It is then installed in the scattering chamber and the system is pumped down and baked. The sample is heated to about 700 K for several hours concurrent with the end of the bake. The heating occasionally had to be carried out twice before a strong specular reflection was seen.

The second method of surface preparation is cleaving the crystal in vacuum. This is done by affixing a thin cover glass to the mounted sample with epoxy. After the ultra-high vacuum is attained, the glass

is detached along with a layer of graphite by use of a manipulator. The scattered intensities, linewidths, and energy levels are essentially the same for both methods of surface cleaning. The scattered intensities are comparable to those seen using alkali halides, but only if the graphite surface is cooled to ~100 K. Cooling gives rise to a dramatic increase in elastic scattering from graphite, as opposed to the alkali halides, and all work described herein was done on a cold surface. The resonance linewidths are only slightly greater for graphite than for alkali halide scattering. Unlike the alkali halides, however, the intensities and linewidths were both stable with time for graphite using either surface cleaning technique.

A major disadvantage of cleaving in situ is that only one cleave can be made. Thus, no improvement is possible (without opening the chamber) if the facets are small or badly misaligned. The misalignment of the facets in polar angle is, in fact, a problem even for relatively good surfaces. The magnitude of the misalignment is assessed by reflecting laser light from the surface. This produces an irregular pattern of reflected light of varying size depending on the quality of the sample. The best samples produce a pattern subtending a solid angle of about  $10^{-4}$  sr, while the worst are about  $10^{-2}$  sr. For comparison, a polished copper sample mounting plug gives about  $10^{-6}$  sr. Thus it is evident that even the best crystals are far from optically flat. The individual facets, however, are flat and it is only necessary that a single facet be larger than the beam's projection on the surface. It is also necessary, of course, that the

beam be aimed properly to impinge on the large facet. This is accomplished by adjusting the height and lateral position of the beam until a single, strong specular peak is observed. An example is shown in Figure 19, obtained by scanning the detector through the specular beam with fixed incidence angles.

Since the chosen facet is not necessarily parallel to the sample holder, there is still the problem of zeroing the polar angle. The method described in Section V.A.1 is not feasible because the rotation involved would usually move the chosen facet out of the beam. The azimuthal zero, however, is determined for graphite in the same manner as for the alkali halides, described in Section V.A.1.

The zero of the polar angle is determined by first writing

$$\hat{\theta} = \hat{\theta}' - \hat{\theta}'_0 , \quad (11)$$

where  $\hat{\theta}$  is the true polar angle,  $\hat{\theta}'$  is the scale reading, and  $\hat{\theta}'_0$  is the scale reading when  $\hat{\theta} = 0^\circ$ . Then, detector angle measurements,  $\hat{\theta}_d$ , are made for a set of nominal polar angles,  $\hat{\theta}'$ . A plot of  $\hat{\theta}_d$  versus  $\hat{\theta}'$  is made and extrapolated to  $\hat{\theta}_d = 0^\circ$ . This intercept effectively determines the scale reading zero correction  $\hat{\theta}'_0$ . These plots turn out to be very nearly straight lines, as seen in the example shown in Figure 20. Typical linear regression correlation coefficients<sup>61</sup> differ from unity by only about  $5 \times 10^{-3}$ . The slopes of the plots vary from about -1.05 to -2.05, an effect caused by the various misalignments described in Section IV.C. A detailed treatment of the effects of apparatus misalignment on the polar angle zeroing procedure is given in the Appendix.

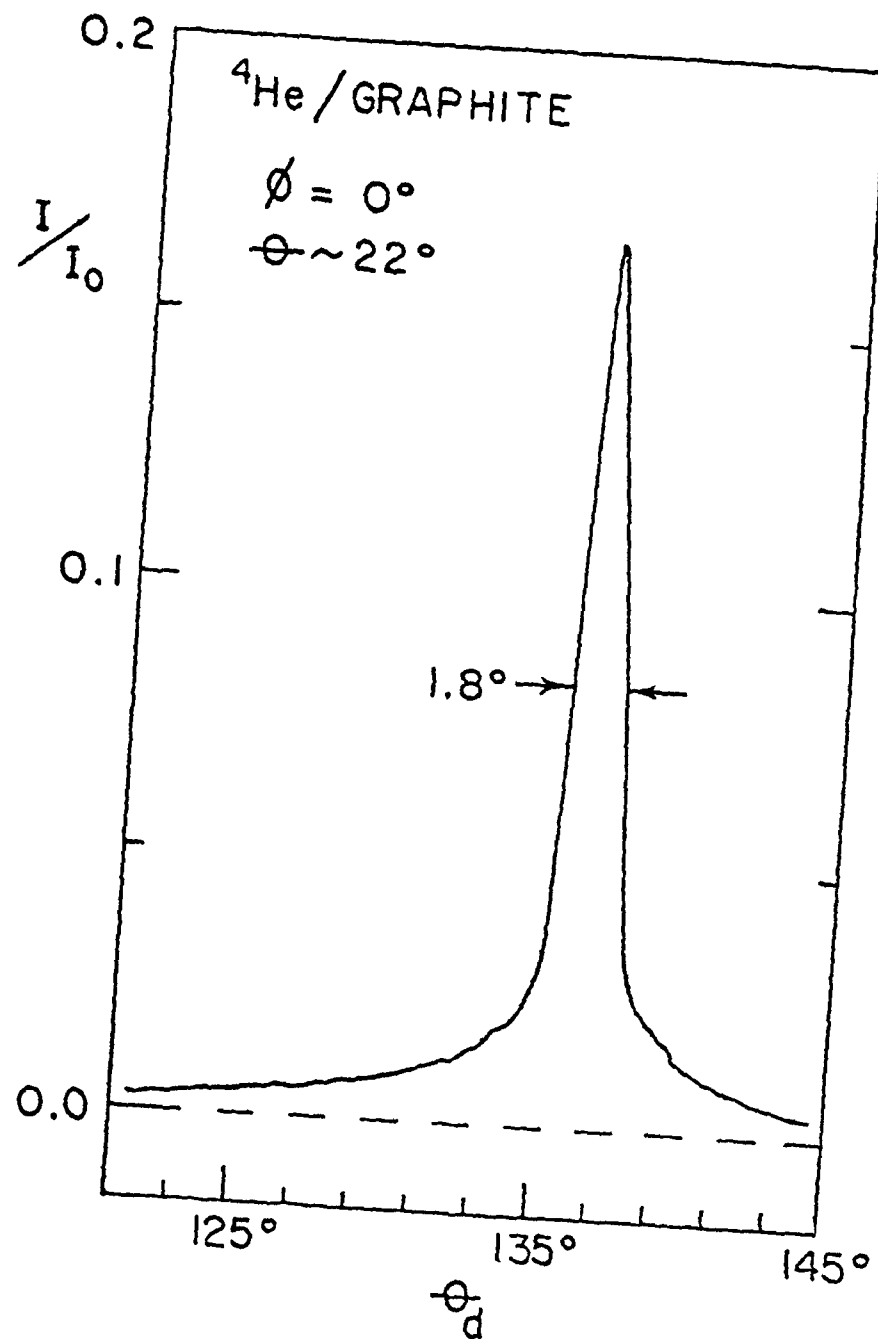


Figure 19. Profile of a specularly reflected beam, taken by scanning the detector with the sample fixed.

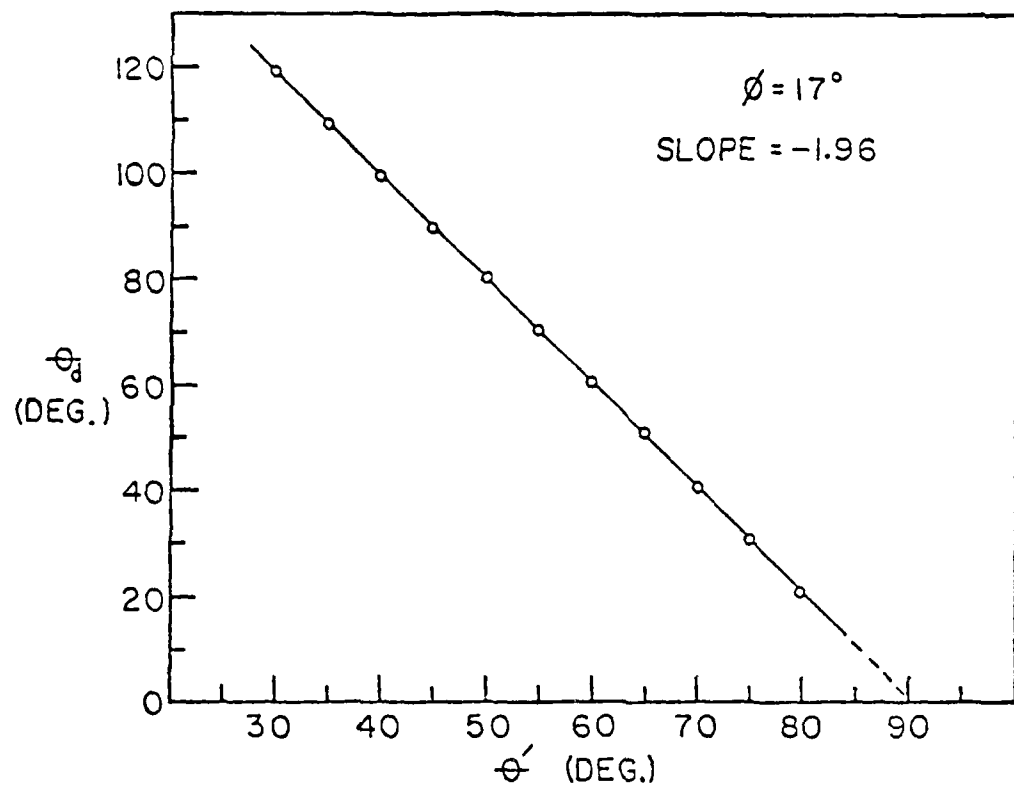


Figure 20. Plot of  $\theta_d$  vs.  $\theta'$ , used to determine the polar angle zero.

## 2. Binding energies

An example of the scattering data, demonstrating selective adsorption minima in the specular intensity, is shown for  $^4\text{He}$  on graphite in Figure 21. Although the actual scattered intensities are not identical for all samples due to surface imperfections, the positions of the minima are reproducible within experimental error. This is sufficient for present purposes, since these positions are the input for calculation of the energy eigenvalues. The data in this section were taken on three surfaces, one vacuum-cleaved and two heat-treated, and no systematic variations were seen from sample to sample.

Five bound state energy levels were resolved for  $^4\text{He}$  on graphite. Energy levels were measured for transitions via each of the three shortest reciprocal lattice vectors available, namely  $\bar{G}_{0,1}$ ,  $\bar{G}_{1,0}$ , and  $\bar{G}_{1,1}$ . The locations in  $K_x$ - $K_y$  space where data were taken are summarized in Figure 22. Notice that the data need be taken over only a  $30^\circ$  interval in  $\phi$  due to the sixfold symmetry of the lattice.

The average binding energies for all  $^4\text{He}$  data are summarized in Table 4. Also tabulated there are the standard deviation and number of determinations for each energy level. The earlier results of Boato et al.<sup>59</sup> are listed there for comparison. Note that there is a systematic disagreement between the two sets of eigenvalues. Although this was initially a source of concern, the discrepancy can be traced to the procedure used in zeroing the polar angle of the Genca apparatus, and when correction is made for this, excellent agreement with the present results is obtained.<sup>24</sup>

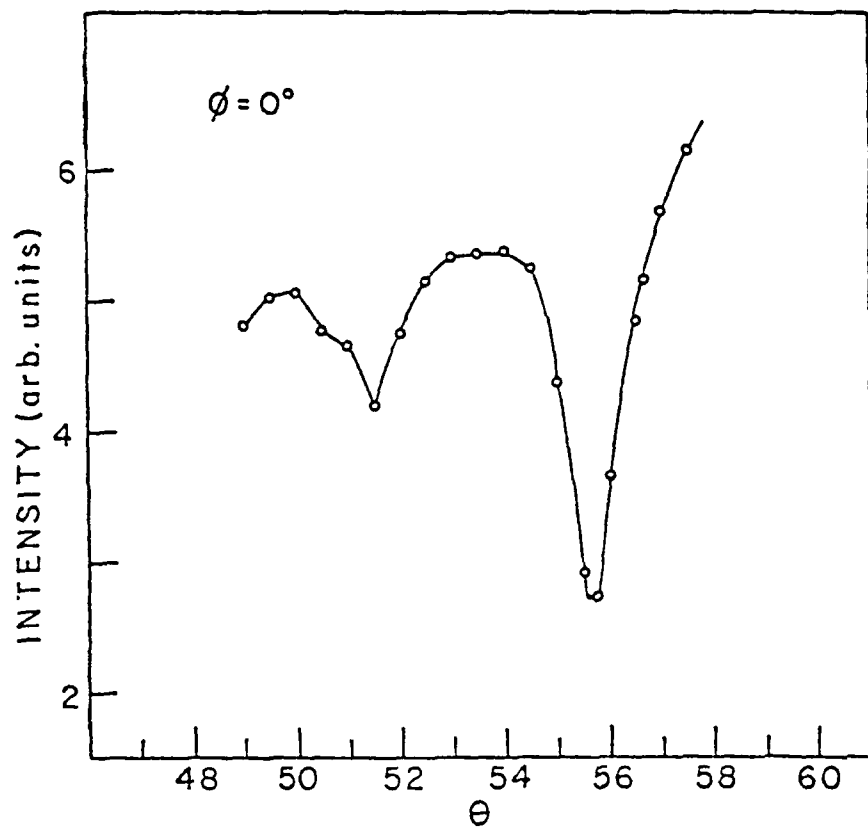


Figure 21. Typical specular intensity data for He/graphite, showing selective adsorption minima.

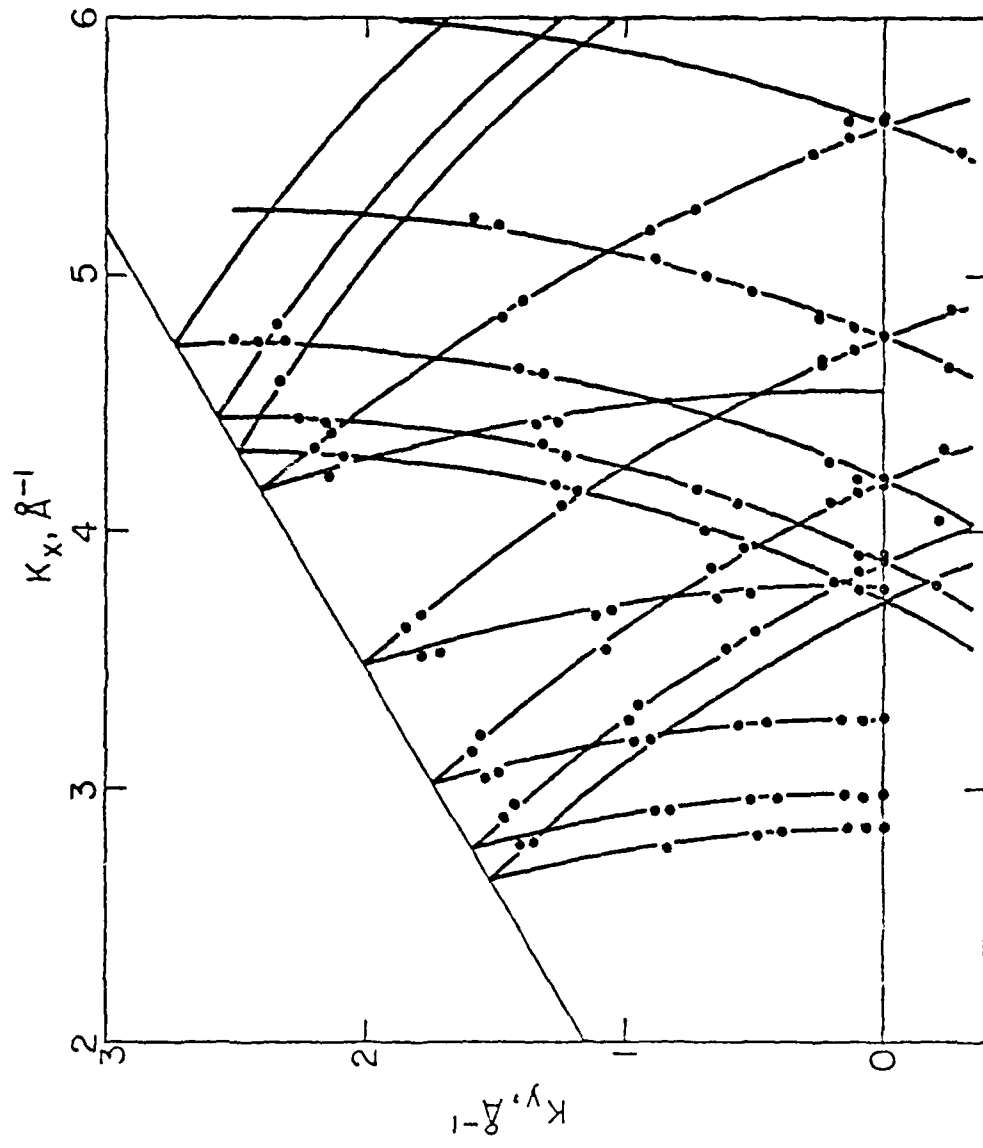


Figure 22. Selective adsorption loci in the  $K_x$ - $K_y$  plane for  $^3\text{He}/\text{graphite}$ ; points are measured values, lines are circles described by Equation (6) using average energies.

Table 4. Energy eigenvalues for  $^4\text{He}/\text{graphite}$ .

j	$\bar{E}_j$ (meV)	Std. dev. (meV)	No. of detns.	Results of Boato et al. <sup>a</sup> (meV)
0	-12.06	0.13	25	-11.75
1	- 6.36	0.11	30	- 6.13
2	- 2.85	0.10	33	- 2.65
3	- 1.01	0.09	32	- 0.86
4	- 0.17	0.06	18	- - -

<sup>a</sup>From Reference 59

For  $^3\text{He}$  on graphite, only three energy levels were resolvable. This is probably due to the higher velocity spread in the  $^3\text{He}$  incident beam. Its lighter mass causes the  $^3\text{He}$  to be less strongly bound to the surface, also making it more difficult to observe high j bound states. The average binding energies of the observed states are presented in Table 5, along with their standard deviations and the number of determinations made for each. The data were taken over several areas of  $K_x-K_y$  space, as shown in Figure 23, and were again taken for transitions induced by each of the three important reciprocal lattice vectors.

As seen in Figures 22 and 23, no systematic trends are apparent from one region of  $K_x-K_y$  space to another. In general, crossings of strongly coupled states were avoided in taking the data. The standard deviations listed in Tables 4 and 5 compare favorably with the estimated uncertainty,  $\Delta E_j \approx 0.12$  meV, calculated as in Section V.A.1. The use

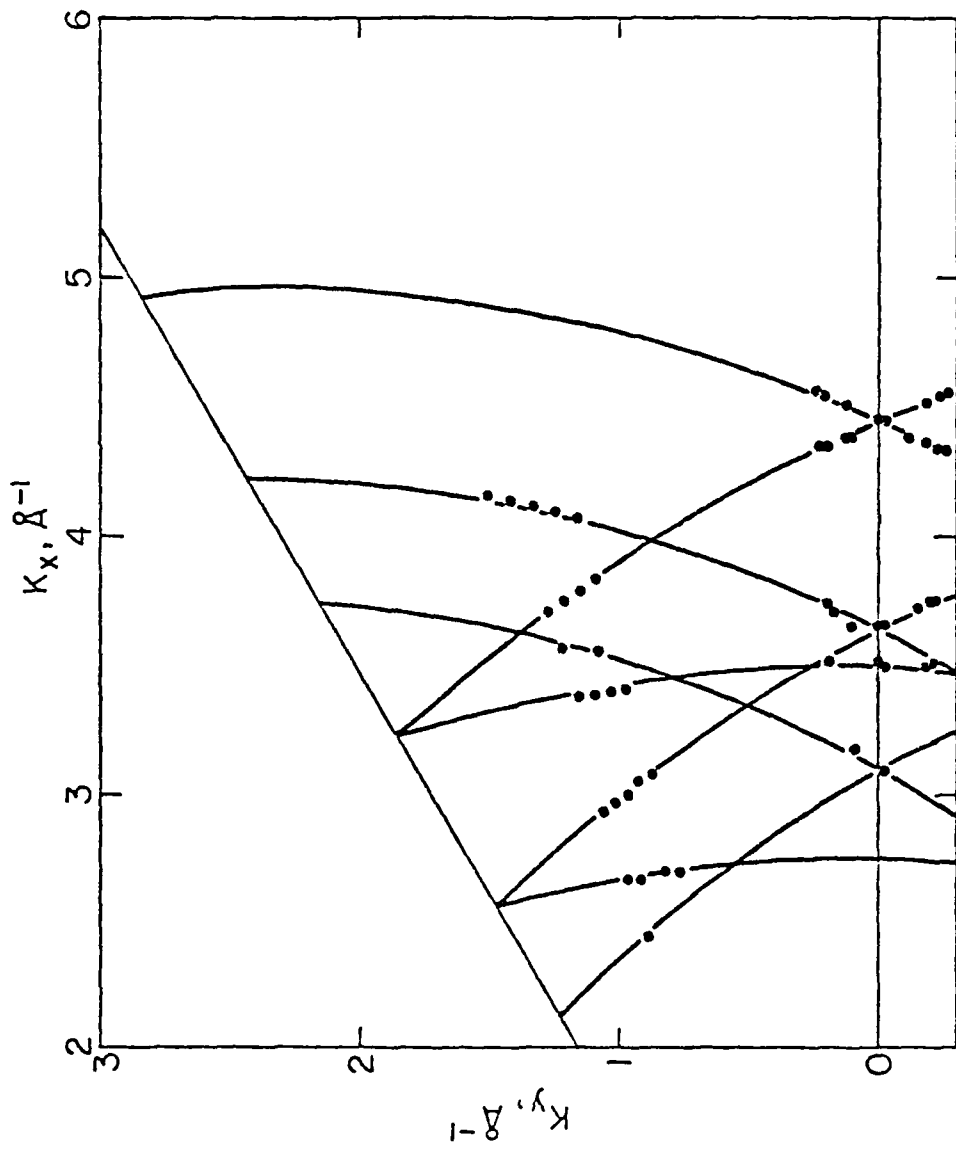


Figure 23. Selective adsorption loci for  $^3\text{He}/\text{graphite}$ ; points and lines have same meaning as in Figure 22.

Table 5. Energy eigenvalues for  $^3\text{He}/\text{graphite}$ 

$j$	$\tilde{E}_j$ (meV)	Std. dev. (meV)	No. of detns.
0	-11.62	0.09	25
1	- 5.38	0.13	25
2	- 1.78	0.11	5

of these results in determining  $v(z)$  for helium on graphite is discussed in Section VI.B. Also presented there is an assessment of the validity of the free-atom approximation used in calculating the eigenvalues from the resonance positions and Equation (6).

### 3. Second-order resonances and splittings

#### a. Using 17.3 meV incident beam.

As pointed out in Section III.D, several interesting effects can occur along with band splitting when strongly coupled resonances cross. Figure 24 presents some specular intensity data plotted as a function of azimuthal angle for various fixed values of polar angle. Boato et al.<sup>24</sup> observed a case similar to this at somewhat higher energy. The resonance loci of Figure 24 are plotted in  $K_x-K_y$  space in Figure 25, along with curves representing the free-atom results. The data are shifted in polar angle to compensate for facetting as in Section V.A.2, in this case, to fit eigenvalues plus calculated band-structure corrections.<sup>29</sup> The data in Figure 24a is plotted in region "a" of

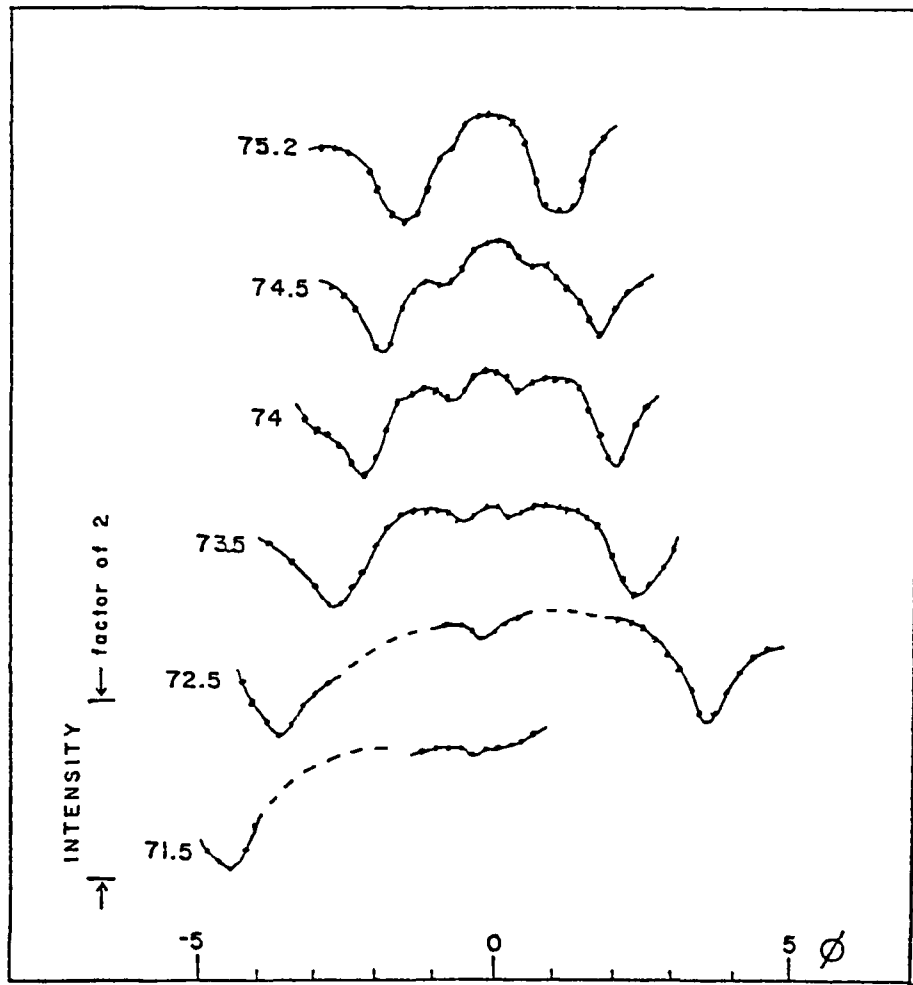


Figure 24a. Specular intensity vs. azimuthal angle at 17.3 meV for several values of polar angle corresponding to region "a" of Figure 25.

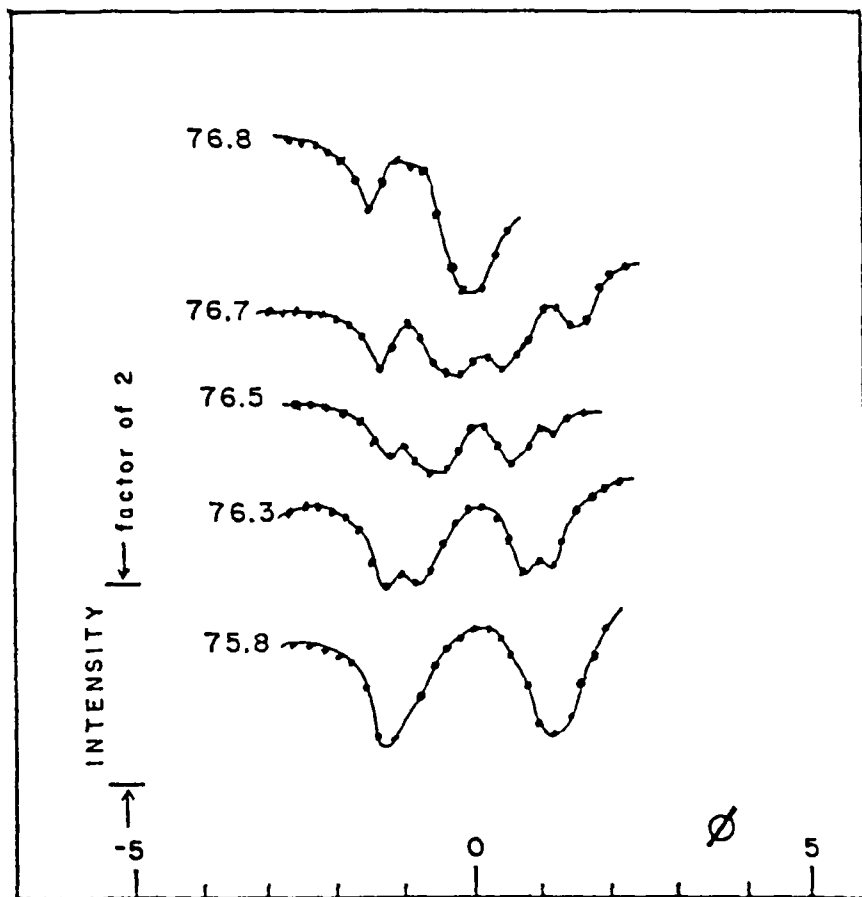


Figure 24b. Same as Figure 24a except corresponding to region "b" of Figure 25.

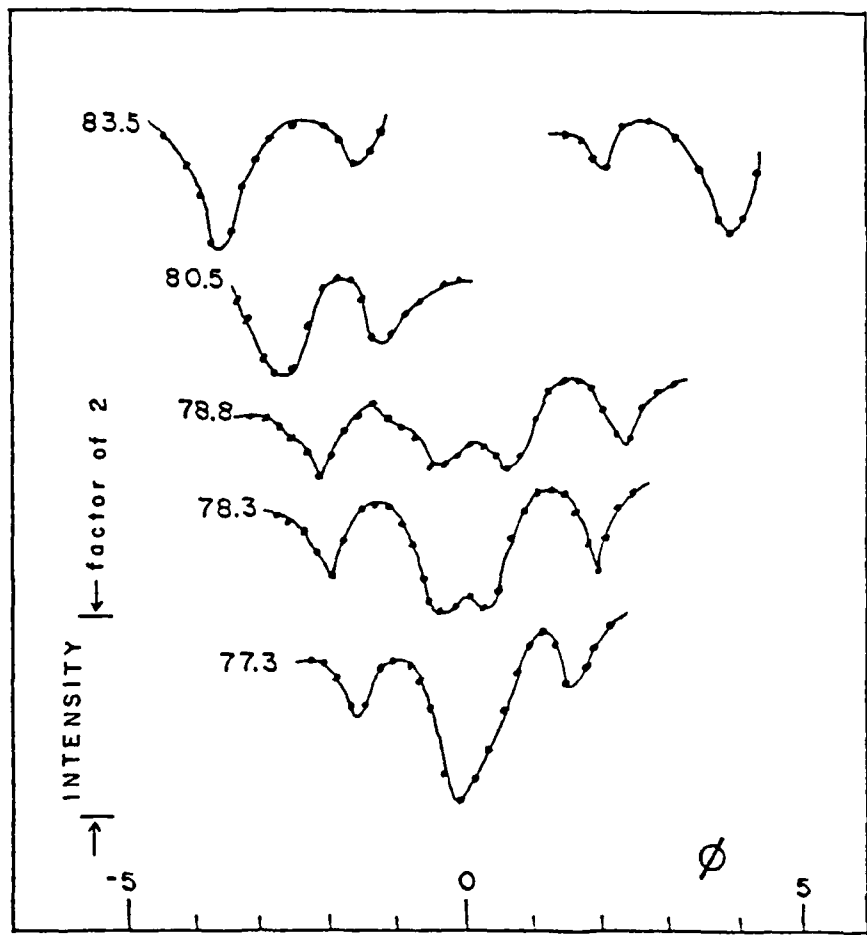


Figure 24c. Same as Figure 24a except corresponding to region "c" of Figure 25.

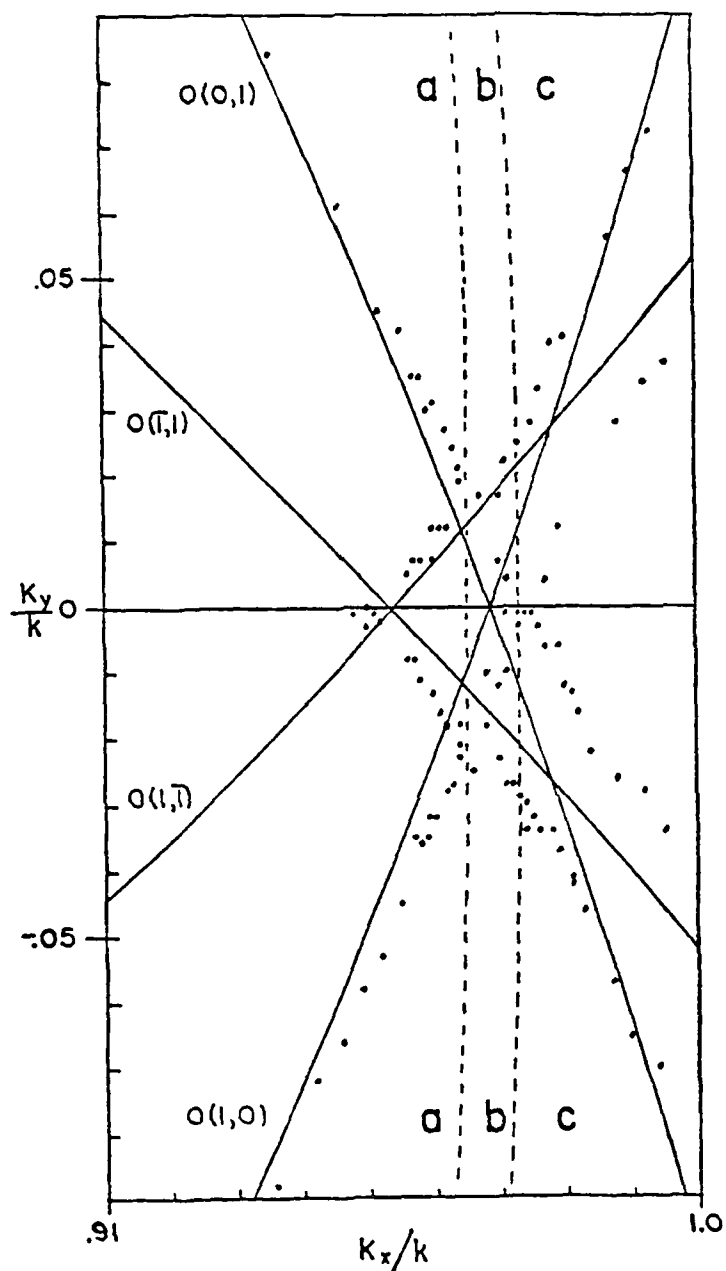


Figure 25. Resonance loci of data in Figure 24 plotted in normalized  $K_x$ - $K_y$  plane; points are measured data, lines are free particle curves [Equation (6)].

Figure 25, and similarly for b and c. At the lowest polar angle, in Figure 24a and region "a", only the pair of minima for the  $0(1,0)$  and  $0(0,1)$  states are visible. These are first-order transitions, i.e., coupled to the incident beam via first-order reciprocal lattice vectors, and therefore quite strong. As  $\theta$  increases, these minima move inward toward  $\phi = 0^\circ$ . As this happens, another minimum appears, much weaker, at  $\theta \approx 72.5^\circ$ . It then splits and moves outward, growing stronger and merging with the other pair at  $\theta \approx 75.5^\circ$ . As seen in Figure 25, the weak minima correspond to the second-order transitions  $0(1,\bar{1})$  and  $0(\bar{1},1)$ . The  $0(1,\bar{1})$  state is strongly coupled to  $0(1,0)$  by  $V_{01}(z)$ , and likewise,  $0(\bar{1},1)$  to  $0(0,1)$  by  $V_{\bar{1}0}(z)$ . Note that the strong coupling does not occur between the pairs of states that cross at  $\theta \approx 75.5^\circ$ ; thus, there is no observable splitting there.

Consider next Figure 24b and region "b" of Figure 25. Here, the merged minima split as  $\theta$  continues to increase, the first-order ones moving inward to their crossing at  $\theta \approx 77^\circ$  and the second-order ones moving outward. Finally, in Figure 24c and region "c" the strongly interacting pairs come together. In the region of strong interaction, they form two mixed states separated by a band gap. After the crossing point is passed, the levels start to approach the free-atom curves and the second-order ones fade away as the admixture becomes weaker.

This is evidently an example of the phenomenon predicted by Weare et al.<sup>15</sup> The second-order resonances, not normally observable, become manifest by "borrowing" intensity from the first-order states they are admixed with. From the magnitude of the splitting of  $0(1,0)$

and  $0(\bar{l},\bar{l})$ , the matrix element  $\langle 0|v_{0,1}|0\rangle$  is calculated to be  $0.25 \pm 0.03$  meV. These results are consistent with those of Boato et al.<sup>24</sup> (see also Table 11).

b. Using 4.7 meV incident beam.

The use of a very low-energy, long-wavelength incident beam has several desirable features. The constraints imposed by the kinematics of the scattering result in fewer open diffraction channels at these energies. The number of selective absorptions allowed also decreases and the resonances spread out in  $K_x - K_y$  space. Thus, the situation is somewhat simplified as compared to the 17.3 meV beam. An application of this low energy beam is presented here for helium scattering from graphite, namely a study of some splittings, which are also slightly more spread out in  $K_x - K_y$  space.

A situation similar to that just previously described is seen in Figures 26 and 27, this data taken with 4.7 meV incident energy corresponding to  $k_i \approx 3.0 \text{ \AA}^{-1}$ . The region being examined again includes both first- and second-order transitions, the first-orders being  $j = 1$  states this time. For the lowest values of  $\theta$ , the minimum at the higher  $\phi$  corresponds to the  $1(0,1)$  state, while the minimum at lower  $\phi$  corresponds to  $0(\bar{l},\bar{l})$ . As  $\theta$  increases, both resonances move inward toward their nominal crossing points at  $\theta = 0^\circ$ . At  $\theta \approx 52^\circ$ , the  $0(\bar{l},\bar{l})$  becomes degenerate at  $\phi = 0^\circ$  with the  $0(\bar{l},\bar{l})$  symmetrical to it (not shown in Figure 26 for simplicity). The  $1(0,1)$  resonance, however, is split off by its admixture with the  $0(\bar{l},\bar{l})$  and does not

$^4\text{He}$  ( $k = 3 \text{\AA}^{-1}$ ) / Graphite

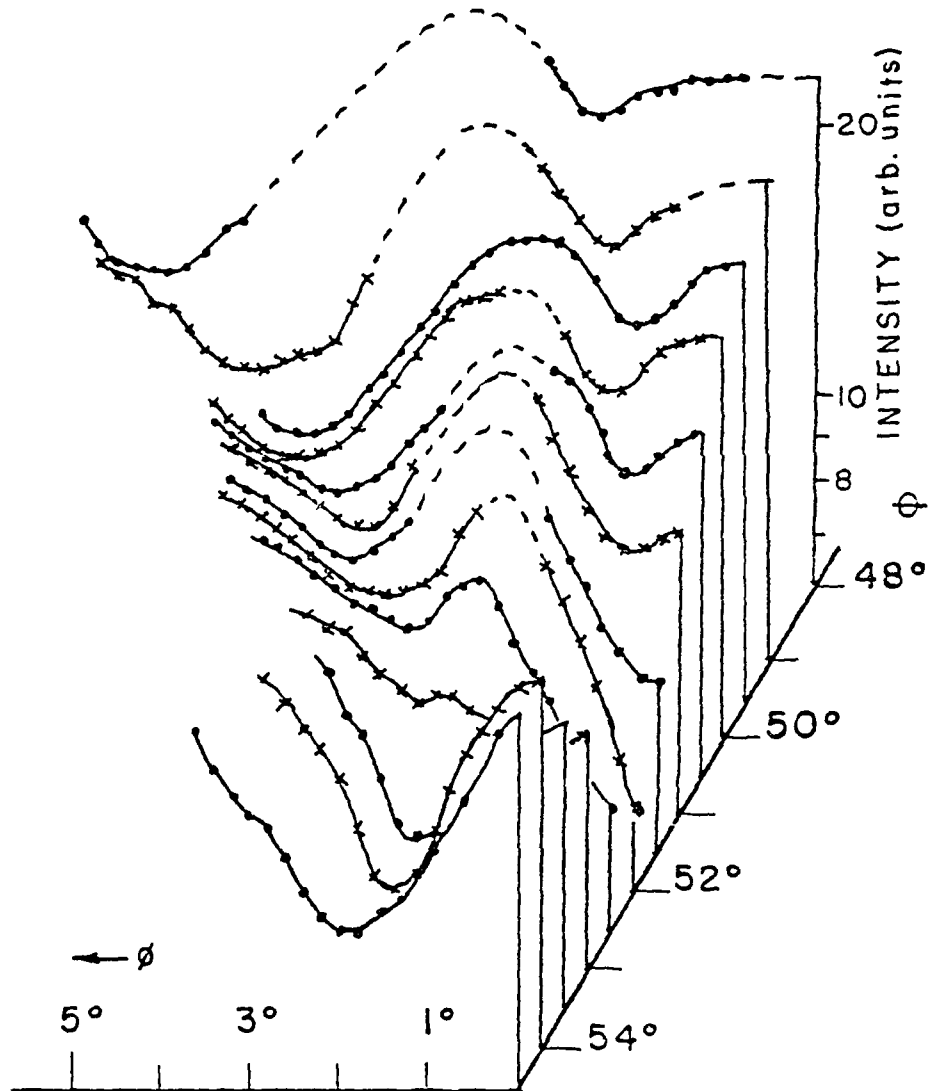


Figure 26. Specular intensity vs. azimuthal angle as in Figure 24 except incident energy is 4.7 meV.

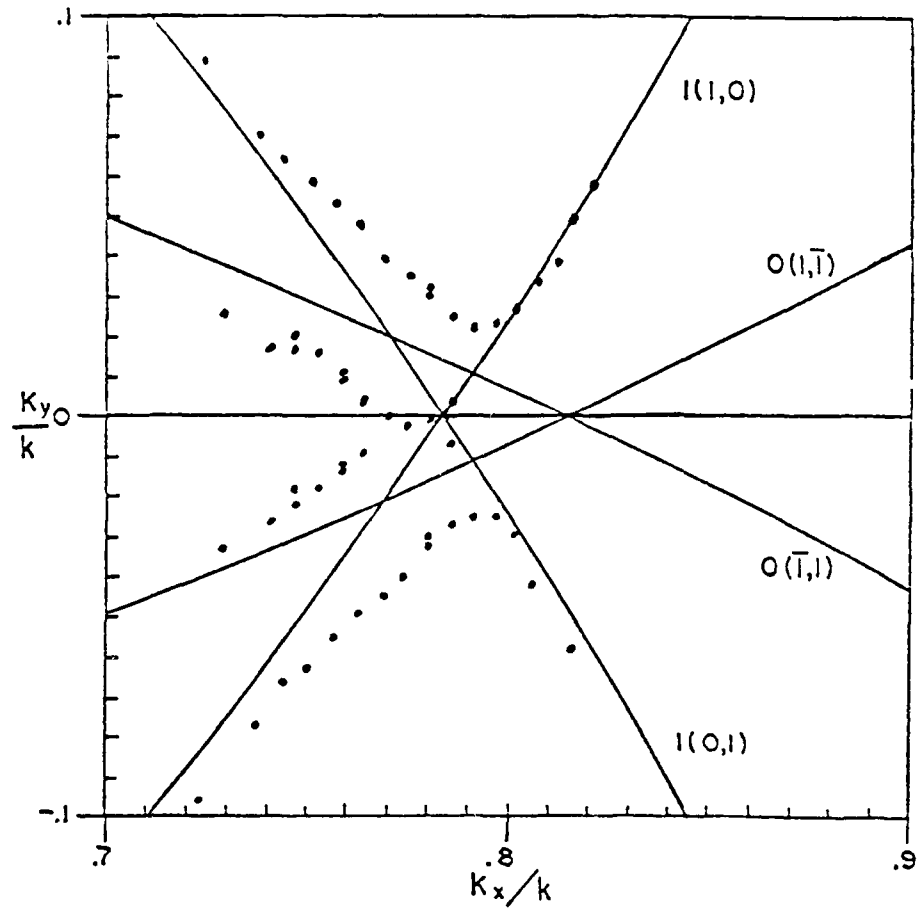


Figure 27. Resonance loci of data in Figure 26, plotted as in Figure 25.

become degenerate with the  $1(1,0)$ . Rather, it starts following the  $1(1,0)$  curve at  $\beta = 54^\circ$  and several degrees from zero in  $\beta$  (the symmetrical situation occurs at negative  $\beta$ ) as seen in Figure 27. The splitting is caused by strong coupling between the first-order and second-order states by  $V_{j,j'}$  terms, and the matrix element for this case can be calculated from the data. The results is  $|V_{j,j'}| = 0.22 \pm 0.03$  meV, again in agreement with the results of Boato et al.<sup>24</sup> that were obtained at a much higher incident energy than the present case. This is also another example of a weak second-order resonance becoming observable via its admixture with a first-order state. They become visible upon approaching the region of strong mixing, remain throughout this vicinity, and disappear as they become decoupled from the first-order transitions.

Figure 28 shows an extension of the data in Figure 27 to encompass a wider range in  $k_x$ - $k_y$  space. Included is a splitting caused by strong mixing of the  $0(1,1)$  and  $1(1,0)$  states, both of which are first-order. Also shown are crossings of these states with the  $2(\bar{1},0)$ ,  $3(\bar{1},0)$ , and  $4(\bar{1},0)$ . The latter three resonances are weakly coupled to the former two via higher-order Fourier components and thus are only weakly perturbed.

The splitting of the  $0(1,1)$  and the  $1(1,0)$  exhibits an interesting phenomenon. The mixed state on the left disappears. This reflects the form of a spatial fading out, as seen by examining the data for this splitting in Figure 29. It is also seen in the scattering from an infinite set of coherent operators,<sup>24</sup> which is appropriate if expected in

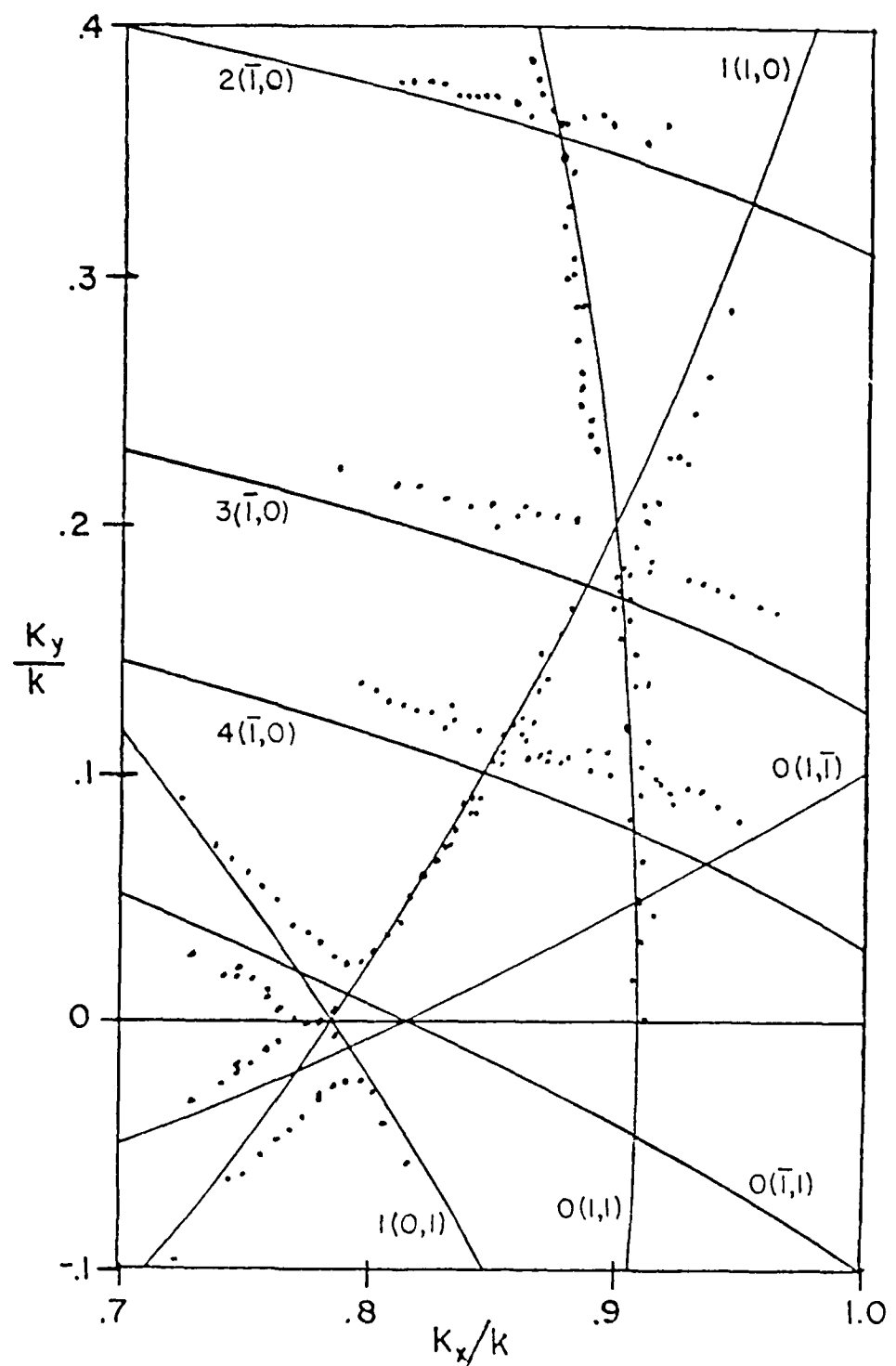


FIGURE 18. Resonance loci as in Figure 17 but over a larger area of the  $K_x$ - $K_y$  plane.

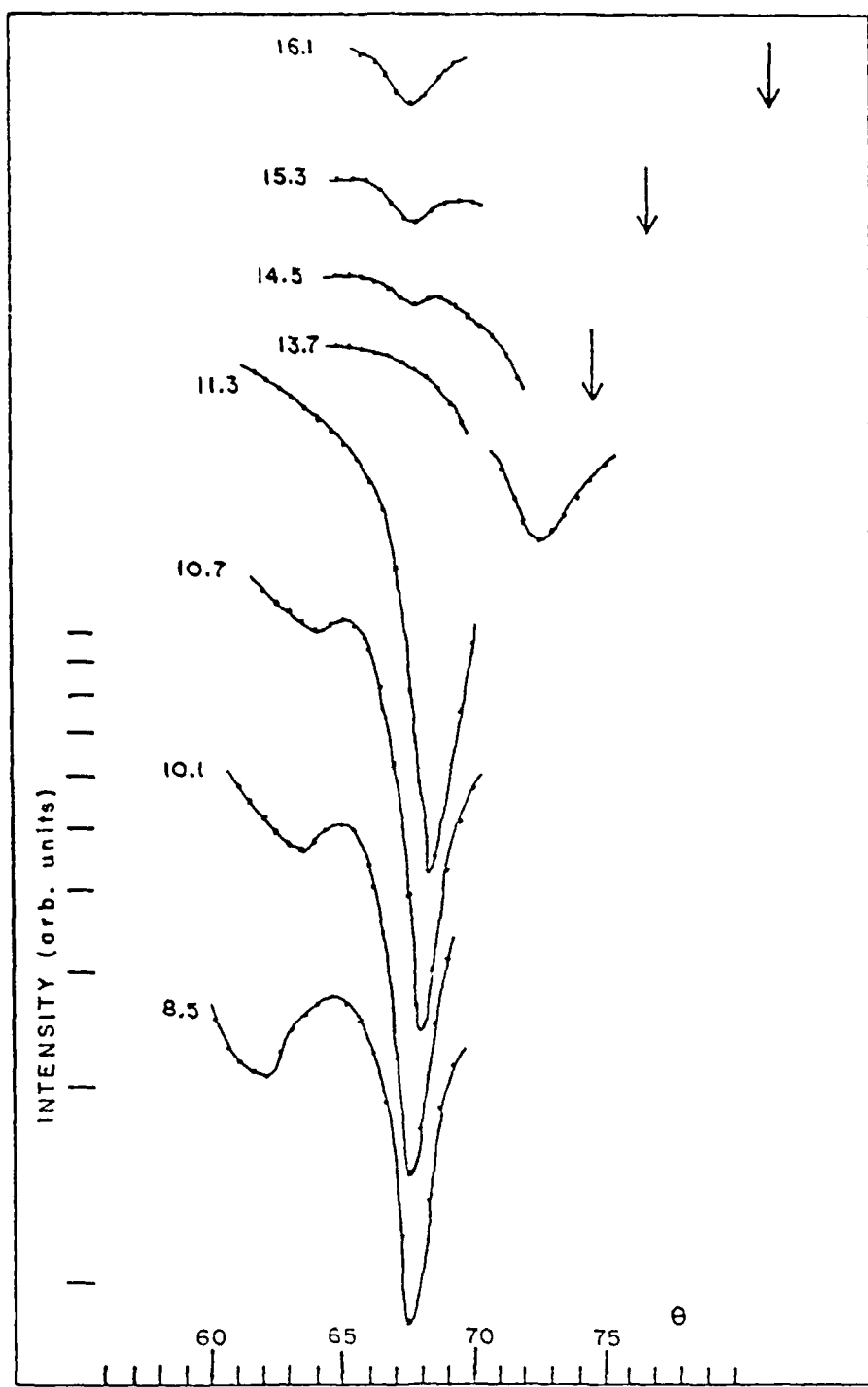


Figure 29. Specular intensity vs. polar angle for several azimuthal angles, showing the splitting depicted in Figure 18; arrows indicate positions of  $1(1,0)$  resonance for which scans were not taken.

situations of high symmetry,<sup>18</sup> but there is no obvious symmetry here. There is some evidence that it may be caused by inelastic effects.<sup>63</sup> At any rate, an estimate of the matrix element for the splitting can be calculated by extrapolating the observed data. It is found to be  $\langle 1|V_{0,1}|0\rangle = 0.16 \pm 0.03$  meV, which again agrees within experimental error with the result of Boato et al.<sup>24</sup> obtained at the higher beam energy.

The  $(\bar{1},0)$  states are only weakly coupled to the  $(1,0)$  and  $(1,1)$  states they cross. For  $j = 4$  and  $j = 2$ , they simply cross with no noticeable disturbance, as expected. The  $3(\bar{1},0)$  transition, however, crosses through the  $1(1,0)-0(1,1)$  splitting and it also disappears in this vicinity. Since the coupling in this case is weak, the situation is somewhat different than for the  $(1,0)-(1,1)$  mixture. Neither case is really well understood theoretically. Finally, notice that the average binding energies of the  $(\bar{1},0)$  resonances in this region are ~0.1 meV higher than the overall averages previously established. This is seen to be the case with the 17.3 meV beam energy also.

#### 4. Inelastic effects

Even at 17.3 meV incident energy, there is some evidence of the presence of inelastic processes operating in the scattering. The experimentally observed selective adsorption signatures are virtually all intensity minima, whereas the elastic scattering theories of Weare et al.<sup>15</sup> and Garcia et al.<sup>16</sup> predict maxima in a few cases. More compelling evidence can be adduced by use of the lower energy beam.

Figure 30 shows specular intensity data as a function of polar angle at  $\phi = 0^\circ$  for two different incident energies. Figure 30a is data for the beam energy at 16.8 meV, while Figure 30b is for the 5.1 meV beam energy. The data were taken on the same surface and incidence conditions other than experimental variables were held as constant as possible.

The major qualitative trends in the data can be explained within an elastic scattering framework. In Figure 30a the intensity in the specular beam shows an overall decreasing trend with  $\theta$ . This is probably caused by the intensity going into the diffraction channels which become open at lower  $\theta$ . When the beam energy is 5.1 meV, fewer diffraction channels open and this is reflected in the relatively flat (except resonances) intensity scan of Figure 30b. Since there are fewer open channels, however, it is expected that the specular intensity at 5.1 meV be greater than that at 16.8 meV for any polar angle. From Figure 30 it is seen that the intensities are about the same magnitude. This fact also contradicts the predictions of a Debye-Waller model. A highly probable explanation of this is the presence of inelastic scattering processes draining intensity from the specular beam.

In order to perform a more direct test of this hypothesis, the beam energy is further lowered to about 2.9 meV. At this incident energy, only one diffracted beam, the  $(\bar{l}, \bar{l})$  is allowed at  $\phi = 0^\circ$ , and it is an in-plane beam. Thus, it is possible to monitor the total diffracted flux from a well-defined crystal plane as the polar angle is scanned through a selective absorption resonance.

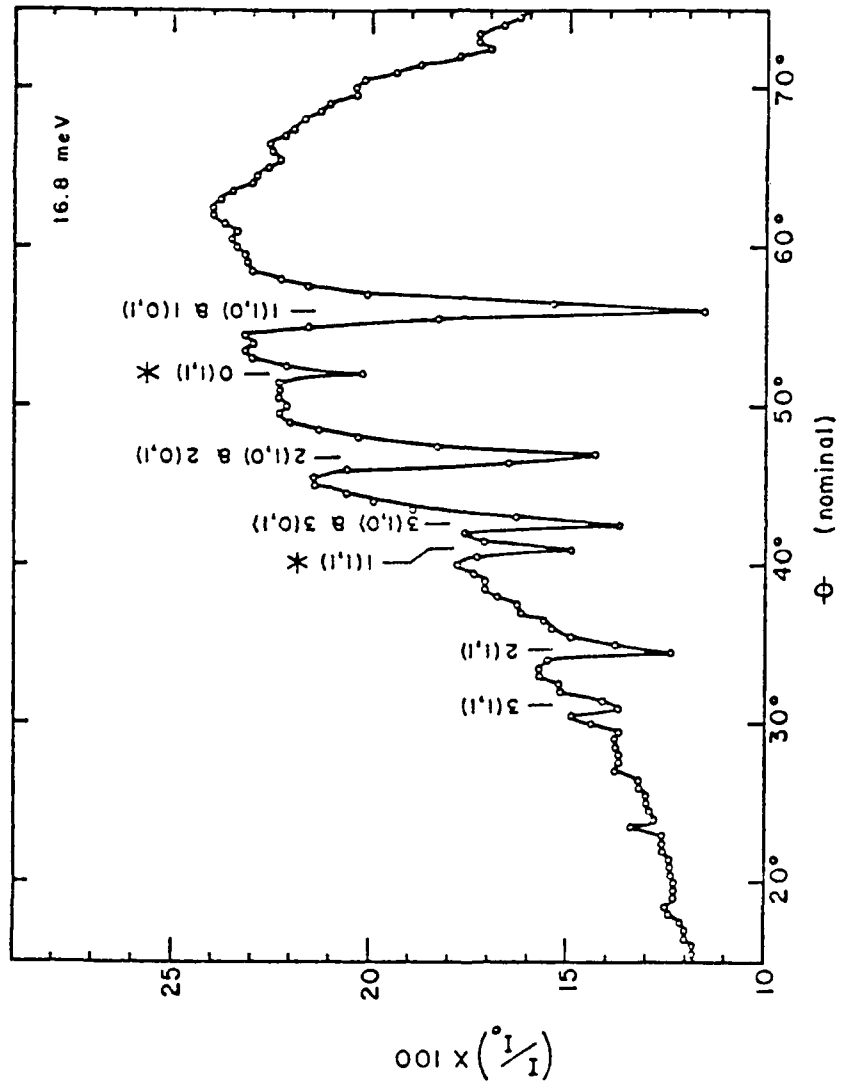


Figure 30a. Specular intensity vs. polar angle for  $\theta = 0$  at 16.8 meV incident beam energy; the (\*) indicate features predicted to be maxima (see text).

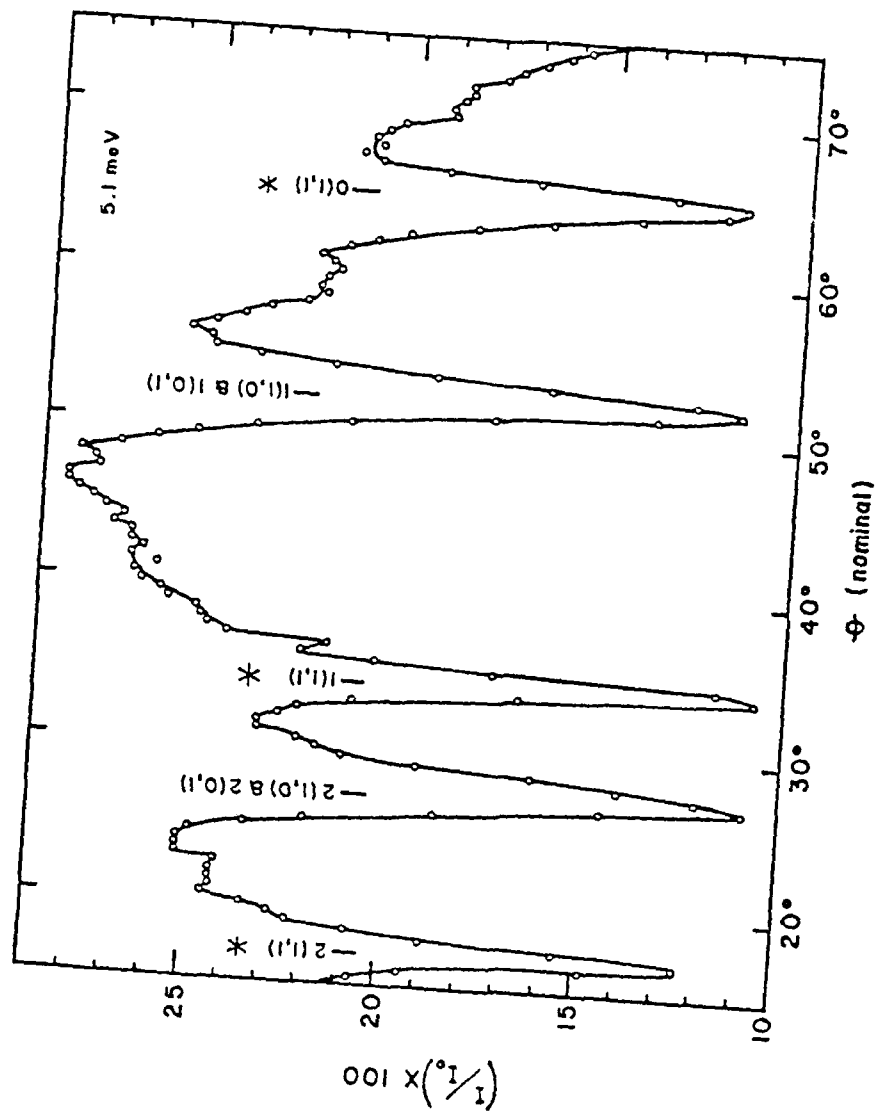


Figure 30b. Same as figure 30a except for a 5.1 meV beam energy.

Any unitary elastic theory predicts that an intensity minimum in one of the beams should give rise to a maximum in the other. Results for the  $1(1,0)-1(0,1)$  transition are presented in Figure 31, where it is seen that minima in both beams occur. It is felt that this is an unambiguous demonstration of the importance of inelastic scattering, and probably as well as can be done without energy analysis of the scattered beams.

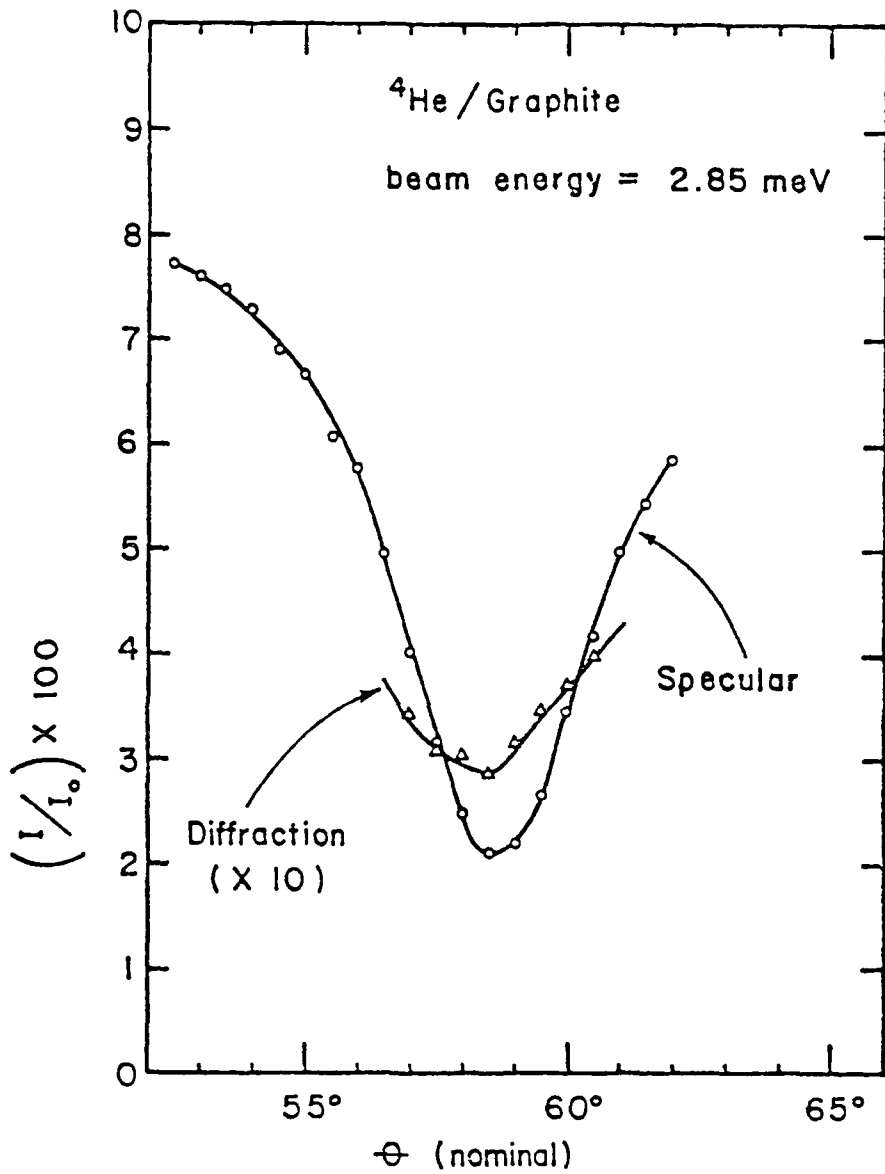


Figure 31. The measurement of total diffracted intensity; specular and diffraction intensities are plotted vs. polar angle.

## VI. DISCUSSION

### A. Alkali Halides

#### 1. Laterally averaged potentials

A major experimental result of Section V.A is the eigenvalue spectrum of helium adsorbed on NaF and LiF surfaces. These values are the input for the generation of semi-empirical potentials  $V_0(z)$ . Two isotopes of helium are used to increase the input available for these calculations. The eigenvalue data also would serve as a test of any first-principles calculation of  $V_0(z)$ , but this has not yet been done.

Several semi-empirical model potentials have been used with success by Cole et al.<sup>64</sup> Two of these, the 3-9 potential<sup>64,65</sup> and the shifted Morse hybrid potential,<sup>64</sup> have been fit to the alkali halide eigenvalue data and are discussed here. The 3-9 potential can be written

$$V(z) = \frac{3^{3/2} D_e}{2} e^{-\left[\left(\frac{C}{z+z_0}\right)^3 - \left(\frac{\sigma}{z+z_0}\right)^3\right]} , \quad (12)$$

where  $D_e$  is the well depth, and  $\sigma$  is the distance for which the potential is equal to zero ( $z_0$  simply shifts the  $z$ -axis without changing the eigenvalue spectrum). The values of the parameters are summarized in Table 6, and the calculated eigenvalues are compared to experiment in Table 7. Equation (12) has the correct asymptotic form of  $\frac{1}{z}$ , far from the surface,<sup>66</sup> and the coefficient  $C_3$  of the asymptotic  $\frac{1}{z^3}$  can be calculated from  $D_e$  and  $\sigma$ . The  $C_3$  calculated in this way, however, is about twice the theoretical value of Bruch and Watanabe.<sup>67</sup> This discrepancy is probably due to the fact that the data is representative

Table 6A. Parameters of the 3-9 potential (from Ref. 64).

System	$D_e$ (meV)	$\sigma$ (Å)	$C_3$ (meV Å <sup>3</sup> )	$z_0$ (Å)	$r_D$
He/NaF	7.64	1.91	138.3	0.59	3.58
He/LiF	8.92	1.94	169.2	0.70	3.93

Table 6B. Parameters of the shifted Morse hybrid potential (from Ref. 64).

System	$D$ (meV)	$\sigma^{-1}$ (Å <sup>-1</sup> )	$\Delta$	$z_p$ (Å)	$z_e$ (Å)	$D(1 + \Delta)$ (meV)	$C_j^a$ meV·Å <sup>3</sup>
He/NaF	6.5176	1.2269	0.05937	4.263	1.699	6.905	72.5
He/LiF	7.740	1.2929	0.075	3.482	1.634	8.321	81.7

<sup>a</sup>Theoretical value, from Reference 67

Table 7. Comparison of experimental and calculated eigenvalues.

System	j	$ \tilde{E}_j $ (expt.) (meV)	$ E_j $ (3-9) <sup>a</sup> (meV)	$ E_j $ (SMH) <sup>a</sup> (meV)
<sup>3</sup> He/NaF	0	4.50	4.53	4.558
	1	1.38	1.40	1.380
	2	--	0.33	0.245
	3	--	0.05	0.018
<sup>4</sup> He/NaF	0	4.92	4.89	4.838
	1	1.87	1.82	1.883
	2	0.54	0.56	0.471
	3	--	0.13	0.071
<sup>3</sup> He/LiF	0	5.59	5.56	5.616
	1	2.00	1.94	1.945
	2	--	0.54	0.412
	3	--	0.11	0.045
<sup>4</sup> He/LiF	0	5.90	5.94	5.940
	1	2.46	2.44	2.487
	2	0.78	0.86	0.731
	3	0.21	0.24	0.141
	4	--	0.05	0.014

<sup>a</sup>From Reference 64

of atoms localized near the surface rather than in the asymptotic region. A convenient property of Equation (12) is that it predicts, to very good approximation, an analytic eigenvalue spectrum.<sup>65</sup>

$$\eta = \eta_D - a C_3^{1/3} |E_j|^{1/6} , \quad (13)$$

where  $\eta$  is a mass reduced quantum number allowing utilization of data for both isotopic forms and is defined by  $\eta \equiv (j + \frac{1}{2})/m^{1/2}$ .

The shifted Morse hybrid potential is based on the idea that the Morse potential is a good approximation to  $V_0(z)$  near the minimum but has the incorrect asymptotic form. Thus, for  $z$  greater than some point  $z_p$ , the form  $\frac{C_3}{z^3}$  is assumed with  $C_3$  being the theoretical value. For  $z$  less than  $z_p$ , a shifted Morse function

$$V_{SM}(z) = D(x^2 - 2x - \Delta), \quad x = e^{-a(z-z_e)} \quad (14)$$

is used, where  $D$  is the well depth,  $\Delta$  is the shift, and  $z_e$  is the equilibrium position. The parameters of Equation (14) are fitted to the energy eigenvalues and the functions are matched at  $z_p$ . Tables 6 and 7 give the parameters and predicted eigenvalues of the shifted Morse hybrid potential for helium on the alkali halides. A plot of these potentials is given in Figure 32 for helium on NaF.

## 2. Surface periodicity

The matrix elements measured for He on LiF can be compared to theoretical calculations done by Tsuchida<sup>66</sup> and by Chow and Thompson.<sup>17</sup> The method they employ is to model the potential as a sum of pair

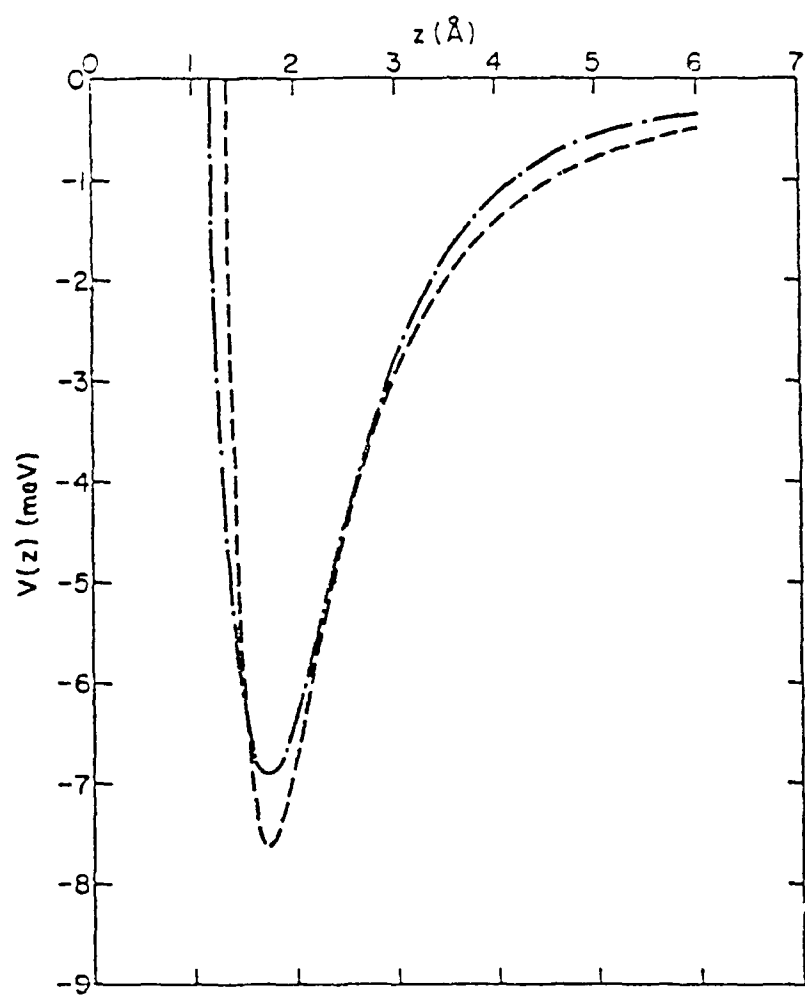


Figure 32. Plot of the 3-9 potential (---) and the shifted Morse hybrid potential (-·-) for He/NaF (from Ref. 64).

AD-A082 986 PENNSYLVANIA STATE UNIV UNIVERSITY PARK APPLIED RESE--ETC F/8 7/4  
SCATTERING OF LOW ENERGY HELIUM BEAMS FROM CLEAN SURFACES OF SO--ETC(U)  
DEC 79 6 N DERRY N00024-79-C-6043  
UNCLASSIFIED ARL/PSU/TM-79-220 NL

2 OF 2  
AD-A082 986

END  
DATE  
ESTIMED  
5-80  
OTIC

Table 8. Experimental and theoretical values of  $^4\text{He}/\text{LiF}$  matrix elements (in meV).

	Chow and Thompson <sup>a</sup>	Tsuchida <sup>b</sup>	Experimental
$\langle 0   v_{01}   0 \rangle$	0.32	0.43	$0.25 \pm 0.05$
$\langle 1   v_{01}   1 \rangle$	0.14	0.20	$0.20 \pm 0.10$
$\langle 0   v_{11}   0 \rangle$	0.21	0.28	$0.10 \pm 0.05$
$\langle 1   v_{11}   1 \rangle$	0.09	0.14	<0.05

<sup>a</sup>From Reference 17

<sup>b</sup>From Reference 68

interactions between the He atom and the ions of the crystal, and they compute the Fourier expansions of the resulting expressions. From the one-dimensional Schroedinger equation using  $V_0(z)$ , the wave functions are calculated. The theoretical matrix elements are then found by numerical integration. Tsuchida represented the potential as a sum of 12-6 pair interactions, while Chow and Thompson used sums of Yukawa - 6 pair potentials. The results of their calculations, along with the experimental values for comparison, are presented in Table 8.

Notice that the theoretical models overestimate the strength of  $V_{11}$  as compared with  $V_{01}$ . Carlos has pointed out<sup>29</sup> that this may be due in part to the approximations made in the pair potentials. In particular, the He-Li<sup>+</sup> pair interaction is approximated by that for He-He, and He-F interaction is approximated by that for He-Ne. This is consistent with the He/LiF diffraction data, which can be interpreted quite well using only the (0,1) component of a surface corrugation function.

### B. Graphite

#### 1. Application to physisorption

As in the case of the alkali halides, the eigenvalues  $E_j$  constitute the spectroscopic data of the adatom states. Carlos and Cole<sup>29,69,70</sup> have fit several model potentials to data for both isotopes. These include pairwise sums of 12-6 potentials, 12-8-6 potentials, exponential - 6 potentials, and Yukawa - 6 potentials. In all cases, they find that the  $E_j$  can be fit to these potentials, but the matrix elements measured for He on graphite by Boato et al.<sup>24</sup> cannot be accounted for. This

situation is remedied by the introduction of anisotropy into the potential corresponding to the anisotropy of the bonding orbitals in the graphite basal plane. They sum over pair potentials of the form

$$U(\vec{r}) = \frac{A e^{-\alpha r}}{r} (1 + \gamma_R \cos^2 \theta) - \frac{3a_s d C_3}{\pi r^6} \left[ 1 - \gamma_A \left( 1 - \frac{3}{2} \cos^2 \theta \right) \right] , \quad (15)$$

and obtain a laterally averaged potential

$$V_0(z) = \frac{4\pi A}{3a_s} \left[ e^{-\alpha z} + \gamma_R \alpha z E_2(\alpha z) \right] - 3C_3 d \sum_{n=0}^{\infty} (z+nd)^{-4} , \quad (16)$$

where  $a_s$  is the unit cell area,  $d$  is the interplanar spacing, and  $E_2(\alpha z)$  is an exponential integral. The parameters of  $V_0(z)$  are fit to the eigenvalues tabulated in Section V.B. The pairwise sums also yield the higher-order  $V_G(z)$ , which are fit to the matrix elements. The parameters of the modified Yukawa - 6 potential are listed in Table 9, while the eigenvalues and matrix elements calculated from it are compared to experimental values in Tables 10 and 11. The agreement is very good, and this is thought to be a good approximation to the helium-graphite interaction. On the other hand, the optimum value of  $C_3$ , given in Table 9, is about half the theoretical value.<sup>71</sup> This is probably because the atoms in resonance do not sample much of the asymptotic region. A plot of the potential over various lattice sites is shown in Figure 33.

A further test of both experiment and theory is to compare these results with the data from experiments on thermodynamic properties of He films adsorbed on graphite. Before this can be done, however, the

Table 9. Parameters of modified Yukawa-6 potential, from Reference 69

$\gamma_A^a$	$\gamma_R$	$\alpha$	$C_3$	$A$
0.4	-0.29	3.25 $\text{\AA}^{-1}$	83 meV- $\text{\AA}^3$	47.2 eV

<sup>a</sup>Fixed a priori from dielectric properties of graphite

Table 10. Experimental and theoretical energy eigenvalues of He/graphite (in meV).

n	<sup>4</sup> He/graphite		<sup>3</sup> He/graphite	
	Experimental	Theoretical <sup>a</sup>	Experimental	Theoretical <sup>a</sup>
0	-12.06	-12.12	-11.62	-11.61
1	- 6.36	- 6.36	- 5.36	- 5.34
2	- 2.85	- 2.77	- 1.78	- 1.88
3	- 1.01	- 0.94	--	- 0.44
4	- 0.17	- 0.22	--	--

<sup>a</sup>From Reference 69

Table 11. Theoretical and experimental matrix elements for He/graphite (in meV).

	Theoretical <sup>a</sup>	Experimental	
		Boato et al. <sup>b</sup>	Penn State
$\langle 0   v_{01}   0 \rangle$	-0.27	-0.28	-0.25
$\langle 1   v_{01}   1 \rangle$	-0.21	-0.185	
$\langle 2   v_{01}   2 \rangle$	-0.13	-0.12	
$\langle 3   v_{01}   3 \rangle$	-0.06	-0.08	
$\langle 0   v_{01}   1 \rangle$	0.20	0.195	0.19 <sup>c</sup>
$\langle 0   v_{01}   2 \rangle$	0.13	0.125	
$\langle 0   v_{01}   3 \rangle$	0.08	0.09	
$\langle 0   v_{01}   4 \rangle$	0.04	0.03	
$\langle 1   v_{01}   2 \rangle$	0.16	0.16	
$\langle 1   v_{01}   2 \rangle$	0.10	0.10	
$\langle 2   v_{01}   3 \rangle$	0.09	0.11	

<sup>a</sup> From Reference 69

<sup>b</sup> From Reference 24

<sup>c</sup> Average value

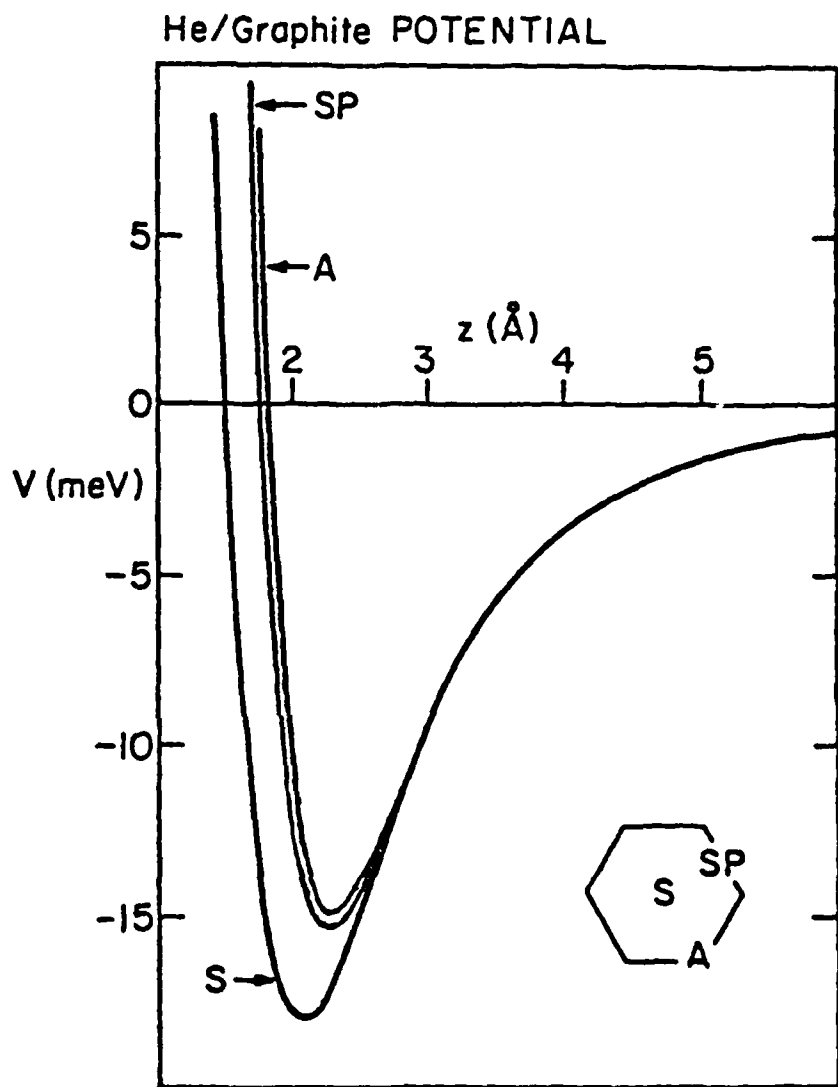


Figure 33. Plot of modified Yukawa-6 potential (summed) for He, graphite over principal lattice sites (from Ref. 69).

free-atom binding energies  $E_j$  must be modified to account for band-structure. A full band-structure calculation was done by Carlos and Cole,<sup>29,70</sup> using the data of the Genoa group<sup>24</sup> and of Section V.B. The result of their calculation at scattering energies demonstrates the validity of the free-atom approximation used to obtain the  $E_j$  (far from level crossings). Their calculation in the energy regime of physisorbed sub-monolayer He films shows a greater degree of corrugation than was previously believed,<sup>72</sup> implying somewhat less free-particle character for the adatoms. This result reflects the anisotropy of the potential.

The computed band-structure corrections at  $\bar{K} = 0$  are - 0.16 meV for <sup>4</sup>He, and - 0.11 meV for <sup>3</sup>He. This yields  $E_j = -12.22$  meV for <sup>4</sup>He, and  $E_j = -11.73$  meV for <sup>3</sup>He as the ground state energy of a single atom adsorbed on graphite. The ground state energy per atom in an adsorbed film is equal to the chemical potential  $\mu_0$  at  $T = 0$ K. This quantity has been derived from thermodynamic data by Greif et al.<sup>73</sup> for <sup>3</sup>He and <sup>4</sup>He films on graphite. After correction is made for the latent heat of <sup>4</sup>He<sup>74</sup> (<sup>3</sup>He is not expected to condense<sup>75</sup>), they obtain  $\mu_0 = -12.27 \pm 0.2$  meV for <sup>4</sup>He, and  $\mu_0 = -11.72 \pm 0.2$  meV for <sup>3</sup>He. These values are in excellent agreement, which seems significant considering the vast differences between the two types of experiment.

## 2. Evaluation of scattering theory

It is clear from the previous treatment that the kinematical analysis has a firm foundation. Results of dynamical scattering

theory, however, are still subject to doubt. Considering the success of elastic theories in predicting resonance lineshapes for He scattering from LiF and their partial success for graphite, it seems that inelastic processes may be the cause of discrepancies.

A major success of elastic theory is the prediction by Weare et al.<sup>15</sup> of intensity borrowing in level crossing. The data of Section V.B demonstrate that this prediction is quite consistent with experiment for both moderate and very low beam energies. The same theory, however, predicts selective adsorption intensity maxima which are observed experimentally to be minima. The conjecture that this is caused by inelastic scattering is consistent with the large increase in signal produced by lowering the surface temperature. This is intuitively sensible since weak interlayer forces in graphite can be expected to produce soft vibrational modes.

The data also show a resonance disappearing in the vicinity of a level crossing, a phenomenon that occurs at both moderate and low beam energies. This is also unexplained by otherwise successful theories. Weare has reproduced this theoretically<sup>63</sup> by using an optical potential to incorporate inelastic effects into the scattering formalism. Chow<sup>55</sup> has also used the optical potential to show that elastic intensity maxima are transformed into minima. The optical potentials, unfortunately, provide virtually no detail about the atom-surface interaction.

Finally, the data taken with a very low energy incident beam show clear and direct violations of any unitary elastic theory. Thus,

despite its valuable successes, atomic beam scattering theory must directly confront the problem of inelastic scattering mechanisms in order to progress much farther. At the very least, it should be able to predict the conditions for which an elastic framework is appropriate.

### C. Conclusions

The major results of this work are the measurement of binding energies of  $^3\text{He}$  and  $^4\text{He}$  on NaF, LiF and graphite, the measurement of several matrix elements of  $^4\text{He}$  on LiF and graphite, and the examination of resonance lineshapes for  $^4\text{He}$  scattering from LiF and graphite, the latter at several incident beam energies. These results have several interesting implications for both atomic beam scattering theory and the physics of two-dimensional systems. In general, it seems that an elastic framework is more appropriate for He scattering from alkali halide surfaces than from the basal plane of graphite. Scattering studies on graphite, especially at very low incident energies, demonstrate the presence of important inelastic processes. Other experiments, however, exhibit phenomena at both moderate and very low beam energies that are consistent with an elastic formalism, such as intensity borrowing. The problem of determining the conditions under which an elastic framework is appropriate remains to be solved. The data presented here indicate the usefulness of the kinematical approach regardless of the status of dynamical theory. Within a kinematical framework, moreover, the free-atom approximation is seen to be good far from level crossings.

The free-atom approximation is used herein to calculate the binding energies of  $^4\text{He}$  and  $^3\text{He}$  on NaF, LiF, and graphite. From these, a set of laterally averaged potentials  $V_0(z)$  are generated for these systems.  $V_0(z)$  is well-characterized for helium on both alkali halides and graphite. There are still problems, however, with these models. In particular, the coefficient of the potential's asymptotic tail differs greatly from theory in all these cases.

Matrix elements of the  $V_G(z)$  were also measured for  $^4\text{He}$  on LiF at 17.3 meV and  $^4\text{He}$  on graphite at 4.7 meV. The LiF measurements indicate that the  $V_{01}$  component dominates the surface periodicity. In the case of graphite, the matrix elements measured at 4.7 meV beam energy agree within error with those of Boato et al.<sup>24</sup> measured at a higher energy. The latter were employed by Carlos and Cole,<sup>69</sup> along with the  $^4\text{He}$  and  $^3\text{He}$  eigenvalues, to generate the form of the helium-graphite potential. It is found that an anisotropic form is required. They then use the potential to calculate the band-structure of helium on graphite.

The major conclusion of these calculations, based partly on the data presented herein, is that the adsorbed He atoms feel a larger corrugation than was previously thought to exist. This has obvious implications for the thermodynamics of helium films on graphite. For the comparison which has been made already, the scattering data and thermodynamic data are in remarkable agreement for the ground state energy of both  $^4\text{He}$  and  $^3\text{He}$  on graphite. Efforts are continuing<sup>70</sup> in the calculation of thermodynamic properties from scattering results on this system.

#### D. Suggestions for Future Work

In view of the important role played by inelastic scattering mechanisms, a high priority should be given to energy analysis of the scattered beams. This can be done by the time-of-flight technique. It will provide important information about the surface vibrational modes, and will probably contribute to the understanding of the scattering mechanisms as well.

Experiments should be done on a variety of other surfaces. Semiconductors, metals, diamond, and secondary cleavage planes of the alkali halides are a few of the possibilities. Another interesting and valuable experiment would be scattering of helium from adsorbed overlayers of the heavy rare gases. Rare-gas-plated graphite basal planes are a particularly interesting possibility.

## REFERENCES

1. I. Estermann and O. Stern, Z. Phys. 61, 95 (1930).  
I. Estermann, R. Frisch, and O. Stern, Z. Phys. 73, 348 (1932).  
R. Frisch and O. Stern, Z. Phys. 84, 430 (1933).
2. J. E. Lennard-Jones and A. F. Devonshire, Nature 137, 1069 (1936).
3. J. C. Crews, J. Chem. Phys. 37, 2004 (1962).
4. J. R. Bledsoe and S. Fisher, Surf. Sci. 46, 129 (1974).
5. D. R. O'Keefe, J. N. Smith, R. L. Palmer, and K. Saltsburg, J. Chem. Phys. 52, 4447 (1970).
6. A. Kantrowitz and J. Grey, Rev. Sci. Instr. 22, 328 (1951).
7. B. Wood, B. F. Mason, and B. R. Williams, J. Chem. Phys. 61, 1435 (1974).
8. G. Boato, P. Cantini, and L. Mattera, Surf. Sci. 55, 141 (1976).
9. H. Hoinkes, H. Nahr, and H. Wilsch, Surf. Sci. 30, 363 (1972).  
H. U. Finzel, H. Frank, H. Hoinkes, M. Luschka, H. Nahr, H. Wilsch, and U. Wonka, Surf. Sci. 49, 577 (1975).
10. D. E. Houston and D. R. Frankl, Phys. Rev. Lett. 31, 298 (1973).  
J. A. Meyers and D. R. Frankl, Surf. Sci. 51, 61 (1975).
11. N. Cabrera, V. Celli, F. O. Goodman, and R. Manson, Surf. Sci. 19, 57 (1970).
12. G. Wolken, Jr., J. Chem. Phys. 58, 3047 (1973).
13. H. Chow and E. D. Thompson, Surf. Sci. 54, 269 (1976).
14. M. W. Cole and D. R. Frankl, Surf. Sci. 70, 585 (1978).
15. C. E. Harvie and J. H. Weare, Phys. Rev. Lett. 40, 187 (1978).  
K. L. Wolfe and J. H. Weare, Phys. Rev. Lett. 41, 715 (1978).
16. N. Garcia, W. Carlos, M. Cole, and V. Celli, Phys. Rev., to be published.  
V. Celli, N. Garcia, and J. Hutchison, to be published.
17. H. Chow and E. D. Thompson, Surf. Sci. 59, 225 (1976).
18. H. Chow, Surf. Sci. 62, 487 (1977).

19. W. E. Carlos, G. Derry, and D. R. Frankl, Phys. Rev. B19, 3258 (1979).
20. M. J. Cardillo and G. E. Becker, Phys. Rev. Lett. 40, 1148 (1978).  
M. J. Cardillo and G. E. Becker, Phys. Rev. Lett. 42, 508 (1979).
21. J. M. Horne and D. R. Miller, Surf. Sci. 66, 365 (1977).
22. K. H. Rieder and T. Engel, Phys. Rev. Lett. 43, 373 (1979).
23. P. Cantini, R. Tatarek, and G. P. Felcher, Phys. Rev. B19, 1161 (1979).
24. G. Boato, P. Cantini, C. Guidi, R. Tatarek, and G. P. Felcher, Phys. Rev. B, to be published; see also Refs. 58 and 59.
25. E. Ghio, L. Mattera, C. Salvo, F. Tommasini, and U. Valbusa, to be published.  
L. Mattera, F. Rosatelli, C. Salvo, F. Tommasini, U. Valbusa, and G. Vidali, to be published.
26. G. Derry, D. Wesner, W. Carlos, and D. R. Frankl, Surf. Sci. 87, 629 (1979).
27. See, for example, W. A. Steele, The Interaction of Gases With Solid Surfaces, Pergamon Press (1974), p. 285.
28. See, for example, J. M. Ziman, Principles of the Theory of Solids, Cambridge University Press (1972), p. 79.
29. W. E. Carlos, Ph.D. Thesis, The Pennsylvania State University (1979), unpublished; see also Ref. 70.
30. F. O. Goodman, CRC Critical Rev. Solid State Mater. Sci. 7, 33 (1977).
31. D. E. Houston, Ph.D. Thesis, The Pennsylvania State University (1973), unpublished.
32. J. A. Meyers, Ph.D. Thesis, The Pennsylvania State University (1975), unpublished.
33. T. O'Gorman, Masters Thesis, The Pennsylvania State University (1979), unpublished.
34. D. R. Frankl, Rev. Sci. Instr. 45, 1375 (1974).
35. A. Landfors, private communication.
36. Spectra-mat, Inc., Watsonville, CA, USA.

37. Perkin-Elmer Ultek, Inc., Palo Alto, CA, USA.
38. Gast Mfg. Corp., Benton Harbor, MI, USA.
39. Crawford Fitting Co., Solon, OH, USA.
40. J. P. Toennies and K. Winkelmann, J. Chem. Phys. 66, 3965 (1977).
41. Air Products and Chemicals, Inc., Allentown, PA, USA.
42. J. G. Skofronick and W. M. Pope, Rev. Sci. Instr. 44, 76 (1973).
43. Physical Electronics Industries, Inc., Eden Prairie, MN, USA.
44. M. P. Liva, Masters Thesis, The Pennsylvania State University (1976), unpublished.
45. M. P. Liva and D. R. Frankl, Surf. Sci. 59, 643 (1976).
46. G. Derry, D. Wesner, S. V. Krishnaswamy, and D. R. Frankl, Surf. Sci. 74, 245 (1978).
47. M. P. Liva, G. Derry, and D. R. Frankl, Phys. Rev. Lett. 37, 1413 (1976).
48. D. R. Frankl, D. Wesner, S. V. Krishnaswamy, G. Derry, and T. O'Gorman, Phys. Rev. Lett. 41, 60 (1978).
49. S. V. Krishnaswamy, G. Derry, D. Wesner, T. J. O'Gorman, and D. R. Frankl, Surf. Sci. 77, 493 (1978).
50. Harshaw Chemical Co., Cleveland, OH, USA.
51. See, for example, Reference 28, p. 62.
52. J. L. Beeby, J. Phys. C (Solid State Phys.) 4, 301 (1971).
53. F. O. Goodman, Surf. Sci. 65, 37 (1977).
54. J. G. Dash, Physics Reports 38C, 177 (1978), and references therein.
55. H. Chow, Surf. Sci. 79, 157 (1979).
56. P. L. Walker, private communication.
57. A few examples are: J. A. Venables, H. M. Kramer, and G. L. Price, Surf. Sci. 55, 373 (1976); 57, 782 (1976) (THEED studies); J. J. Lander and J. Morrison, Surf. Sci. 6, 1 (1967); J. Suzanne, J. P. Coulomb, and M. Bienfait, Surf. Sci. 40, 414 (1973); 44, 141 (1974); 47, 204 (1975) (LEED studies); and K. Carneiro, W. D. Ellenson, L. Passell, J. P. McTague, and H. Taub, Phys. Rev. Lett. 37, 1965 (1976) (neutron diffraction).

58. G. Boato, P. Cantini, and R. Tatarek, Phys. Rev. Lett. 40, 887 (1978).
59. G. Boato, P. Cantini, R. Tatarek, and G. P. Felcher, Surf. Sci. 80, 518 (1979).
60. Union Carbide Corporation, Cleveland, OH, USA.
61. Space Environment Laboratories, Boulder, CO, USA.
62. The correlation coefficient used is
$$r = \left[ \frac{\sum (\theta' - \bar{\theta}') (\theta_d - \bar{\theta}_d)}{\sum (\theta' - \bar{\theta}')^2 \sum (\theta_d - \bar{\theta}_d)^2} \right]^{\frac{1}{2}}$$
63. J. H. Weare, private communication.
64. C. Schwartz, M. W. Cole, and J. Pliva, Surf. Sci. 75, 1 (1978).
65. M. W. Cole and T. T. Tsong, Surf. Sci. 69, 325 (1977).
66. E. M. Lifshitz, J. Exp. Theoret. Phys., USSR 29, 94 (1955).
67. L. W. Bruch and H. Watanabe, Surf. Sci. 65, 619 (1977).
68. A. Tsuchida, Surf. Sci. 46, 611 (1974).
69. W. E. Carlos and M. W. Cole, Phys. Rev. Lett. 43, 697 (1979).
70. W. E. Carlos and M. W. Cole, Phys. Rev. B, submitted for publication.
71. G. Vidali, M. W. Cole, and C. Schwartz, Surf. Sci. 87, L273 (1979).
72. D. E. Hagen, A. D. Novaco, and F. J. Milford, in Adsorption-Desorption Phenomena, edited by F. Ricca, Academic Press (1972), p. 99.
73. R. L. Elgin, J. M. Grief, and D. L. Goodstein, Phys. Rev. Lett. 41, 1723 (1978).
74. C. E. Campbell and M. Schick, Phys. Rev. A3, 691 (1971).
75. A. D. Novaco and C. E. Campbell, Phys. Rev. B11, 2525 (1975).

## APPENDIX

## Misalignment and Angular Measurement

A1. Introduction

The determination of the incidence angles,  $\theta$  and  $\phi$ , is a difficult procedure if high accuracy is required. One problem is caused by the crystal surface being composed of facets misaligned in polar angle. Another problem is caused by the apparatus misalignments outlined in Section IV.C; namely, the beam, the surface, and all rotation axes not being properly positioned with respect to each other. The two problems are not independent of each other, and the occurrence of both together is extremely difficult to treat. Because the facetting is not very bad in the alkali halides, the averaging procedure described in Section V.A.1 is adequate if care is taken to minimize the degree of misalignment. The relative flatness of the surface, in turn, makes the alignment procedure easier to perform. Work with the graphite surface, however, entails a more severe set of problems.

A2. Angle Measurements for Graphite

The facets of the graphite surface typically are small and badly misaligned (see Section V.B.1). It is clear that the averaging technique, appropriate for the alkali halides, is not suitable for determining  $\theta$  in graphite work since an entirely new facet will probably be sampled upon rotation by  $60^\circ$  to a crystallographically equivalent position.

Instead, the procedure for determining  $\theta$  described in Section V.B.1 is employed. This assumes that the polar angle scale reading  $\theta'$  is

equal to the true polar angle  $\theta$  except for a constant correction which can be found by zeroing the angle scale. Detector angle measurements,  $\theta_d$ , are made for a set of nominal polar angles  $\theta'$  and are extrapolated to  $\theta_d = 0$ . This yields the value of  $\theta'$  at  $\theta = 0^\circ$  which can then be used to correct all  $\theta'$  measurements. This procedure, however, is also affected by the misalignments and its accuracy is therefore not necessarily assured. Thus, an assessment of the effects of misalignment on the polar angle zeroing procedure was carried out.

### A3. Effects of Misalignment

#### A3a. Surface Normal Misalignments

If the surface normal is not collinear with the azimuthal axis (a tilted facet, for example), the polar angle changes as the azimuth is varied. Therefore, data are taken only within a few degrees of the  $\phi$  value at which the zeroing procedure is done. A new zeroing run is performed when data are wanted at a different  $\phi$ . The tilt will also introduce some error into the detector angle reading, but this error enters linearly to good approximation since the tilt angle is small and therefore, it is taken care of by the extrapolation procedure.

#### A3b. Rotation Axes Misalignments

The misalignments of the polar and detector angle rotation axes are difficult to treat analytically, so an empirical approach was taken. In one case, for example, a zeroing run,  $\theta'$  vs.  $\theta_d$ , was first carried out. Then, the detector angle axis was moved  $\approx 3$  mm laterally.

The same zeroing run was then done again resulting in different detector angle readings but having essentially the same slope and the same value of  $\theta_0$ . These results are presented in Table 12. Although it is not possible to draw general conclusions, no inconsistencies were found to result from these misalignments and it is at least reasonable to expect the extrapolation procedure to compensate for their effects.

### A3c. Beam and Surface Misalignments

The major remaining problems are the beam and the sample surface not being on the polar angle rotation axis. Only these two misalignments are considered here to simplify the analysis. First, define  $d_B$  as the distance between the beam and the axis of rotation  $d_S$  as the distance between the surface and the axis, and  $R$  as the radius of the detector swing. Let  $\alpha = 90^\circ - \theta$ , the angle between the beam and the surface, so that in the ideal case of no misalignment  $\theta_d = 2\alpha$ . In the case of misalignment being present, it is found by geometrical construction that

$$\tan 2\alpha = \frac{R \sin \theta_d - d_B}{R \cos \theta_d - \left( \frac{d_B}{\tan \alpha} - \frac{d_S}{\sin \alpha} \right)} . \quad (A1)$$

This transcendental equation is solved numerically and it is found that the extrapolation procedure is valid, but only for the small degree of misalignment maintained throughout the experiment.

Table 12. Zeroing results before and after detector axis change.

Data of 9/12/79 $\phi = 17^\circ$		Data of 9/15/79 $\phi = 17^\circ$	
$\theta'$	$\theta_d$	$\theta'$	$\theta_d$
direct beam	0.54	direct beam	0.80
80	20.78	80	21.06
75	30.83	75	30.58
70	40.53	70	40.74
65	50.54	65	50.75
60	60.25	60	60.33
55	70.01	55	70.00
50	79.93	50	79.72
45	89.54	45	89.43
40	99.32	40	99.22
35	109.11	35	109.08
		30	118.85
slope = -1.96		slope = -1.95	
$\theta'_0 = 0.42^\circ$		$\theta'_0 = 0.39^\circ$	

VITA

Gregory N. Derry was born March 11, 1952, in Burlington, Vermont. He graduated from Queensbury High School, Glenn Falls, New York in 1970. He then attended Union College, Schenectady, New York, and graduated cum laude with a B.S. degree in Physics in 1974.

He then entered the doctoral program in Physics at The Pennsylvania State University. He has been both a graduate teaching and research assistant, and is currently a member of The American Physical Society.

DISTRIBUTION LIST

Commander (NSEA 09G32)  
Naval Sea Systems Command  
Department of the Navy  
Washington, DC 20362

Copies 1 and 2

Commander (NSEA 0342)  
Naval Sea Systems Command  
Department of the Navy  
Washington, DC 20362

Copies 3 and 4

Defense Technical Information Center  
5010 Duke Street  
Cameron Station  
Alexandria, VA 22314

Copies 5 through 16